
DELIVERABLE

D27.2 Use of improved hybrid dynamic simulation for novel isolators/dissipators, for thermomechanical applications, and for soil-structure interaction studies

Work package	WP27/JRA5 - Innovative testing methodologies for component/system resilience
Lead	António A. Correia (LNEC)
Authors	Amadeo Benavent (UPM) Stathis Bousias (UPAT) Gidewon G. Tekeste (LNEC) Giuseppe Abbiati (ETH) Bozidar Stojadinovic (ETH)
Reviewers	Oreste Salvatore Bursi (UNITN) Patrick Covi (UNITN)
Approval	Management Board
Status	Final
Dissemination level	Public
Delivery deadline	31.10.2019
Submission date	28.04.2020
Intranet path	DOCUMENTS/DELIVERABLES/ SERA_D27.2_Use_of_improved_hybrid_dynamic_simulation.pdf



Table of Contents

Summary	4
1 Novel tests and results of smart materials	6
1.1 Improved energy dissipators equipped with smart materials.....	6
1.1.1 Introduction	6
1.1.2 Description of the improved displacement-dependent damper	7
1.1.3 Investigations on large diameter NiTi bars (SMA part of the new damper).....	8
1.1.4 Investigations on tube-in-tube assemblage (TTD part of the new damper)	14
1.1.5 Development of new Damping Corrections Factors	22
1.2 Tests on improved energy isolators equipped with smart materials	23
1.2.1 Experimental program	25
1.2.2 Test campaign.....	27
2 Soil-structure interaction analysis with HDS.....	38
2.1 Three-loop architecture framework for hybrid simulation	38
2.1.1 OpenSees software framework	39
2.1.2 Middleware software.....	40
2.1.3 Simulation coordinator VI	40
2.1.4 FPGA VI	47
2.1.5 LabVIEW based TCP/IP interface.....	50
2.1.6 Command generation and tracking	52
2.1.7 Command compensation.....	55
2.1.8 Tracking Indicator	59
2.2 Data acquisition and transducers.....	60
2.3 HDS framework validation	61
2.3.1 Case-study	61
2.3.2 Test setup	62
2.3.3 Rehearsal test for hybrid simulation	66
2.3.4 Hybrid test experiment.....	67
2.4 Soil-structure interaction analysis via HDS.....	68
3 Use of HDS for thermomechanical applications.....	72
3.1 Thermomechanical test rig	72
3.1.1 Mechanical transfer system.....	73
3.1.2 Thermal transfer system.....	74
3.1.3 Real-time control system	75
3.2 Verification of the MTF	75
3.2.1 Benchmark case study	75

3.2.2	Results and discussions.....	77
3.3	Verification of the TTF.....	78
3.3.1	Benchmark case study	78
3.3.2	Results and discussions.....	80
3.4	OpenFresco Class	82
4	Conclusions and future developments.....	84
4.1.1	Conclusions.....	84
4.1.2	Future developments.....	85
5	References.....	86

Summary

This report starts by presenting and discussing novel cyclic and dynamic tests carried out @UPM and @UPATRAS on energy dissipators based on smart materials and on fibre-reinforced elastomeric isolators (FREIs). Afterwards, the development of a hybrid dynamic simulation (HDS) framework and its application @LNEC are presented and discussed, with emphasis on the use of a shake table and additional actuator for analysing a soil-structure system. Finally, it presents the innovative test rig for thermomechanical applications @ETH Zurich and its application to hybrid fire simulation (HFS).

With regard to passive energy dissipation devices, the design of structures with displacement-dependent energy dissipation devices requires the development of new testing/design methods. The q -factor approach used for conventional structures is not appropriate for structures with energy dissipation systems. One alternative are the methods that predict the response with an equivalent single degree of freedom (SDOF) system with an effective period associated with a secant stiffness at point of maximum displacement, and an effective damping ratio that converts the hysteretic energy dissipated by the dampers into an equivalent linear viscous damping, i.e. the capacity spectrum approach. A key aspect of these methods is the modification of the 5% damped elastic spectrum for high levels of damping through the so-called damping corrections factors (DCF). Therefore, the proposed experimental campaign allowed for novel equations for DCFs to be developed.

As far as fibre-reinforced elastomeric isolators (FREI) are concerned, it becomes obvious that relevant experimental studies are rather limited in scope and extent. In particular, in order to fully understand their response characteristics and contribution to seismic vulnerability reduction, they have to be tested in actual conditions involving realistic structures. As a nonlinear response is expected to develop only on FREIs, the rest of the full scaled building can be numerically represented, while FREIs are experimentally tested, i.e. via dynamic substructuring or hybrid simulation (HS). Therefore, the main objectives of this work were to investigate the behaviour of such bearings and, in particular, the temperature effects developed during cycling at large deformations.

With respect to the HDS framework for soil-structure systems, it deals with one of the difficult aspects of building infrastructure seismic response – soil-structure interaction (SSI). This section presents how hybrid simulations in SSI problems may be carried out. This approach has proven to be quite challenging; nonetheless, recent innovative testing schemes make it a viable technique. Therefore, ways for extending and evolving the experimental capabilities of hybrid tests for SSI problems are presented and discussed. The report presents the development and validation of a software framework for (HDS). The ingredients that make-up an efficient HDS testing facility are explained in greater depth; and improvements on the existing schemes are presented. A three-loop architecture software framework in the form of a state-machine is proposed and developed in this work. Implementation of the software framework in LabVIEW programming software is discussed in detail followed by its validation using hybrid test experiments conducted on a steel frame. At the end, the potential, limitations and future developments of the software framework are briefly pointed out.

Finally, HFS is presented and discussed as a way to circumvent the need for large-scale structural fire tests, which are rare because they require for expensive specialized facilities. As a result, most of the research regarding the behaviour of structures in fire has been carried out on single structural components subjected to standard heating curves. Although such tests offer significant information about the fire performance of specific structural elements, they do not account for force redistribution owing to the interaction of the tested structural component with the remaining part of the structure. In order to overcome such limitations, HDS emerged as a viable alternative to both large-scale and component fire testing in the last two decades, resulting in hybrid fire simulation (HFS) techniques. In

In this section, the thermomechanical (TM) test rig recently developed @ETH Zurich for testing plates under different thermal and mechanical boundary conditions is presented. A real-time computer coordinates both thermal and mechanical actuation devices as well as data acquisition. Starting from the existing test rig, the development of a thermomechanical hybrid simulation platform is described, as well as some experimental tests performed. This research expands the state-of-the-art paradigm of HDS, which mainly focused in the area of structural seismic testing, towards stochastic multi-physics hybrid simulation.

1 Novel tests and results of smart materials

1.1 Improved energy dissipators equipped with smart materials

1.1.1 Introduction

Northridge, in 1994, and Kobe, in 1995, ground motions highlighted that conventional earthquake-resistant systems result in significant structural and nonstructural damage, initiating the transition to Performance-Based Design (PBD). Passive control systems (base isolation and energy dissipation) have proven to be a very effective solution to attain the objectives of PBD. This research focuses on energy dissipation and particularly on structures with metallic dampers. Despite their short history, the advantages of structures with energy dissipation systems in comparison with conventional systems and their ability to increase the robustness and resilience of buildings are now widely recognized. However, they are considered a special solution for singular (high-rise) buildings in high seismicity regions, and use in Europe is still incipient. One current challenge is to make structures with energy dissipation systems a “usual” solution of massive use in low-to-middle structures located in low-to-moderate seismicity regions. To this end, it is necessary to develop cost-effective dampers and to cope with certain limitations of present technologies.

Metallic dampers are low cost, have stable hysteretic behavior and large energy dissipation capacity, and provide long-term reliability. They have also limitations. One lies in the residual deformations after an earthquake. Another is that they do not dissipate energy until metal yielding, thus they can be ineffective for mild earthquakes. Allowing metal yielding under mild earthquakes or even under wind loads can lead to high cycle fatigue problems that would reduce the energy dissipation capacity of the damper in case of strong earthquakes. This research investigates an improved displacement-dependent damper intended to remedy these drawbacks. The damper consists of a tube-in-tube configuration of two commonly available hollow structural steel sections with a central bar made of Nickel-titanium (NiTi) Shape Memory Alloys (SMAs). The outer steel hollow section has a series of strips created by cutting slits through the wall, and it is connected to the inner hollow section in such a way that when the brace damper is subjected to forced displacements in the direction of its axis beyond a trigger quantity δ_t , the strips deform and dissipate energy through flexural/shear yielding. The NiTi bar is entrusted with two tasks: (i) to provide recentering capability and (ii) to dissipate energy under mild earthquakes or wind loads. The steel strips created by cutting slits through the wall outer steel hollow section are entrusted with the task of dissipating most of the energy input by a strong earthquake. The trigger axial displacement δ_t gives the improved damper a multiphased nature: for displacements $\delta_t \leq \delta$ hysteretic energy is dissipated only by the NiTi bar; for $\delta_t > \delta$ the energy is mostly dissipated by the steel strips of the outer steel hollow section.

Moreover, the design of structures with displacement dependent energy dissipation devices requires the development of new methods. The q-factor approach used for conventional structures is not appropriate for structures with energy dissipation systems. One alternative are the methods that predict the response with an equivalent single degree of freedom (SDOF) system with an effective period associated with a secant stiffness at point of maximum displacement, and an effective damping ratio that converts the hysteretic energy dissipated by the dampers into an equivalent linear viscous damping (i.e. the capacity spectrum approach). A key aspect in these methods is the modification of the 5% damped elastic spectrum for high levels of damping through the so-called damping corrections

factors (DCF). New equations for DCFs are presented to be used for the design of structures with energy dissipation devices.

1.1.2 Description of the improved displacement-dependent damper

A new damper referred to as TTD-SMA damper hereafter (Tube-in-Tube Damper with SMA bars) is developed. It consists of the tube-in-tube assemblage of two commonly available hollow structural sections made of stainless-steel, as shown in Figure 1. The outer hollow section has a series of strips created by cutting slits through the wall, and it is connected to the inner hollow section in such a way that when the brace damper is subjected to forced displacements in the direction of its axis beyond a trigger quantity δ_t , the strips deform and dissipate energy through flexural/shear yielding. The axial displacement δ_t that triggers the deformation of the strips is controlled by the designer, and it is intended to avoid deformations in the strips and thus high-cycle fatigue problems when the building is subjected to mild earthquakes or strong winds. The TTD-SMA damper has recentering capability provided by a large diameter NiTi bar located along the axis of the damper and assembled with the inner and outer tubes in such a way that, regardless of the brace damper being subjected to tension or compression, one half of the SMA bar is in tension and the other half is not loaded.

The typical strain-stress σ - ε , relationship of a SMA bar subjected to cyclic tension deformations is shown in Figure 2. The TTD-SMA damper possesses a multiphase nature that improves the response under wind and very frequent, frequent or severe earthquakes, in comparison with conventional metallic dampers. In the first phase, for strains ε in the SMA bar up to about 1.25% and axial displacements of the damper below δ_t indicated in Figure 1, the TTD-SMA device exhibits a linear elastic behavior and the strips of the outer tube remain undeformed. In this initial phase the lateral stiffness added by the new damper is smaller than that of a conventional metallic damper, since the Young modulus of SMA material is markedly smaller than conventional steel. In the second phase, for strains in the SMA bar ε in between approximately 1.25% and 5%, and axial displacements in the damper below δ_t , the TTD-SMA damper dissipates energy through the hysteretic behavior of the SMA bar (see Figure 2) with negligible permanent deformations, while the strips of the outer tube remain undeformed. In the third phase, for strains in the SMA bar ε larger than about 5% and axial displacements of the damper beyond δ_t , the strips of the outer tube dissipate most of the energy through plastic deformations while the superelastic properties of the SMA provide recentering capabilities. Besides recentering, the strain hardening exhibited by the SMA bar provides additional resistance against P-delta effects. The new damper design is intended to respond in the first phase for wind or very frequent earthquakes, in the second phase for frequent earthquakes, and in the third phase for rare or very rare earthquakes.

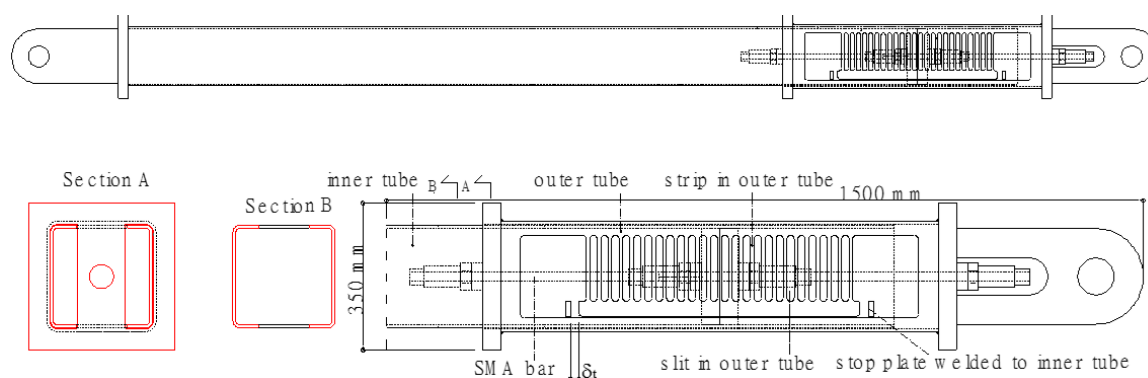


Figure 1: TTD-SMA damper (upper) and detail of the damping mechanism (lower)

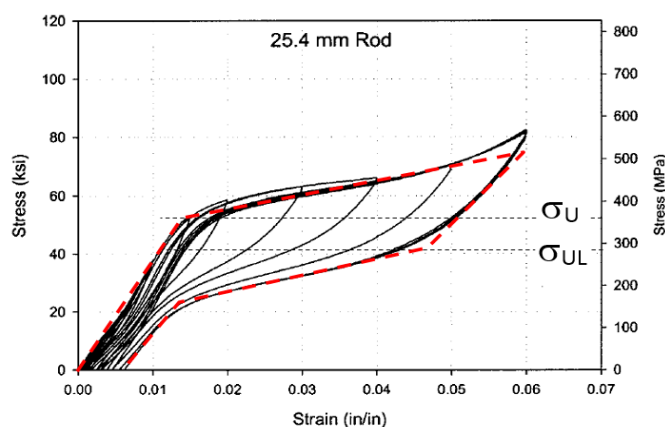


Figure 2: Typical ε - σ curve of SMA bar

The investigations conducted separately on the NiTi bars (SMA part of the damper) and on the assemblage of the two tubes (TTD part of the damper) are presented next in sections 1.1.3 and 1.1.4. Further, the developments on new damping correction factors (DCF) that could be used for the design of structures with energy dissipation devices of the type investigated in this research are presented in section 1.1.5.

1.1.3 Investigations on large diameter NiTi bars (SMA part of the new damper)

1.1.3.1 Static and dynamic cyclic tests

This sub section describes the test campaign conducted to characterize the hysteretic behavior of NiTi bars of large diameter, and to evaluate its ultimate energy dissipation capacity.

Test specimens

Quasi-static and dynamic cyclic loadings were imposed in nine specimens consisting of cylindrical 12.7mm diameter and 750 mm length bars made of SMAs. The specimens have identical geometry, thermo-mechanical processing and material composition. The NiTi bars were subjected to a heat treatment that guaranteed the superelastic properties at room temperature.

Loading set up and loading protocol

Quasi-static tests

Six specimens (referred to as S_{11} to S_{16} , where the first number identifies the loading protocol, and the second the number of the specimen) were subjected to the loading protocol 1 shown in Figure 3; it consisted on imposed cyclic displacements of constant amplitude at $\varepsilon=4.5\%$ with a frequency of 0.02Hz (quasi-static loads). Two specimens (referred to as S_{21} to S_{22}) were subjected the loading protocol 2 shown in Figure 4; it consisted on cyclic loads at two different frequencies of 0.02 Hz (S_{21}) and 0.04 Hz (S_{22}) (quasi-static). Two specimens (referred to as S_{31} to S_{32}) were subjected to the loading protocol 3 shown in Figure 5 until failure; it consisted on multiple-step cyclic displacements at a frequency of 0.02 Hz (quasi-static). One specimen (referred to as S_{41}) was subjected to the loading protocol 4 shown in Figure 6; it consisted on cyclic displacements until failure at a frequency of 0.02 Hz (quasi-static). All tests were conducted in ambient conditions (20°-25°) with a universal testing machine SAXEWAY T1000.

Dynamic tests

Two additional specimens (referred to as D_{21} and D_{22}) were subjected to the loading protocol 2 shown in Figure 4, applied at two different frequencies of 0.2Hz and 1.0Hz (dynamic loading). An INSTRON 8803 fatigue testing system was used for the tests.

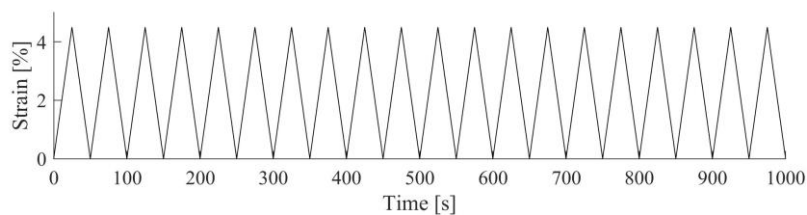


Figure 3: Loading protocol 1 used for specimens S₁₁ to S₁₆

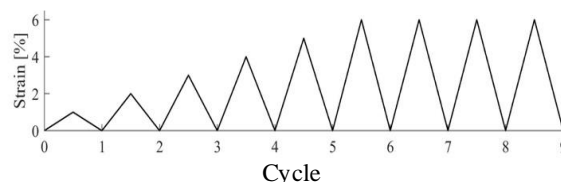


Figure 4: Loading protocol 2 used for specimens 0.02, 0.04, 0.2, 1.0 Hz used for S₂₁, S₂₂, D₂₁, D₂₂

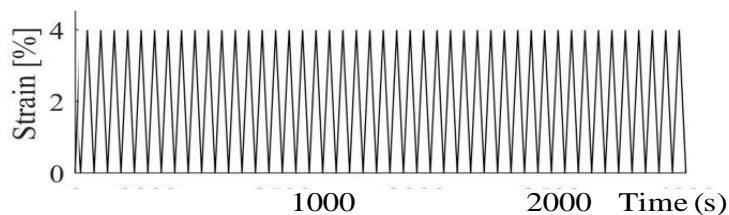


Figure 5: Loading protocol 3 (frequency 0.02 Hz) used for specimens S₃₁, S₃₂

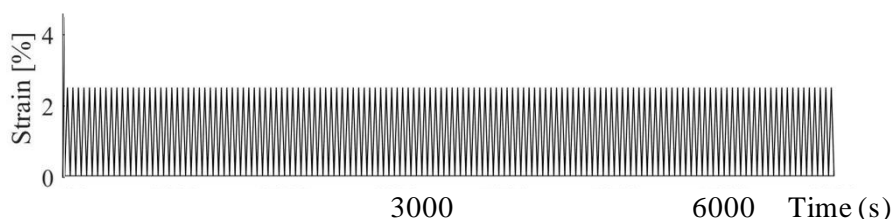


Figure 6: Loading protocol 4 (frequency 0.02 Hz) used for specimen S₄₁

Test results

Hysteretic behaviour

The stress-strain curves obtained for specimen S₁₁ under quasi-static imposed deformations are shown in Figure 7. Similar curves were obtained for specimens S₁₂ to S₁₆. In the initial cycles the loading and unloading transformation stresses tend to diminish, resulting in a reduction of the energy dissipated in each cycle (functional fatigue). The hysteretic loops tend quickly to stabilize in successive cycles, and the maximum stress and residual strain ϵ_R is practically the same in all cycles.

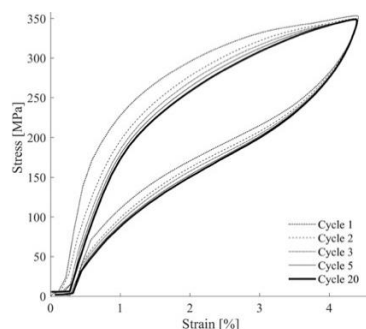


Figure 7: Hysteretic loops of specimens under quasi-static displacements of constant amplitude

The stress-strain curves obtained for the specimens S₂₁, S₂₂, D₂₁ and D₂₂ are shown in Figure 8. It can be seen that the loading and unloading paths for a given amplitude overlap the loading and unloading

paths obtained in cycles of lower amplitude. It is worth noting also that the shape of the loops depends on the frequency of the dynamic loading. To better understand this dependency the hysteretic loops at 6% strain are shown in Figure 9. As can be seen in this figure, an increase in the strain rate results in greater loading and unloading transformation stresses, narrower hysteresis loops and earlier occurrence of strain hardening effect. In contrast, the amount of residual strain is not affected by the frequency of the applied loading.

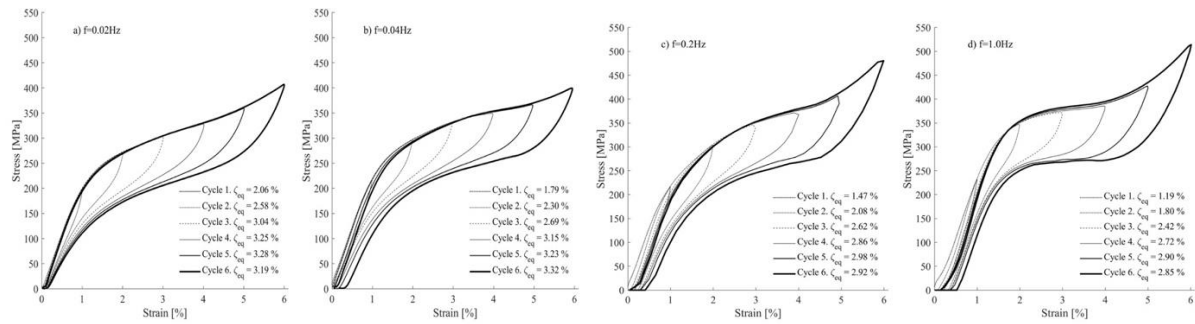


Figure 8: Hysteretic loops of specimens: (a) S₂₁; (b) S₂₂; (c) D₂₁ and (d) D₂₂

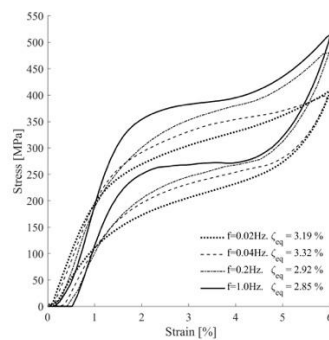
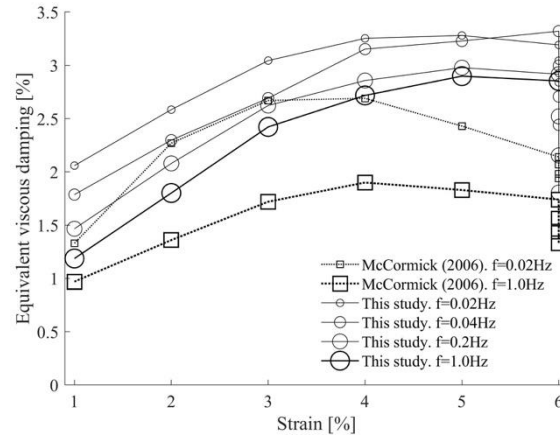


Figure 9: Hysteretic loops of specimens under quasi-static and dynamic loading at 6% strain

Equivalent viscous damping ratio

Figure 10 shows the equivalent viscous damping ratios ξ_{eq} computed for specimens S₂₁, S₂₂, D₂₁ and D₂₂. It is defined as $\xi_{eq} = E_D / (2\pi \epsilon_{max} \sigma_{max})$ where E_D is the energy dissipated in one loop of hysteresis, ϵ_{max} and σ_{max} are the maximum strain and stress, respectively, in the cycle. The results of the tests conducted in this study are compared with the values reported by McCormick et al. (2007) on NiTi bars having the same diameter (12.7mm). It can be seen that the specimens tested by McCormick et al. (2007) exhibited in general lower values of ξ_{eq} and a wider range of variation depending on the amplitude and the number of cycles applied at $\epsilon=6\%$. These differences are attributed, among other factors, to material composition and thermomechanical treatment.


 Figure 10: Equivalent damping ζ_{eq} for 12.7mm diameter NiTi bars

The effect of the strain rate on the amount of energy dissipated in a single cycle at $\epsilon=6\%$ amplitude was investigated to identify possible differences between wires and bars made of NiTi allows. The results of specimens S_{21} and D_{22} , were compared with the tests conducted by McCormick et al. (2007), Zhu and Zhang (2013), Dolce and Cardone (2001) and DesRoches et al. (2004) on wires and bars subjected to one cycle of amplitude $\epsilon=6\%$ at frequencies of 0.02Hz and 1.0Hz. To make the results comparable, E_D dissipated in one cycle was normalized by the product of the yield force F_y and yield displacement δ_y . F_y and δ_y were determined idealizing the loading branch of the $F-\delta$ curve obtained from the tests with two segments. The slope and position of these segments was determined so that the slope of the second segment of the bilinear approximation closely fits the path of the loading transformation phase, and the area under the real curve and the bilinear approximation was the same. Table 1 shows the results. In the Table, ϕ is the diameter, σ_y is the yield stress $\sigma_y=(F_y/[\pi(\phi/2)^2])$, ϵ_y is the yield strain and $\bar{E}_D=E_D/F_y\delta_y$. The values of σ_y , ϵ_y , E_D and \bar{E}_D vary depending on the frequency. The last column of Table 1 shows the ratio between \bar{E}_D obtained for quasi-static loading (0.02Hz), $\bar{E}_{D,static}$, and the corresponding value obtained for dynamic loading (1.0 Hz), $\bar{E}_{D,dynamic}$. The specimens with $\phi \leq 2$ mm are referred to as wires and those with $\phi > 6$ mm as bars. It follows from Table 1 that the average value of $\bar{E}_{D,static}$ is 1.4 in wires and 1.62 in bars, and the counterpart values of $\bar{E}_{D,dynamic}$ are 1.1 and 0.87 respectively. There are not clear differences between wires and bars from the point of view of the normalized dissipated energy. However, the reduction of energy dissipation under dynamic loads in comparison with static loads in terms of the ratio $\bar{E}_{D,dynamic} / \bar{E}_{D,static}$ is about 40% larger on bars than on wires. Also, it is seen that σ_y increases with frequency and this increase is larger in bars than in wires.

 Table 1: Energy dissipated in a single cycle at $\epsilon=6\%$ amplitude and different frequencies

	Frequency: ϕ (mm)	σ_y (N/mm ²)		ϵ_y (%)		E_D (MPa)		$\bar{E}_D=E_D/(F_y\delta_y)$		$\frac{\bar{E}_{D,dynamic}}{\bar{E}_{D,static}}$
		0.02	1.0Hz	0.02	1.0Hz	0.02	1.0 Hz	0.02	1.0 Hz	
		McCormick	0.254	504	553	1.83	1.79	275	309	
Zhu	0.58	305	309	1.22	1.12	250	275	2.10	1.48	0.71
Dolce	1.84	390	415	1.40	1.25	279	332	1.00	0.83	0.84
DesRoches	7.10	315	374	1.33	1.40	237	267	1.67	0.71	0.42
McCormick	12.70	328	414	1.33	1.54	247	269	1.41	0.78	0.56
This study	12.70	245	359	1.12	1.39	219	258	1.78	1.11	0.62

Ultimate energy dissipation capacity

Under a severe earthquake, a NiTi bar installed in a structure for passive control can be subjected from several dozens to several hundreds of cycles of forced displacements in the plastic range. In these

loading conditions, the cumulation of plastic deformations (low cycle fatigue) can lead the NiTi bar to exhaust its energy dissipation capacity and fail. Several fatigue failure models have been developed following an energy criterion. However, they are based on tests conducted with NiTi wires and micro-tubes. In this subsection their validity for NiTi bars is studied, using the results of the tests conducted on specimens S_{31} , S_{32} and S_{41} . First, the total amount of energy dissipated by these specimens until failure, normalized by $F_y \delta_f$, i.e. $\Sigma \bar{E}_{D,static} = \Sigma E_{D,static} / (F_y \delta_f)$, was calculated and is shown in the second column of Table 2. Second, the normalized energy dissipated in a single cycle, i.e. $\bar{E}_{D,static} = E_{D,static} / (F_y \delta_f)$, was calculated and is shown in the third column of Table 2. Third, the total dissipated energy was expressed in terms of equivalent number of cycles N_f defined by $N_f = \Sigma \bar{E}_{D,static} / \bar{E}_{D,static}$; it is shown in the fourth column of Table 2. It is worth recalling that specimens S_{31} , S_{32} and S_{41} were subjected to quasi-static loads, and it has been shown in previous section that the amount of energy dissipated under dynamic loading is smaller than under static loads. For the $\phi=12.7$ mm bars tested in this study $\bar{E}_{D,dynamic} / \bar{E}_{D,static}$ is 0.62 (last row in Table 1). Using this ratio, the normalized energy dissipated in a single cycle under dynamic loading $\bar{E}_{D,dynamic}$ was estimated multiplying $\bar{E}_{D,static}$ by 0.62; the results are shown in the last column of Table 2. The values (N_f , $\bar{E}_{D,dynamic}$) obtained in this way for specimens S_{31} , S_{32} and S_{41} are plotted with circles in Figure 11. These results are compared with those obtained by Moumni et al. (2005) (square symbols) for 6.2mm diameter NiTi bars tested under dynamic (0.3 Hz) loads. Since the ratio $\bar{E}_{D,dynamic}$ increases with the amplitude of the cycle, $\bar{E}_{D,dynamic}$ is directly related to the amplitude of the cyclic loading. The ultimate energy dissipation capacity corresponding to each point in Figure 11, is simply obtained by multiplying the abscissa (N_f) by the ordinate $\bar{E}_{D,dynamic}$.

Table 2: Ultimate normalized energy dissipation capacity

ϵ (%)	$\Sigma \bar{E}_{D,static}$	$\bar{E}_{D,static}$	N_f	$\bar{E}_{D,dynamic}$
4.0	124	1.17	106	0.73
4.0	112	1.17	96	0.73
2.5	260	0.52	500	0.32

It is observed in Figure 11 that the ultimate energy dissipation capacity of NiTi bars subjected to low-cycle fatigue obtained in this study is consistent with the values reported in Moumni et al. (2005). From a regression analysis of these results, the ultimate energy dissipation capacity of NiTi bars subjected to dynamic cyclic loading can be estimated with the following expression:

$$\bar{E}_{D,dynamic} = 7,0 N_f^{-0.52}$$

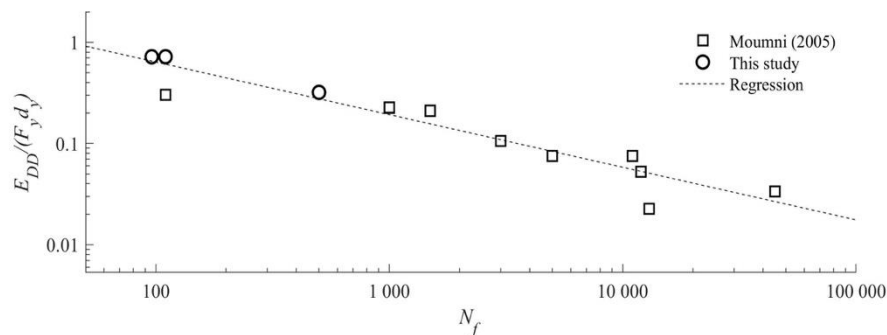


Figure 11: Normalized energy dissipation versus the number of cycles to failure

1.1.3.2 Numerical models for representing the cyclic behaviour of NiTi bars

The hysteretic behaviour of NiTi bars has been represented in the past with the flag-shape model shown in Figure 12. This model is simple and is defined by few parameters: initial stiffness k_1 , loading phase transformation stiffness k_{2L} , unloading phase transformation stiffness k_{2UL} , the strain hardening stiffness k_3 , loading transformation strength at start F_{Ls} , loading transformation deformation at finish δ_{Lf} , and

ratio of loading transformation strength at start $\beta \cdot F_{Ls}$ and k_1 can be easily determined from the cross area A and length L of the bar, and the Young's modulus E and yield stress σ_{Ls} of the material, i.e. $F_{Ls} = \sigma_{Ls} A$ and $k_1 = EA/L$. However, flag-shape model has as drawback: it cannot capture the residual deformation associated with the residual strain ϵ_R (see Figure 7). When the NiTi bar is subjected to few cycles of large amplitude, the amount of dissipated energy associated with the residual strain ϵ_R is negligible in comparison with the energy dissipated in a complete cycle, and the conventional flag-shape model captures reasonably well the actual amount of energy dissipated by the NiTi bar. However, in case of a loading history consisting of few cycles of large amplitude and a large number of cycles of small amplitude (this is the typical loading pattern imposed by earthquakes), the amount of energy dissipated by the small amplitude cycles can be comparatively very large. In this later case, the conventional flag-type model can lead to a wrong prediction of the energy accumulated on the NiTi bars.

To solve this flaw without losing simplicity, a new hysteretic model is proposed that consists of two springs connected in parallel as shown in Figure 13. One of the springs follows the force-displacement rule of the conventional flag-type model described above (Figure 12) but with the initial stiffness and the loading transformation strength at start weighted by a factor γ (Figure 13a). The restoring force of the second spring follows an elastic-perfectly plastic (EPP) model with yield force equal to $(1-\gamma)F_{Ls}$ and elastic stiffness k_{EPP} (Figure 13b). The sum of the restoring forces provided by both springs gives the complete hysteretic model shown in Figure 13c. In the proposed hysteretic model F_{Ls} and k_1 are determined from the geometry of the bar and the mechanical properties of the material (i.e. $F_{Ls} = \sigma_{Ls} A$ and $k_1 = EA/L$), and the rest of parameters have been calibrated with the results of the dynamic cyclic tests giving: $k_{2L} = k_1/15$, $k_{2UL} = 2k_{2L}/3$, $k_3 = k_1$, $\delta_{Lf} = 4F_{Ls}/k_1$, $\beta = 0.4$ and $k_{EPP} = 4k_1$. The shape of the hysteretic loops obtained with the proposed model is compared in Figure 14 with the results of the tests conducted with specimen D₂₂. The difference in terms of dissipated energy is less than 10%.

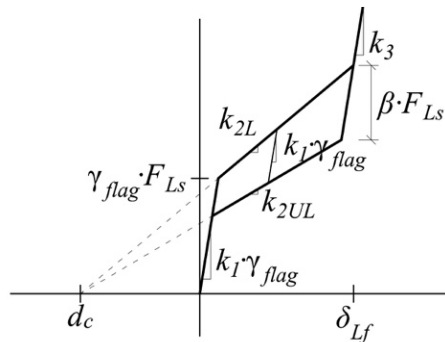


Figure 12: Conventional flag-shape model

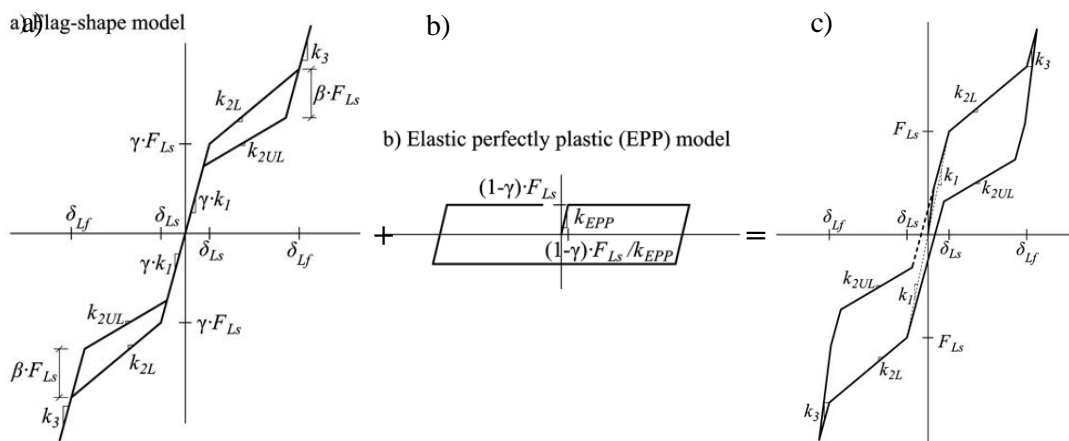


Figure 13: Proposed hysteretic model: (a) flag-shape component, (b) elastic-perfectly plastic component; (c) complete model

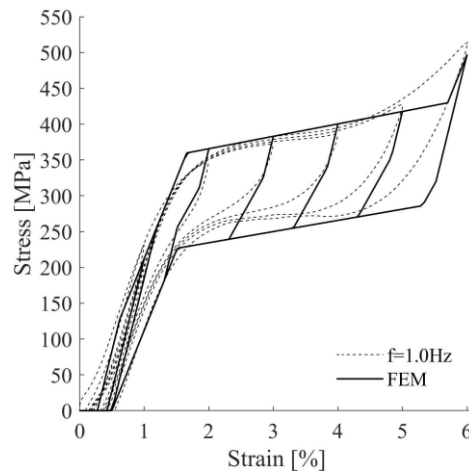


Figure 14: Comparison between proposed hysteretic model and dynamic cyclic tests

1.1.4 Investigations on tube-in-tube assemblage (TTD part of the new damper)

1.1.4.1 Dynamic and static tests

Test specimens

Figure 15 shows the tube-in-tube (TTD) subassembly that constitutes the basic part of the new damper. The four sides of the outer tube are regularly slit transversally leaving “struts” of steel that constitute the main source of energy dissipation of the new damper. When the damper is subjected to imposed deformations along its axis, the struts work as fixed-ended beams deforming in double curvature. Three specimens (referred to as TTD4, TTD5 and TTD6 herein) with the geometry shown in Figure 16a and made of stainless steel grade 1.4301 (304-L AISI), were built and tested under dynamic and under static loadings. The outer and inner tubes were #150.4mm and #140.4mm (#width.thickness) square hollow sections cut from a single segment. A total of 100 struts (25 per face) with dimensions of $b=5\text{mm}$, $h=80\text{mm}$, $t=4\text{mm}$ and a radius of the ends of $r=5\text{m}$ were slit on the outer tube. The geometry of the struts is shown in Figure 16b. The material properties were obtained from tensile tests at different strain rates and are shown in Table 3, where $\sigma_{0.2\%}$ is the 0.2% yielding stress, σ_y and ϵ_y are the stress and strain at yielding, σ_u and ϵ_u are the ultimate stress and strain, and σ_b and ϵ_b are the stress and strain at the end of the smooth transition branch from the elastic to the inelastic range.



Figure 15: Tube-in-tube subassemblage

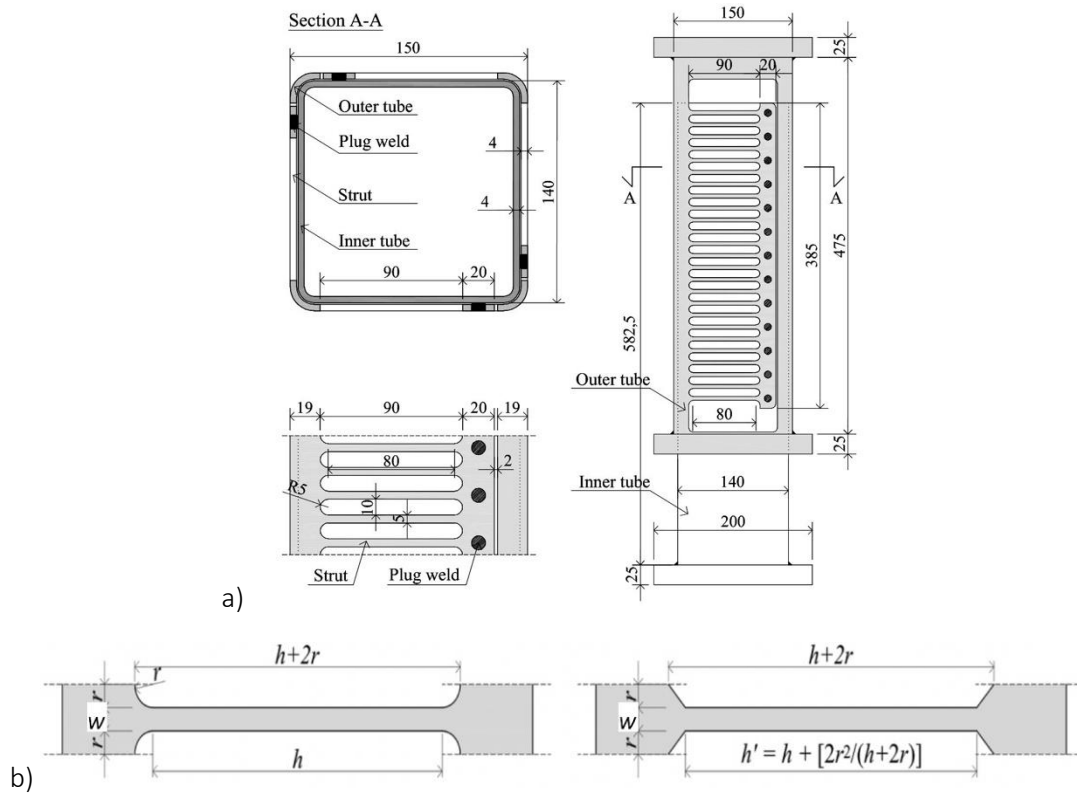


Figure 16: Test specimens

Table 3: Mechanical properties of the stainless steel

Strain rate (Hz)	$\sigma_{0.2\%}$ (MPa)	σ_u (MPa)	σ_y (MPa)	σ_b (MPa)	ϵ_y (%)	ϵ_b (%)	ϵ_u (%)
0.01	377±15	604±30	250±5	405±15	0.12±0.05	0.40±0.01	46±1
0.5	529±6	709±16	400±10	560±15	0.20±0.01	0.57±0.02	44±2

Loading set-up and loading protocol

Dynamic tests

First, a prototype structure consisting of RC waffle-flat plates supported on RC columns was designed. The elevation is shown in Figure 17. From this structure, the portion enclosed with red dashed lines in Figure 17 was selected. It had one storey and half, and one span and half. From this portion of the structure, a test model was defined by applying a scale factor $\lambda_L=2/5$ to the linear dimensions. The test model was built in Laboratory; the approximate dimensions were $3 \times 3 \times 3 \text{ m}^3$. Second, three dampers (named TTD1, TTD2 and TTD3 in Figure 18) were installed in the first (ground) storey, and three (named TTD4, TTD5, TTD6 in Figure 18) in the second storey. This study focuses on the results obtained from the TTDs located on the second storey, namely TTD4, TTD5, TTD6.

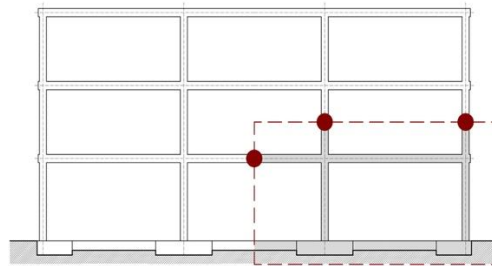
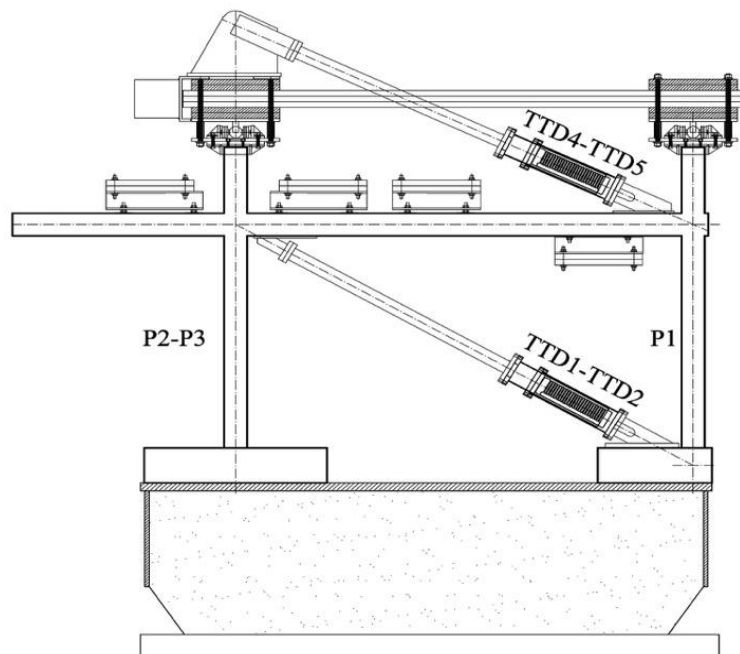


Figure 17: Prototype structure (enclosed with dashed lines the portion used to define the test model)

The RC scaled partial structure with the TTD dampers was mounted on a MTS $3 \times 3 \text{ m}^2$ shake table as shown in Figure 19. The TTD dampers were instrumented with displacement transducers and strain gauges at both ends, in order to record the axial load-deformation curves. Figure 19 shows the test specimen equipped with the TTDs and part of the instrumentation utilized.



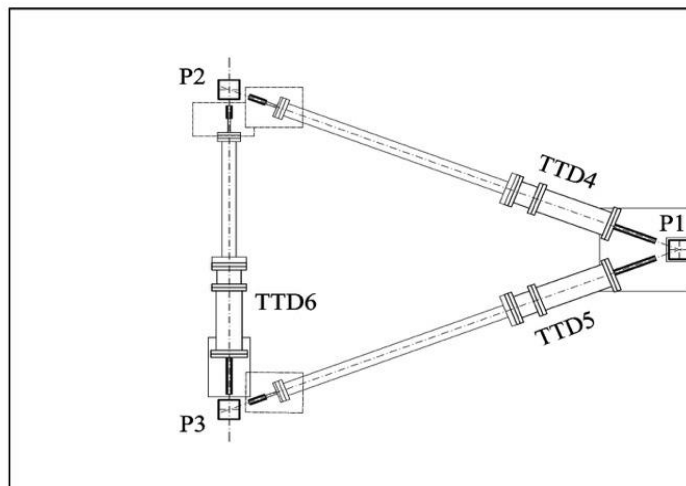


Figure 18: Test model: elevation (top), plan (bottom)



Figure 19: General overview of the test specimen installed in the shake table

The test model was subjected to a series of seismic simulations with increasing intensity, that reproduced, appropriately scaled, the near fault ground motion recorded at Bar-Skupstina Opstine during the Montenegro earthquake in 1979. After the seismic simulations, the RC concrete structure remained basically elastic (undamaged). The TTD dampers experienced severe plastic deformations but their ultimate energy dissipation capacity was not exhausted.

Quasi-static tests

In order to investigate the ultimate energy dissipation capacity of the TTD dampers, after performing the shake table dynamic tests, the three specimens TTD4, TTD5 and TDD6 were subjected to quasi-static cyclic loading until failure. To this end, each specimen was unassembled from the RC structure and tested under cyclic loading on a universal testing machine SAXEWAY T1000, as shown in Figure 20. The quasi-static cyclic tests were carried out under displacement control at 0.02Hz. Three different histories of cyclic displacements were applied to the specimens. In the first and second cyclic tests, the specimens were subjected to a set of cycles of incremental amplitude. The increment of amplitude from one set of cycles to the next was equal to the yield displacement of the TTD damper. In the first cyclic test, each set had 10 cycles, while in the second

cyclic test the number of cycles of each set was 4. The third cyclic test consisted on cycles of constant amplitude.

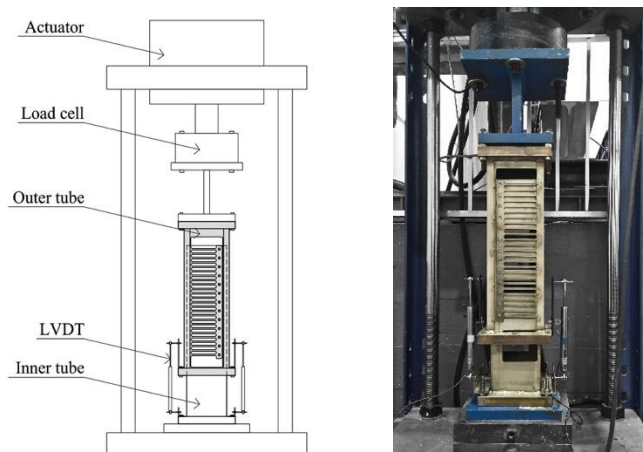


Figure 20: Experimental set-up used during the cycling tests

Test results

Hysteretic curves

The axial force-displacement, $Q-\delta$, curves obtained from the dynamic shake table tests are shown in Figure 21.

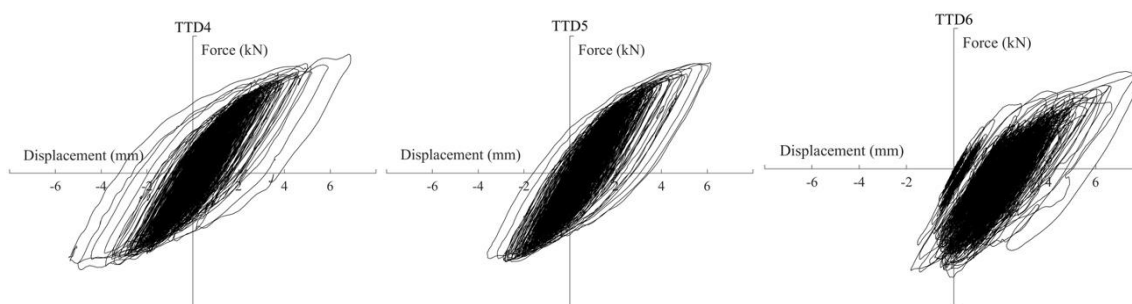


Figure 21: $Q-\delta$ curves obtained from shake table tests: (a) TTD4, (b) TTD5, (c) TTD6

The $Q-\delta$ hysteretic curves obtained from the quasi-static cyclic tests are shown in Figure 22. The solid lines represent the hysteretic behaviour up to the failure point, while the dot lines are the $Q-\delta$ hysteretic curves after failure. Failure was assumed to occur when the load started to decrease with increasing imposed deformations.

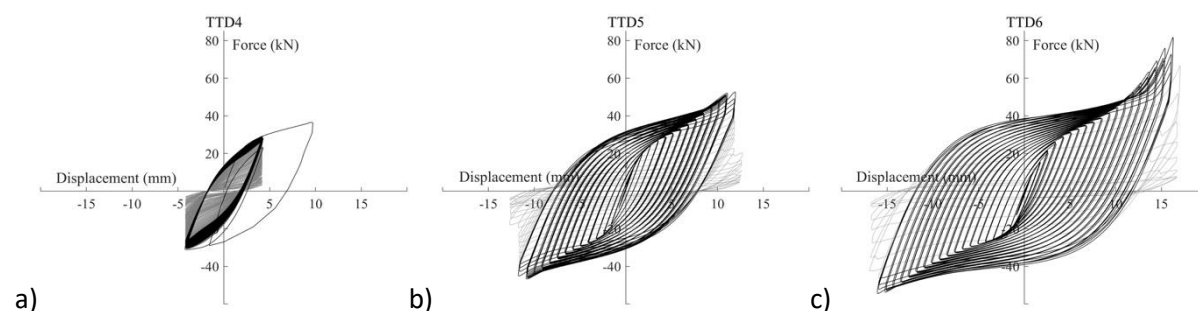


Figure 22: $Q-\delta$ curves obtained from the quasi-static cyclic tests: (a) TTD4, (b) TTD5, (c) TTD6

Since the material properties of the stainless-steel depend on the strain rate (see Table 3), in order to plot together the $Q-\delta$ hysteretic curves obtained from the dynamic and from the quasi-static tests, the

curves were previously normalized dividing by the yield force Q_y and yield displacement δ_y calculated with Equations (1) and (3) presented later, using the material properties obtained at 0.01 Hz (see Table 3) for the quasi-static tests, and the material properties obtained at 0.5 Hz (see Table 3) for the dynamic tests. The complete Q - δ curves are shown in Figure 23.

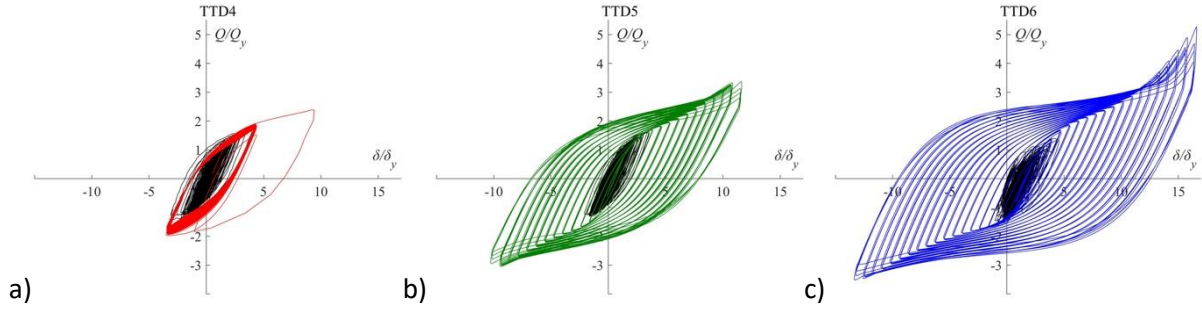


Figure 23: Complete normalized Q - δ curves of the tested specimens: (a) TTD4, (b) TTD5, (c) TTD6

Ultimate energy dissipation capacity

Figure 24a shows the typical force displacement, Q - δ , curve of a TTD specimen obtained from cyclic tests. The curve can be decomposed into two parts, the skeleton part and the Bauschinger part (Benavent-Climent, 2007). The skeleton part is formed by sequentially connecting the segments of the Q - δ curve that exceed the load level attained in preceding cycles in the same domain of loading (indicated with a square symbol in Figure 24a). Referring to Figure 24a, this means sequentially connecting the segments labelled 0-1, 5-6, 11-12, 17-18, 23-24, 29-30 in the positive domain, and 2-3, 8-9, 14-15, 20-21, 26-27 in the negative domain. The skeleton part obtained in this way is the curve shown in Figure 24b. As shown in previous studies (Benavent-Climent, 2007), the skeleton curves in the positive and negative domains are almost coincident and can be approximated by a trilinear curve (plot with dash line in Figure 24b) that is characterized by the yield force Q_y , the yield displacement δ_y , the force corresponding to the onset of the second segment Q_B , the first plastic stiffness K_{p1} and the second plastic stiffness K_{p2} . Q_y and δ_y can be predicted from the geometry and the mechanical properties of the steel with the following equations (Benavent-Climent, 2010) based on fundamental principles of the strength of materials:

$$Q_y = \min \left\{ n \frac{f_y t w^2}{2h'}, n \frac{2f_y t w}{3\sqrt{3}} \right\} \quad (1)$$

$$Q_B = \min \left\{ n \frac{f_B t w^2}{2h'}, n \frac{2f_B t w}{3\sqrt{3}} \right\} \quad (2)$$

$$\delta_y = \frac{Q_y h'^3}{n E t w^3} \left(1 + 3 \ln \frac{h+2r}{h'} \right) + \frac{3 Q_y h'}{2 n t w G} \left(1 + \ln \frac{h+2r}{h'} \right) \quad (3)$$

Here, as shown in Figure 16b, w and h are the width and height of the strut, respectively, r is the radius of the end part of the strip, t is the thickness of the plate, n is the total number of strips and $h' = h + [2r2/(h+2r)]$. The maximum displacements in the skeleton part, in the positive and negative domains, are denoted herein by ${}_s\delta_i^+$ and ${}_s\delta_i^-$ (see Figure 24b).

The Bauschinger part is constituted by the segments that begin at $Q=0$ and terminate at the maximum load level previously attained, in preceding cycles in the same loading domain. Referring to Figure 24b, the Bauschinger part comprises the segments labelled as 4-5, 10-11, 16-17, 22-23, 28-29 in the positive domain, and 7-8, 13-14, 19-20, 25-26 in the negative domain of loading. In Figure 24a, segments 1-2, 6-7, 12-13, 18-19, 24-25, 30-31 in the positive domain and 3-4, 9-10, 15-16, 21-22, 27-28 in the negative domain are unloading paths whose slope (i.e. stiffness) coincides with the initial elastic stiffness $K_e (=Q_y/\delta_y)$. The Bauschinger part obtained in this way is shown in Figure 24c.

Up to a given point (Q_i, δ_i) of the Q - δ curve, the area enveloped by the skeleton curve in the positive and in the negative domains is respectively referred to herein as ${}_sW_i^+$ and ${}_sW_i^-$. Also, for each domain of loading, the areas enveloped by the Bauschinger part are referred to as ${}_B W_i^+$ and ${}_B W_i^-$. The sum

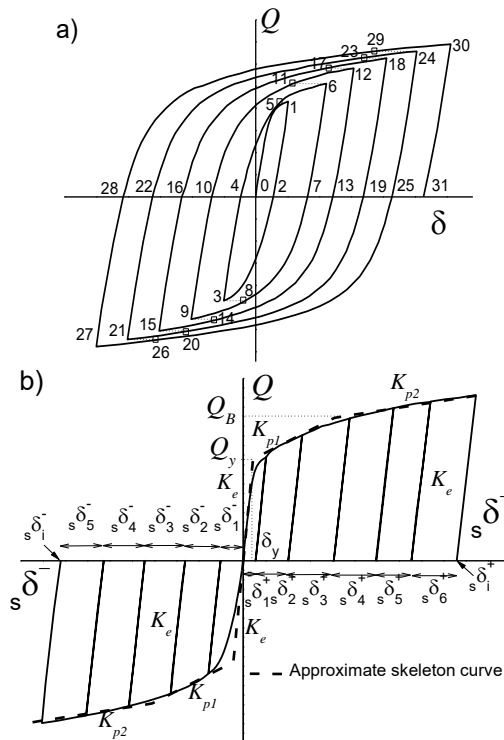
(${}_sW_i^+ + {}_B W_i^+$) in the positive domain, and (${}_sW_i^- + {}_B W_i^-$) in the negative domain, represent the total plastic strain energy dissipated by the damper in the positive and in the negative domains of loading. For convenience, above energies can be expressed in non-dimensional form by the following ratios:

$$\begin{aligned}
 {}_s\bar{\eta}_i^+ &= \frac{{}_sW_i^+}{Q_y\delta_y}; & {}_s\bar{\eta}_i^- &= \frac{{}_sW_i^-}{Q_y\delta_y}; & {}_B\bar{\eta}_i^+ &= \frac{{}_B W_i^+}{Q_y\delta_y}; & {}_B\bar{\eta}_i^- &= \frac{{}_B W_i^-}{Q_y\delta_y}, & \bar{\eta}_i^+ &= \frac{{}_sW_i^+ + {}_B W_i^+}{Q_y\delta_y}; & \bar{\eta}_i^- &= \frac{{}_sW_i^- + {}_B W_i^-}{Q_y\delta_y} \\
 {}_s\eta_i &= {}_s\bar{\eta}_i^+ + {}_s\bar{\eta}_i^-, & {}_B\eta_i &= {}_B\bar{\eta}_i^+ + {}_B\bar{\eta}_i^-, & \eta_i &= {}_s\eta_i + {}_B\eta_i
 \end{aligned} \quad (4)$$

and the maximum displacements in the skeleton part, ${}_s\delta_i^+$, ${}_s\delta_i^-$, can be normalized as follows:

$${}_{ep}\bar{\eta}_i^+ = \frac{{}_s\delta_i^+}{\delta_y}; \quad {}_{ep}\bar{\eta}_i^- = \frac{{}_s\delta_i^-}{\delta_y}; \quad {}_{ep}\eta_i = {}_{ep}\bar{\eta}_i^+ + {}_{ep}\bar{\eta}_i^- \quad (5)$$

The ultimate values of above paraments, i.e. when the metallic damper fails, will be denoted hereafter with the subindex u instead of i . They represent the (normalized) ultimate energy dissipation capacity of the damper. The ultimate energy dissipation capacity of the specimens TTD tested in terms of the ratios defined above is summarized in Table 4. The energy consumption path followed by each specimen until failure, in the ${}_{ep}\eta$ vs. ${}_s\eta$, ${}_{ep}\eta$ vs. ${}_B\eta$ and ${}_{ep}\eta$ vs. η spaces is plot in Figure 25 with red, green and blue lines. Also plotted with bold black lines (failure curve) is the prediction of the ultimate energy dissipation capacity of the TTD damper calculated following the model proposed in past studies (Benavent-Climent, 2007). As can be observed, the prediction fits very well with the results of the tests. The values of two key parameters that govern this prediction ($a=-13$ and $b=3900$) are also plotted in Figure 25.



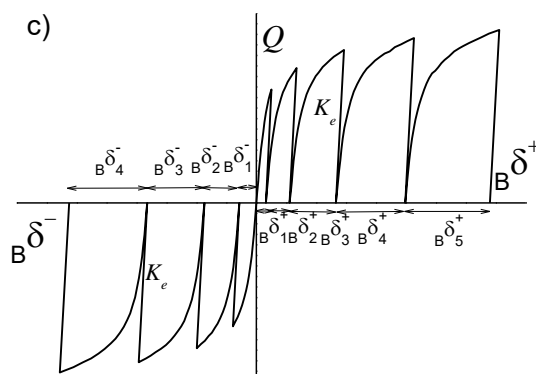


Figure 24: Decomposition of the force displacement, Q - δ , curve: a) entire Q - δ curve; b) skeleton part; c) Bauschinger part

Table 4: Ultimate energy dissipation capacity of TTD damper

Specimen	$ep\bar{\eta}_u^+$	$ep\bar{\eta}_u^-$	$s\bar{\eta}_u^+$	$s\bar{\eta}_u^-$	$B\bar{\eta}_u^+$	$B\bar{\eta}_u^-$	$\bar{\eta}_u^+$	$\bar{\eta}_u^-$	η_u	$B\eta / s\eta$
TTD5	17.6	19.3	37	41	1643	1611	1680	1652	3332	41.7
TTD6	22.5	28.4	54	66	1700	1633	1754	1699	3453	27.8
TTD4	9.3	6.5	16	10	1884	1856	1900	1866	3766	143.8

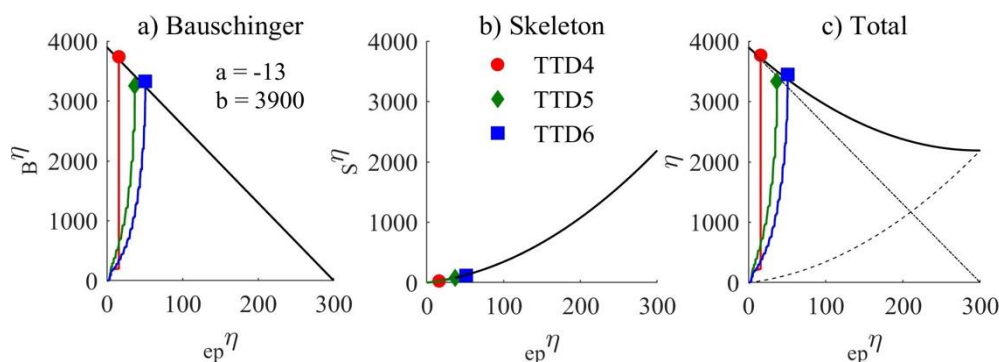


Figure 25: Ultimate energy dissipation capacity of the TTD damper and comparison with predictions

1.1.4.2 Numerical model for representing the cyclic behaviour of TTD part

The hysteretic behaviour of the TTD part under arbitrarily applied cyclic loadings can be predicted from the shape of the skeleton part and the shape of each segment of the Bauschinger part, applying the approach proposed in Benavent-Climent (2010). The shape of the skeleton part can be approximated with the trilinear curve characterized by parameters Q_y , δ_y , Q_B , K_{p1} and K_{p2} plot with dashed lines in Figure 24b. From the results of the tests $K_{p1}/K_e=0.4$ and $K_{p2}/K_e=1/14$, where $K_e=Q_y/\delta_y$. The shape of each Bauschinger part is modeled with two segments as shown with dot-dash lines in Figure 26a). The slope of the first segment is taken equal to the elastic stiffness K_e . The second segment is defined by two parameters: α and β . The first parameter, α , determines the ordinate Q' ($=\alpha Q_m$) of the point of change from the first to the second segment; here Q_m is the maximum force on the Bauschinger segment. α is determined imposing that the area under the Bauschinger segment equals the area of the bilinear model, as shown in Figure 26a. The relation between Q_m and Q' ($=\alpha Q_m$) calculated in this way for each Bauschinger segment obtained from the tests (both normalized by δ_y) is shown in Figure 26b. The points are approximately on a line with slope α . The second parameter, β ($=_B\delta/\Sigma_s\delta$) relates the amplitude of the plastic deformation on each Bauschinger segment $_B\delta$ (see Figure 26a), with the maximum plastic deformation cumulated in the skeleton part in the positive and negative domains of loading, $\Sigma_s\delta$, up to

the beginning of the Bauschinger segment. The relation between ${}_B\delta$ and $\Sigma_S\delta$ for each Bauschinger segment obtained from the tests (both normalized by δ_y) is shown in Figure 26c. The points are approximately on a line which slope is β . The values of parameters α and β proposed for modelling the TTD part of the new damper are $\alpha=0.4$ and $\beta=0.35$.

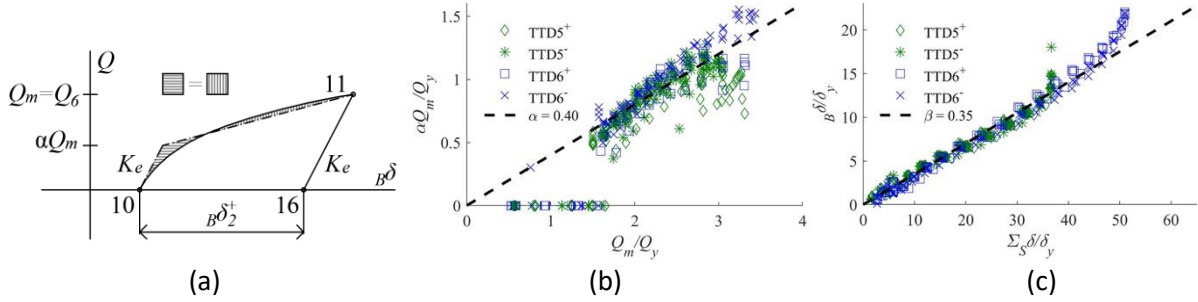


Figure 26: Model of Bauschinger part: (a) typical Bauschinger segment and bilinear approximation, (b) α values, (c) β values

1.1.5 Development of new Damping Corrections Factors

Site-specific elastic response spectrum defined for 5% damping ratio is a common way to characterize earthquake actions, and it is used in combination with the q-factor approach to design conventional structures. In conventional frames, the seismic energy is intended to be dissipated in a large number of regions (plastic hinges) distributed throughout the structure, and the fulfilment of local and global ductility conditions allows to reduce the elastic seismic forces by a factor q . In contrast, in buildings with Passive Energy Dissipation (PED) systems most of the energy input by the earthquake is intentionally dissipated (concentrated) in few elements (the dampers) and the q-factor approach is not appropriate. An alternative method already implemented in codes is the capacity spectrum method that uses equivalent properties and elastic response spectra, conveniently modified to account for high damping. Structures with PED systems exhibit equivalent damping ratios typically over 20% in the first mode, and up to about 90% in the upper modes. Appropriate damping correction factors (DCFs) are required to modify the 5% damped elastic response spectrum for such high levels of damping. To this end, new DCFs were derived using 880 European records. Special consideration has been made to issues such as the significant duration of the ground motion and the soil type.

Description of the study

SDOF systems of different natural period T (ranging from 0s to 4s) and viscous damping ratio ξ (from 10% to 90%) were subjected to several suites of recorded accelerograms using step-by-step time-history elastic analysis. For each record r , DCFs were defined for acceleration ${}^r\eta_a$, velocity ${}^r\eta_v$, and displacement ${}^r\eta_d$ as follows:

$${}^r\eta_a(T, \xi) = {}^rS_a(T, \xi) / {}^rS_a(T, 5\%) \quad (6)$$

$${}^r\eta_v(T, \xi) = {}^rS_v(T, \xi) / {}^rS_v(T, 5\%) \quad (7)$$

$${}^r\eta_d(T, \xi) = {}^rS_d(T, \xi) / {}^rS_d(T, 5\%) \quad (8)$$

where ${}^rS_a(T, 5\%)$ is the spectral absolute acceleration of the record for 5% damping and ${}^rS_a(T, \xi)$ for a damping ratio ξ ; ${}^rS_v(T, 5\%)$, ${}^rS_v(T, \xi)$ have similar meaning for the relative velocity, and ${}^rS_d(T, 5\%)$, ${}^rS_d(T, \xi)$ for the relative displacement. First, the records were classified in two groups according to the duration $D_{5-95\%}$ (i.e. $D_{5-95\%} \leq 16$ s and $D_{5-95\%} > 16$ s). The records with $D_{5-95\%} \leq 16$ s are associated with

regions of low-to-moderate seismicity (magnitude $M_s \leq 5.5$; Type 2 spectrum in EN1998). The records with $D_{5-95\%} > 16$ s are associated with regions of high seismicity (magnitude $M_s > 5.5$; Type 1 spectrum in EN1998). Second, the acceleration records within each group were classified according to the type of soil. Third, the DCFs defined with Eqs. (6), (7) and (8), were obtained through time-history analysis for each record r . Within each subgroup, the mean value for each period T was calculated and is denoted hereafter as $\eta_a(T, \xi)$, $\eta_v(T, \xi)$ and $\eta_d(T, \xi)$.

Results

Based on regression analysis, new expressions were proposed for predicting $\eta_a(T, \xi)$, $\eta_v(T, \xi)$ and $\eta_d(T, \xi)$ for different damping ratios ξ , periods T and type of soil. As an example, Figure 27 shows the mean values of $\eta_a(T, \xi)$ computed from the time-history analysis (solid line), and the proposed expressions (dashed line).

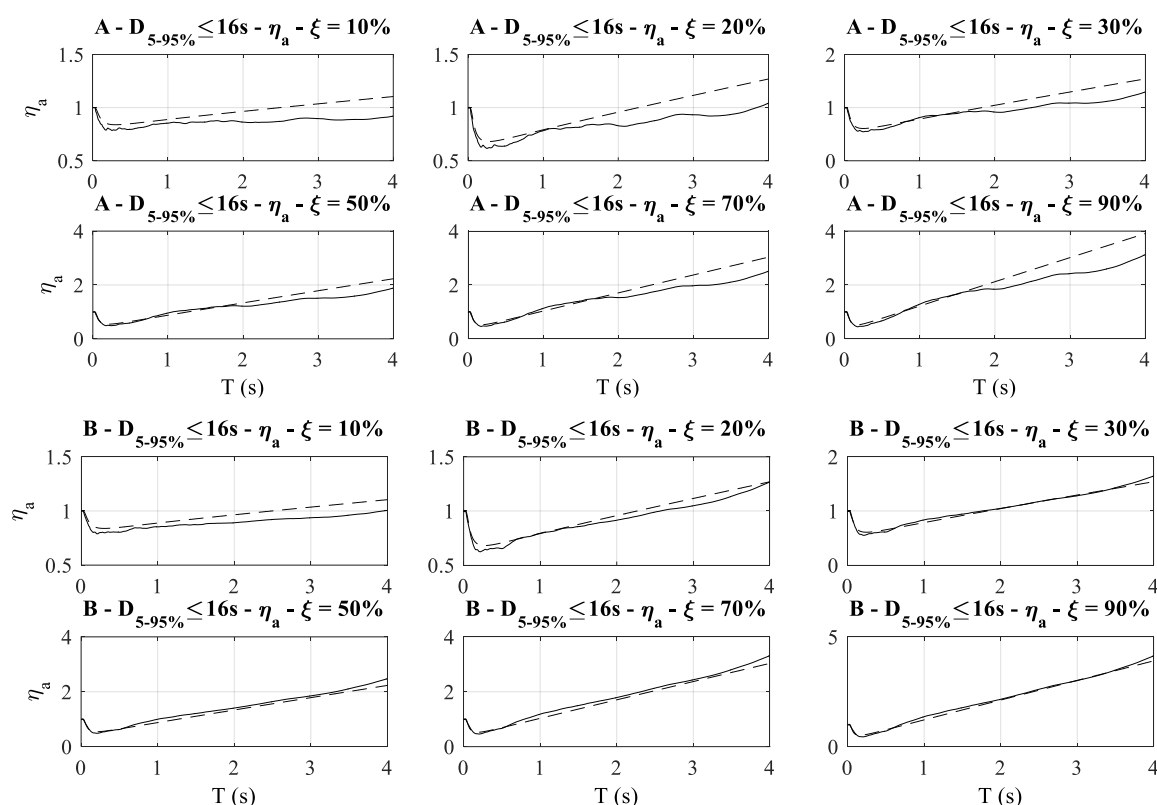


Figure 27: η_a for $D_{5-95\%} \leq 16s$. Actual values (solid line) vs. prediction (dashed line)

1.2 Tests on improved energy isolators equipped with smart materials

Seismic isolation of structures by means of introducing at their base devices with low horizontal stiffness, is widely used the last decades, especially in bridges. The most common devices are rubber bearings reinforced with thin steel plates in order to increase their vertical stiffness. All these years new types of bearings have been proposed tested and applied, aiming in improving specific characteristics of these bearings, mainly the horizontal stiffness and the damping.

Fibre-reinforced elastomeric isolators (FREIs), utilize fibre reinforcement laminates instead of steel shims. In this way the cost of production reduces significantly (due to the elimination of the vulcanization process), while the much lower weight compared to the steel-reinforced rubber bearings

results in reducing also transportation and installation cost. Moreover, the fibre cords are also flexible in bending, so when a FREI is loaded in shear, the plain cross-section becomes curved. This causes tension in the fibre reinforcement, which produces a frictional damping, resulting in a higher damping compared to that of the elastomer.

In typical applications of rubber bearings in general, elastomer is bonded on thick end steel plates rigidly connected to the structure. Eliminating these plates results in unbonded FREIs. Unbonded FREIs differentiate their behaviour in terms of stiffness, which can be distinguished in two phases. At moderate lateral displacements the top and bottom surfaces of the bearing loose contact to their supporting external plates, exhibiting a rollover deformation (*roll-out effect*). This leads to a decrease of the effective horizontal stiffness, called softening (Figure 28a). In larger lateral displacements the originally vertical faces of the bearing become horizontal and come in contact with the upper and lower supports (*roll-over effect*, Figure 28b). At this phase, there is an increase in the effective horizontal stiffness which can act as a self-restraining mechanism against displacements beyond design limits.

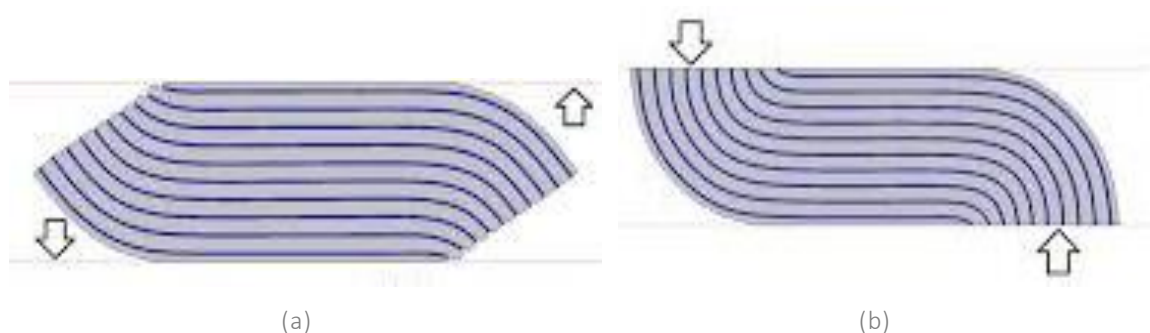


Figure 28: Phase 1 (a) and phase 2 (b) of the unbonded FREIs subjected to lateral displacements

Isolators built using layers of elastomer/rubber bonded with thin layers of bidirectional fibre fabric as reinforcement, are known as FREI (fibre reinforced elastomeric isolators) and can be encountered in two configurations: with un-bonded support conditions (their end phases are not bonded on the top plates on the foundation or the bottom plate of the structure above the isolator, U-FREI) or bonded ones (B-FREI). Both types have been studied both analytically (Kelly and Takhirov, 2001, Kelly and Takhirov, 2002, Nezhad et al., 2009a, Van Engelen et al. 2012, Vemuru et al. 2014) and experimentally (Kelly and Takhirov 2001 & 2002, Paulson et al. 1991, Nezhad et al. 2008), including studies of small buildings on shake tables (Nezhad et al., 2009b, Das et al. 2016).

Experimental results on unbonded isolators depict a stable roll-over deformation and enhanced efficiency of FREIs as compared to that of high-damping steel-reinforced ones. Moreover, light weight U-FREI can potentially provide superior performance in seismic isolation of low-rise buildings, utilizing stable roll-over displacement. Installation of FREIs at the superstructure-substructure interface of seismically vulnerable buildings, would be simple and hassle free.

It becomes obvious that experimental studies on FREI is rather limited in scope and to fully understand their response characteristics and contribution to seismic vulnerability reduction, they have to be tested in actual conditions involving real structures. As non-linear response is expected to develop only on FREIs, the rest of the full scaled building can be numerically represented, while FREIs are experimentally tested, i.e. via substructuring or hybrid simulation.

The main objectives of this work are to investigate the behaviour of such bearings and in particular the temperature effects developing during cycling at large deformations and how these can be encountered in a hybrid simulation framework.

1.2.1 Experimental program

1.2.1.1 Test specimens

The fibre reinforced elastomeric isolators tested (Figure 29) are of 200 mm diameter and of 45 mm total height – the effective height of the elastomer is 40 mm. The six isolators tested (in pairs, F44, F26a, F26b, see below) were of “Type 1” (i.e. for vertical load capacity up to 500kN).



Figure 29: FREIs used at the testing campaign

1.2.1.2 Test setup

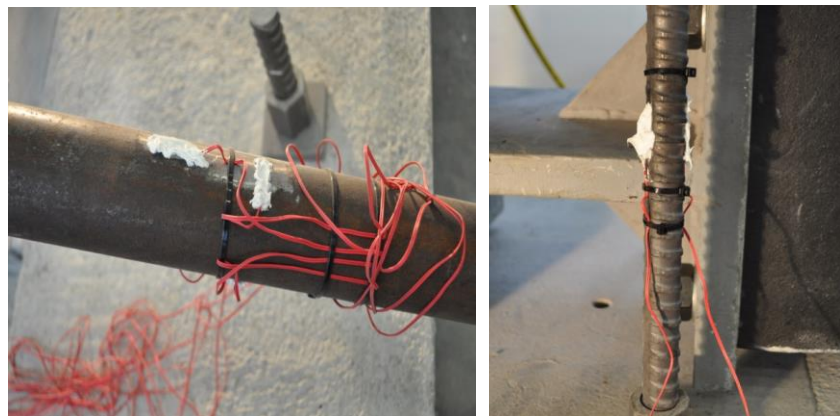
The test setup (Figure 30) consists of a pair of thick steel plates: the bottom one was anchored on the laboratory strong floor, while the top one rested on the isolators under test. Each pair of isolators is placed between the top and bottom thick steel plates, with another steel plate introduced between them. Thus, the isolators are tested in a “back-to-back” configuration, with a horizontal actuator driving the steel plate between the two bearings, forcing them to deform. The top plate is constrained not to move, thanks to four inclined steel arms – the vertical load of the superstructure is applied on this steel plate. An MTS dynamic actuator (± 250 mm stroke and ± 500 kN force capacities, servovalve of 1500 lt/min) imposed the horizontal displacements to the specimens. Four hollow Enerpac jacks imposed a vertical load of 375 kN on the top plate (75% of the vertical capacity of the bearings), which was kept constant during the test. The test sequence commenced by imposing the vertical load on the specimens, followed by the adjustment and placement of the 4 diagonal braces. With top steel plate been fixed, the axial load on the specimen fluctuates during test, due to the deformation of the bearings. Strain gauges were attached in all 4 diagonal braces and the vertical prestress rods passing through the hollow jacks, allow estimation of the exact axial load exerted (Figure 31).



(a)

(b)

Figure 30: Photos of test setup before (a) and during a test (b)



(a)

(b)

Figure 31: Installed strain gauges at the diagonal braces (a) and the prestress rods (b)

To measure the temperature fluctuation, 4 thermocouples were installed to each pair bearings, three at the bottom bearing and one at the top one. At the bottom bearing, two thermocouples were placed to the side of the bearing (90° in respect to the axis of horizontal deformation), one in the middle of the height and one close to the top surface of the bearing (5 mm from the top of the bearing), while the third was placed at the mid height in an axis forming an angle of 45° with respect to the axis of deformation (Figure 32a). The thermocouple at the top bearing was placed at its side in the mid height (Figure 32b). The thermocouples were glued inside 1 cm-deep holes at the outer surface of the bearings.

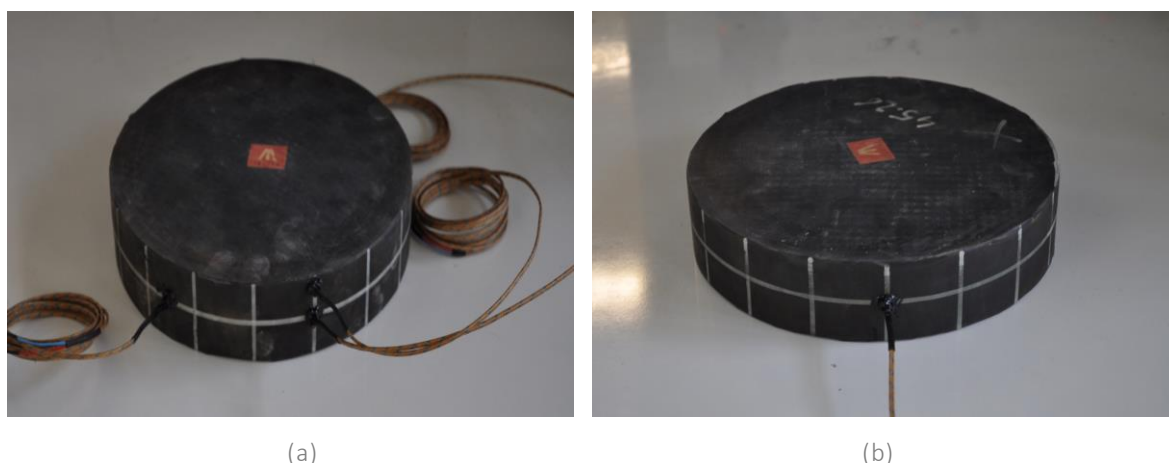


Figure 32: Installed thermocouples at the bottom bearing (a) and at the top bearing (b)

1.2.2 Test campaign

The **F44** pair of isolators was subjected to two cyclic tests with sinusoidally varying cycles of increasing amplitude, to investigate their performance in terms of stiffness and damping:

- o *Frb01* with amplitudes of ± 5 mm, ± 10 mm, ± 20 mm (shear strain $\gamma=50\%$) for the first test
- o *Frb02* with amplitudes of ± 20 mm, ± 30 mm, ± 40 mm, ± 50 mm, ± 60 mm ($\gamma=150\%$) for the second one

The **F26a** pair was first subjected to a repetition of tests on **F44**, for the sake of comparison. Subsequently, the same pair was subjected to a series of tests, to investigate their thermal behaviour at different levels of strain, deformation speed or number of cycles. In summary, the tests performed on the **F26a** pair of isolators are as follow:

- o *Frb03* same as test *frb01*
- o *Frb04* same as test *frb02*
- o *Frb05* with 80 sinusoidal cycles of amplitude ± 35 mm ($\gamma=87.5\%$)
- o *Frb06* with 40 sinusoidal cycles of amplitude ± 35 mm at half speed of test *frb05*
- o *Frb07* with 40 sinusoidal cycles of amplitude ± 35 mm at double speed of test *frb05*
- o *Frb08* with 40 sinusoidal cycles of amplitude ± 70 mm ($\gamma=175\%$) at half speed of test *frb05*

The test sequence was continued to the **F26b** pair, with the following tests been performed:

- o *Frb09* with 40 sinusoidal cycles of amplitude ± 70 mm at same speed as test *frb05*
 - o *Frb10* with 40 sinusoidal cycles of amplitude ± 70 mm ($\gamma=175\%$) at double speed of test *frb05*
- Frb04* same as test *frb02*

1.2.2.1 F44 isolators

Test frb01 – cyclic straining to shear strain up to 50%

Figure 33 and Figure 34 depict the imposed displacement history and the force- displacement response of **F44**, respectively.

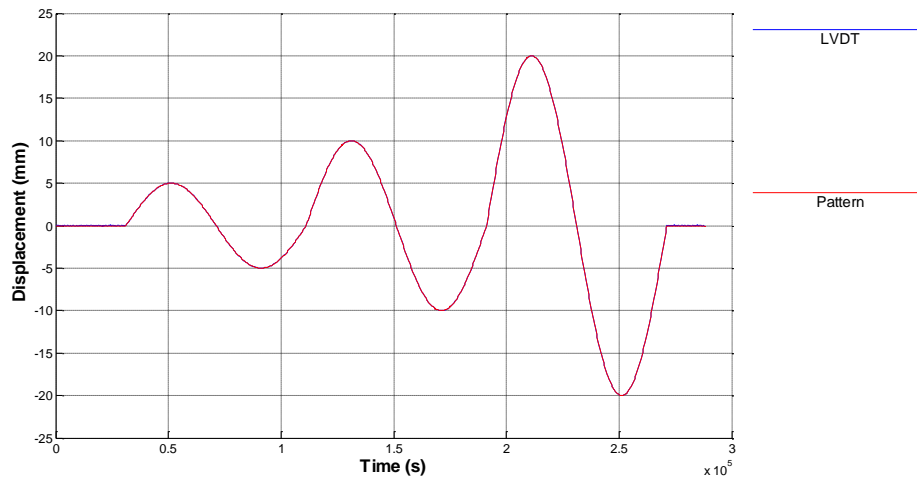


Figure 33: Displacement history of 3 sinusoidal cycles with amplitudes of ± 5 mm, ± 10 mm, ± 20 mm

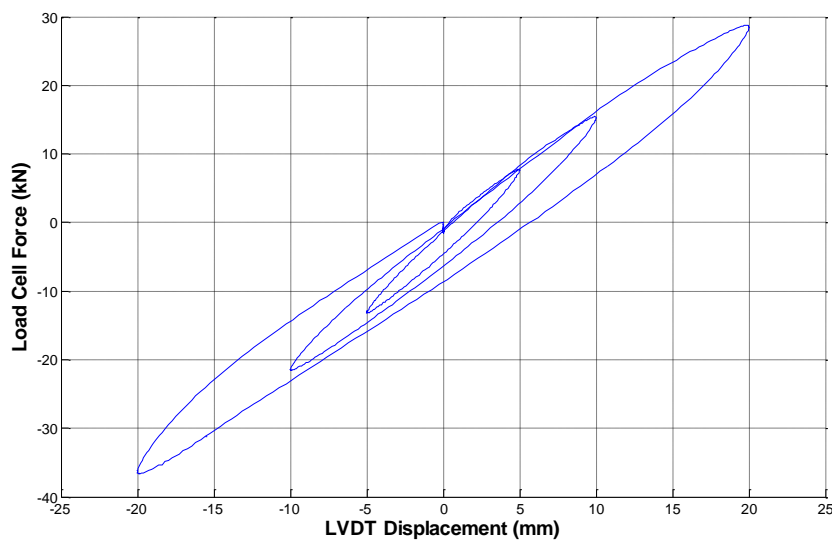


Figure 34: Force-displacement loops of test frb01

The fact that the top plate at the test setup was restrained through diagonal braces, caused a fluctuation of the vertical load on the bearings (Figure 35). With a vertical load of 375 kN been imposed, the fluctuation of the vertical load is less than 2% of the load imposed at the start of the test and its effect can be neglected.

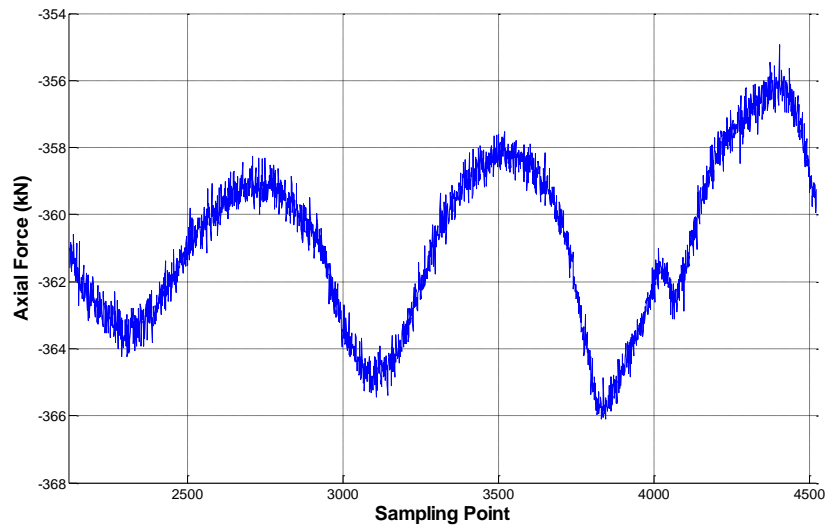


Figure 35: Vertical load fluctuation during test frb01

Test frb02 – cyclic straining to shear strain up to 150%

The loading pattern of this test consisted of 5 sinusoidal cycles of increasing displacement amplitudes of ± 20 mm, ± 30 mm, ± 40 mm, ± 50 mm and ± 60 mm – displacement history and the force-displacement response loops are presented in Figure 36 and Figure 37, respectively. In Figure 38 is presented a photo of the top bearing at -60 mm where the roll-out effect appears.

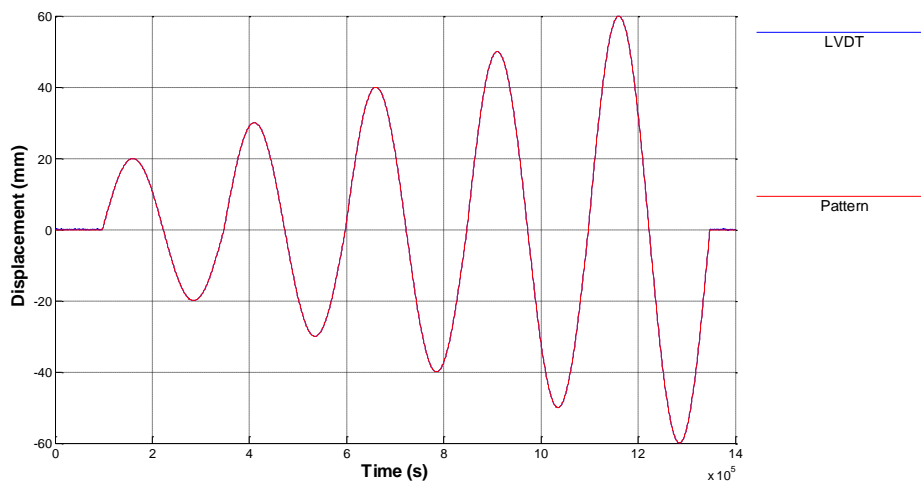


Figure 36: Displacement history of test frb02

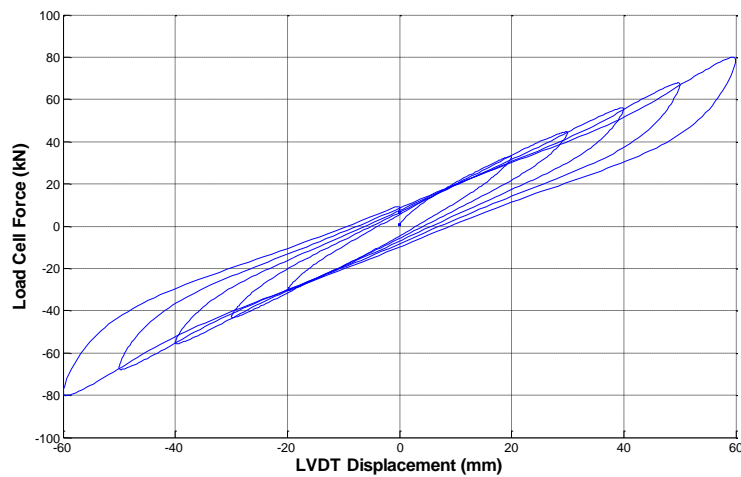


Figure 37: Force-displacement loops of test frb02



Figure 38: Photo of the top bearing in phase 1 (roll-out effect)

Due to the higher horizontal displacements (deformations up to 150% of the effective height of the bearing), the fluctuation (Figure 39) was also higher than in test frb01 – still very low (less than 7% of the initial load).

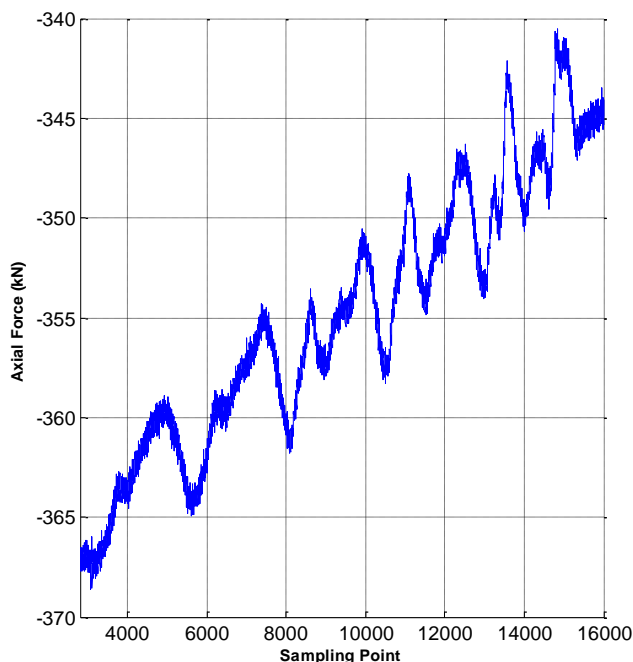


Figure 39: Vertical load fluctuation during test frb02

1.2.2.2 F26a isolators

Test frb03

This test is performed on F26a isolators with a loading sequence identical to that of test frb01. In terms of stiffness, the effective stiffness K_{eff} is calculated as:

$$K_{eff} = \frac{F_{max} - F_{min}}{u_{max} - u_{min}}$$

where F_{max} , F_{min} , u_{max} , u_{min} are the maximum and minimum force and displacement over each cycle, respectively. The force-displacement response in frb03, is presented in Figure 40. Comparing Figure 40 to Figure 34, a difference in the effective stiffness of less than 10% (at any displacement level) can be identified. It must be noted that the vertical axis in the graphs presents the force as acquired from the load-cell of the actuator. This force is related of the restoring force of both bearings tested back to back.

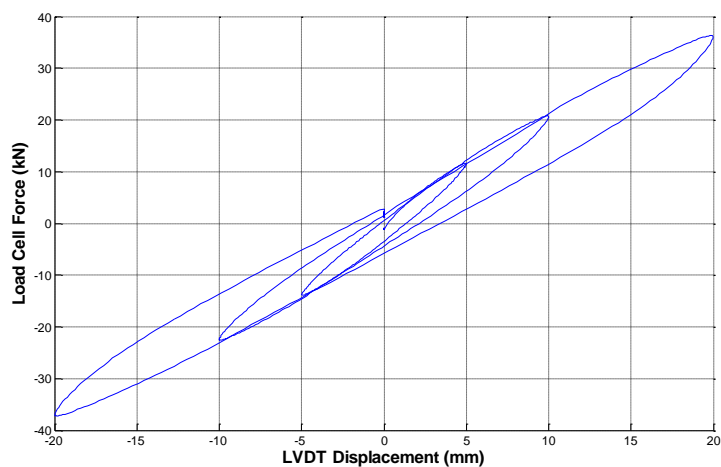


Figure 40: Force-displacement loops of test frb03

Test frb04

Under the same displacement pattern as in test frb02, the force-displacement response of the isolators is shown in Figure 41. When compared to the results of frb02 (Figure 37) it can be seen that the difference in the effective stiffness is less than 3% at any displacement level.

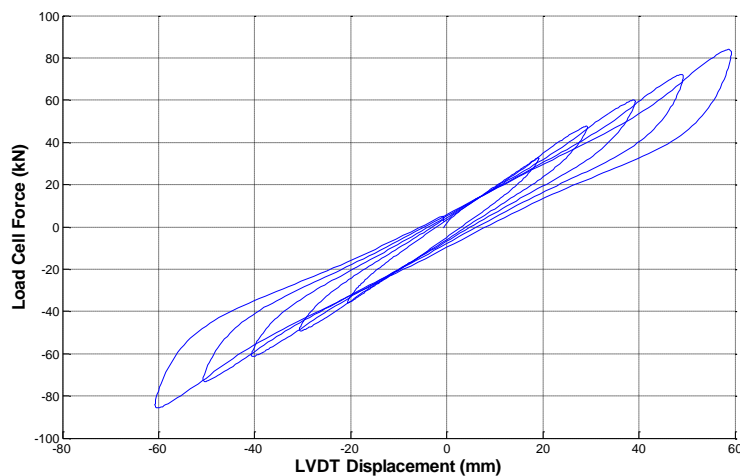


Figure 41: Force-displacement loops of test frb04

Test frb05

The loading pattern used for this test consisted of repeated sinusoidal cycles of amplitude ± 35 mm. First a set of 40 cycles was imposed and, after pausing for three minutes, another set of 40 cycles was imposed, resulting to a total of 80 cycles on same amplitude. Force-displacement loops for all cycles are included in Figure 42, while cycles 1, 2, 3, 70 and 80 are also plotted separately in Figure 43 (to allow investigating the effect past cycling may induce on the performance of the isolator). Following the first cycle, stiffness drops due to scragging effect and then remains practically unchanged, even after an appreciable number of cycles (70 or 80 cycles).

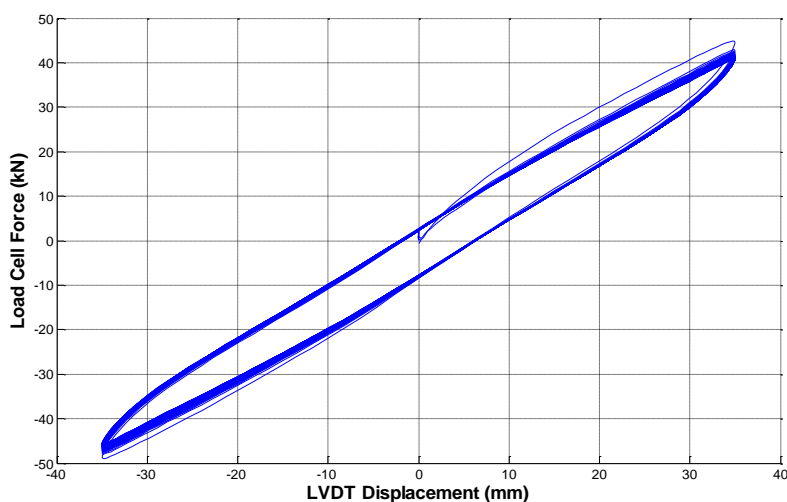


Figure 42: Force-displacement loops of test frb05

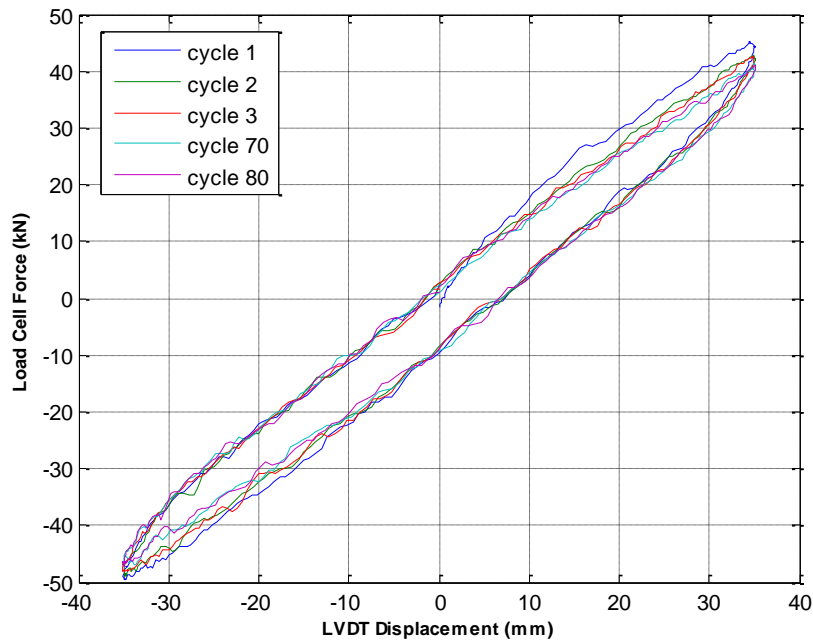


Figure 43: Force-displacement of the first and last cycles of test frb05

In Figure 44, the variation of temperature measured by the thermocouple at mid-height of the bottom bearing, is presented. The drop at the middle of the sampling points is due to the 3-minute break between the first and second set of cycles, described previously. It is worth noting that after 80 cycles of loading the temperature of the bearings raised only 4 °C.

Temperature increases with the deformation. To form a basis for comparison, Figure 45 presents the temperature at the positive peak of each cycle, thus representing the envelope of Figure 44.

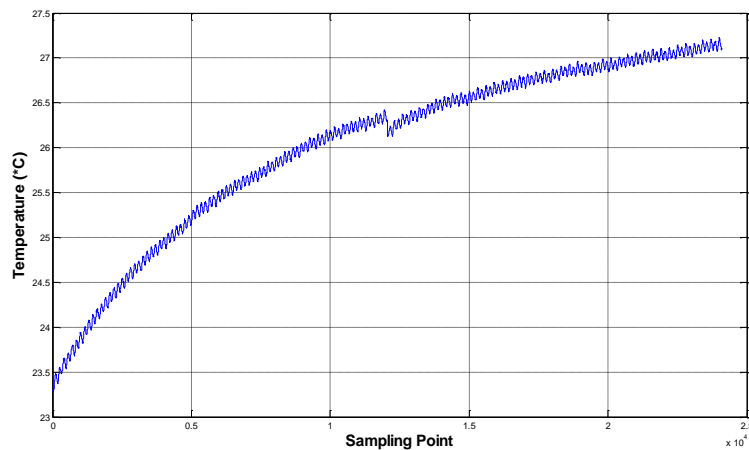


Figure 44: Temperature history of test frb05

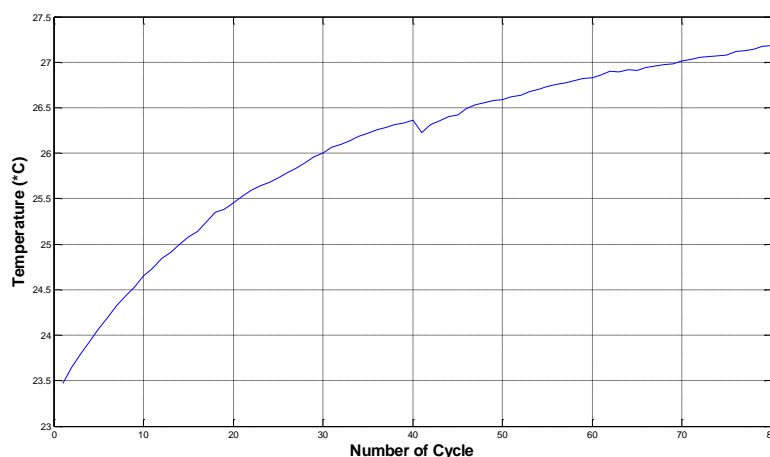


Figure 45: Contour of temperature history of test frb05

Comparison of tests frb05, frb06 and frb07

Test frb06 comprised 40 sinusoidal cycles of amplitude ± 35 mm at half the speed of test frb05, while test frb07 consisted 40 sinusoidal cycles of amplitude ± 35 mm at double the speed of test frb05. In Figure 46, a comparison of the first 40 cycles of test frb05 along those of tests frb06 and frb07, in terms of the temperature rise between each cycle, is being presented. It is obvious that the higher the speed of loading is, the higher is the temperature rise.

Figure 47 presents, for all three tests, the cycle-to-cycle drop in force. The larger drop in force occurs in test frb05 and not – as probably might have been expected – in frb07 under doubled speed of deformation. This may be attributed to the scragging effects: the bearings in test frb05 were almost virgin, and thus their first cycles of loading saw a higher force-drop. If one compares only tests frb06 and frb07 (where the scragging effect is not present), it is seen that they practically present the same behaviour, in terms of force decrease between cycles. Taking into account that the temperature rise in test frb07 was much higher than that in frb06 (Figure 46), one can safely conclude that the effect of heating on the stiffness of the isolator, can be neglected.

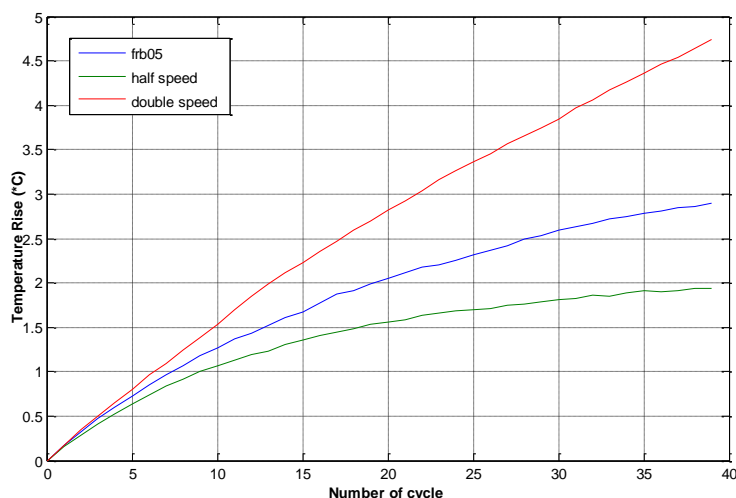


Figure 46: Comparison of temperature contour histories of tests frb05, frb06, frb07

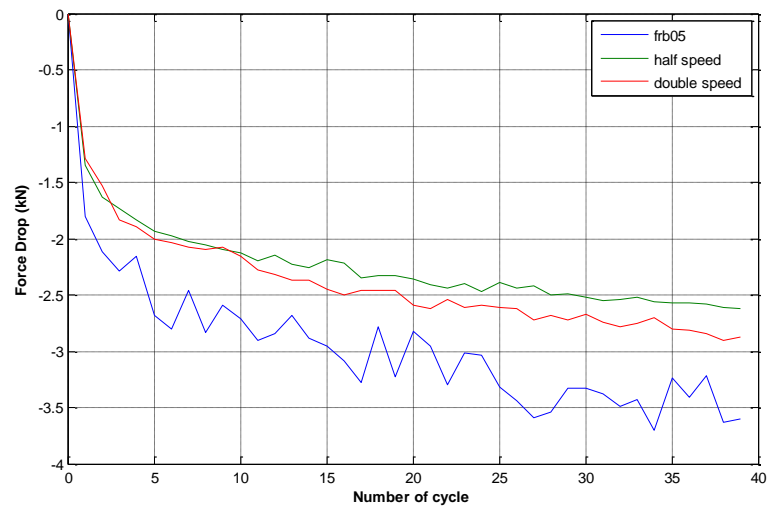


Figure 47: Comparison of force drop of tests frb05, frb06 (half speed), frb07 (double speed)

1.2.2.3 F26b isolators

In tests frb08, frb09 and frb10 the same loading pattern was imposed, comprising 40 sinusoidal cycles of a constant amplitude of ± 70 mm (shear deformation of $\gamma=175\%$). At such high deformation level rolling-over is observed (Figure 48), leading the stiffness into the hardening range (phase 2).

Test frb09 was carried out at a loading speed identical to that of test frb05, test frb08 at half-speed with respect to frb09 and test frb10 double the speed of frb9. After test frb08, which was carried out first, ruptures at the perimeter of both bearings were observed, exposing the fiber chords (Figure 49).

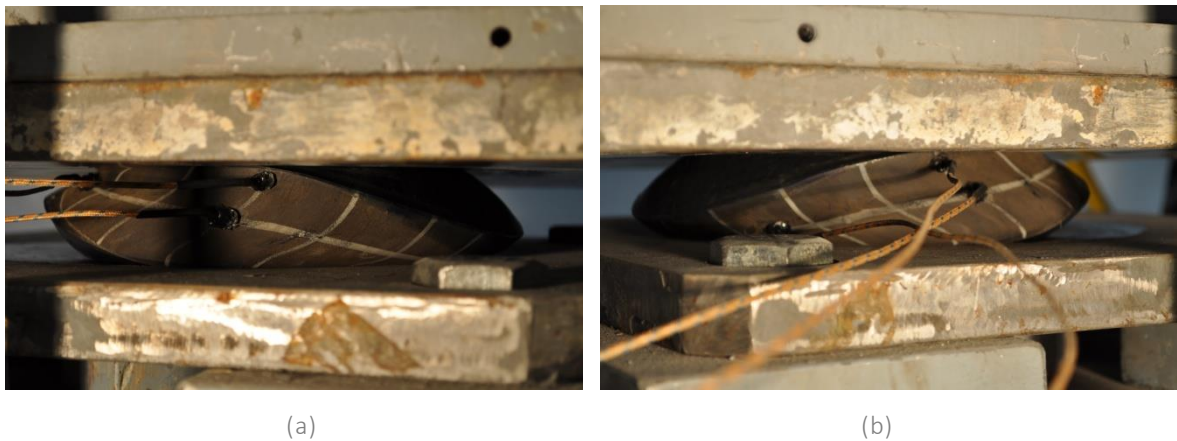


Figure 48: Photos of bearings in phase 2 ("roll-over") at maximum positive (a) and negative (b) displacement



Figure 49: Ruptures in bearing observed after test frb08

Thus, the bearings were switched with a virgin pair of the same type and tests frb09 and frb10 were repeated. Figure 50 presents results from tests frb08, frb09 and frb10 compared on the basis of the cycle-to-cycle rise in temperature, while Figure 51 depicts the force drop between each cycle. The results for high deformation-level cycling appreciably converge to the conclusion derived from test result under low deformation level (Figure 46 and Figure 47): temperature rise due to cycling of U-FRE isolators is small and its effect to the stiffness of the bearing can be considered negligible, irrespectively of whether the stiffness of the bearing is in phase 1 (roll-out effect) or phase 2 (roll-over effect).

On the basis of the above, the technique adopted for accounting for the strain-rate effects of isolators when hybrid simulation is performed, i.e. the correction of the reaction force on the basis of an a-priori calibration for force, displacement, rate of force and rate of displacement effect, can be safely employed for temperature effects developing when unbonded, fibre-reinforced isolators are cyclically (seismically) deformed from the “roll-out” too the “roll-over” phase of response.

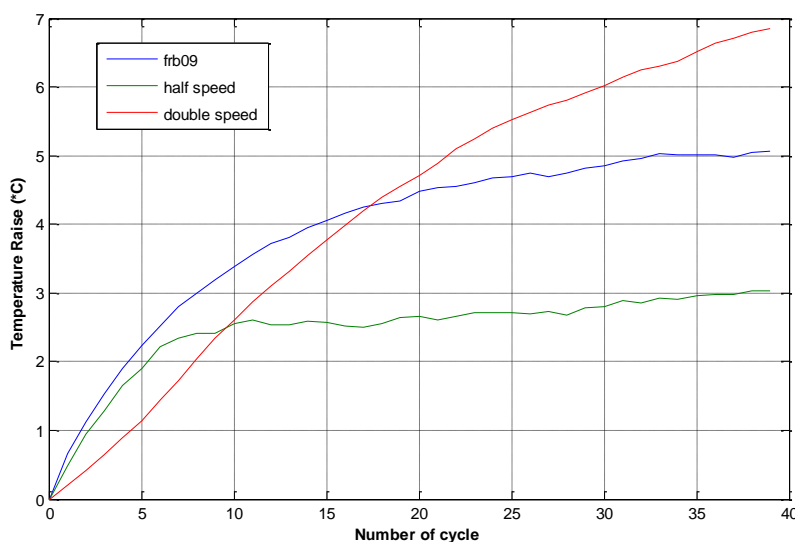


Figure 50: Comparison of temperature contour histories of tests frb08, frb09 (half speed), frb10 (double speed)

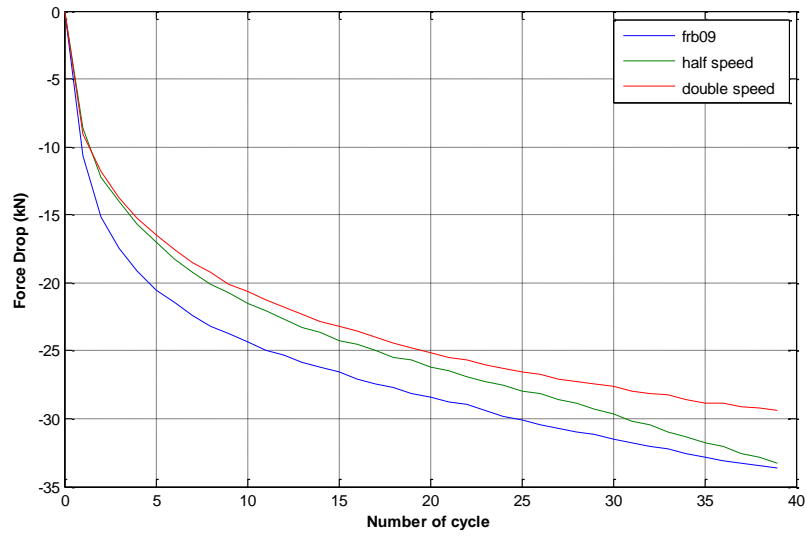


Figure 51: Comparison of temperature contour histories of tests frb08, frb09 (half speed), frb10 (double speed)

2 Soil-structure interaction analysis with HDS

2.1 Three-loop architecture framework for hybrid simulation

Two different schemes of hybrid simulation were developed at the Portuguese National Laboratory of Civil Engineering (LNEC). They were integrated into a single software package for ease of use. LabVIEW virtual instruments (VI) were used in constructing a state-machine based software framework to promote modularity and flexibility. The framework software is capable of executing slow and real-time hybrid tests.

The first scheme can be perceived as a three-loop architecture with a control loop as the innermost loop, simulation coordinator as an intermediate loop and integration loop as the outermost loop. The innermost loop is dedicated for controlling a servo-hydraulic actuator or shake table. The intermediate loop interacts with OpenFresco framework through a TCP/IP protocol while continuously generating command displacements.

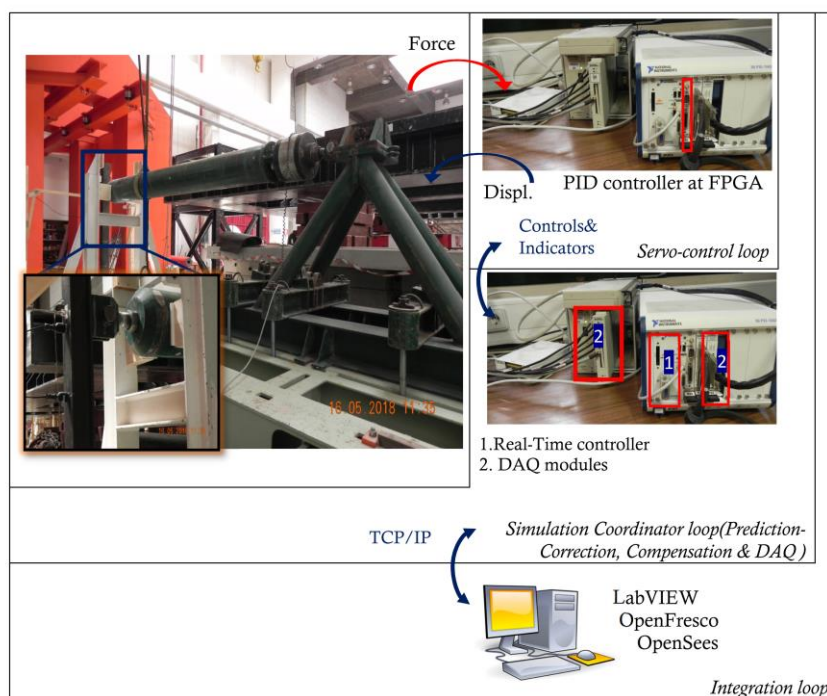


Figure 52: Three-loop architecture framework for HDS

Experimental errors are compensated in the intermediate loop through the adaptive compensation technique. In the current study, OpenSees, an open-source finite element software framework, together with OpenFresco middleware correspond to the outermost integration loop. OpenSees and OpenFresco are linked through TCP/IP communication protocol as well. The integration loop receives measured restoring force as a feedback and advances the numerical solution one-step forward in time.

The platform is built on the National Instruments (NI) hardware that constitutes an embedded Real Time (RT) controller, NI PXI-8106, and a Field Programmable Graphical Array (FPGA), NI PXI-7841R. The simulation coordinator is programmed in the RT controller while the PID control algorithm is executed in the FPGA module. Data acquisition board, NI PXI-6289, collects feedback displacement, acceleration

and actuator force that are measured by transducers. All the NI modules are connected into a NI PXI-1042Q chassis and communicate via Direct Access Memory (DMA) protocol. Although DMA FIFO provides a high throughput data transfer, rapid transfer of a small-sized data is essential during hybrid simulation. To this end, direct communication based on controls and indicators is an effective approach, thus improving the speed of execution of a hybrid test.

The second scheme in this framework software is also a three-loop configuration but excludes the need for an external finite-element software. A simple computational driver was programmed using LabVIEW programming environment and integrated into the simulation coordinator. This scheme eliminates the need for OpenFresco; thus, TCP/IP communication is not anymore used. Data is directly exchanged between the computational driver and simulation coordinator through local variables. Nevertheless, the computational driver is designed to model only two-dimensional linear-elastic numerical substructures with rigid end connection at floor levels, i.e. shear building. Therefore, a numerical substructure should essentially remain linear while an experimental element is tested to a desired level of inelasticity. This setup is highly convenient for structures with soft-storey mechanisms or soil-structure interaction problems where no or little structural nonlinearity is expected. The second scheme is referred as direct hybrid simulation (directHS) hereinafter. This scheme greatly improved the speed of test execution since TCP/IP communication between the simulation coordinator and the computational driver is replaced by a direct exchange of data. Real-time hybrid tests can therefore be realized in this mode of execution which could not be achieved in the first scheme. It should be noted that the speed of execution of a hybrid test in the second scheme may nevertheless be limited due to the limited clock-speed of the NI-RT controller.

The experimental substructure is driven by an actuator or a shake table depending on interface boundary conditions. During the validation process of the framework software, a steel column with a pin-ended connection at the top was driven by a shake table using a space truss and rod system in order to transfer the actuator's load to the experimental column.

The LabVIEW-based software framework for hybrid simulation is built from a Real-time VI (referred hereinafter as simulation coordinator VI), Host PC VI and FPGA VI. The state-flow is programmed into the simulation coordinator VI and calls the FPGA VI at each time-step during a hybrid test. The Host PC VI offers a real-time graphical visualization window for monitoring structural responses during hybrid simulation. Sub-space synchronization and tracking error plots can also be monitored from the Host PC VI.

2.1.1 OpenSees software framework

OpenSees is an open-source object-oriented finite element software framework for structural modelling and analysis. It is implemented in C++ programming language and has been widely used by the earthquake engineering community, both users and developers, across a wide range of applications. The transparent and modular nature of OpenSees allowed many users to modify and/or develop specific modules with little interaction with the rest of the framework (Fenves et al. 2004).

The framework for OpenSees has four main components namely: *Model builder*, *Domain*, *Analysis and Recorder*. Each component is associated with a unique operation. The model builder is responsible for constructing the objects in the model and adding them to the domain. It can add or remove objects from the domain anytime during the analysis. The current step and next-time step states of the model are kept and returned by the domain object. This makes the domain to act as a central object. This object is an aggregation of several other objects such as Node, Element, Load pattern, Single-point constraint, Multi-point constraint, etc. Once a model is built, the domain object is ready for analysis. The analysis object drives the model one time-step ahead and returns the state to the domain. The analysis object is constructed out of many sub-classes. Each sub-class is designed to do a specific analysis type such as Static analysis, Eigen analysis, Transient analysis, etc. On the other hand, the

recorder object monitors a user-defined parameter during the analysis process. The simulation results can therefore be visualized and post-processed after the analysis.

2.1.2 Middleware software

The Open Framework for Experimental Setup and Control (OpenFresco) is the middleware software that is adopted in the first scheme of the framework developed. It has an object-oriented architecture with two abstractions for experimental objects. These experimental objects are the loading system (commonly servo-hydraulic actuators), and the control and data acquisition system. The loading system imposes boundary conditions such as displacement, velocity, acceleration and force. The control system on the other hand commands the actuators based on target displacements received from the numerical substructure. The data acquisition (DAQ) object is responsible for collecting measured responses from transducers installed in an experimental setup.

According to the abstractions, an *ExperimentalSetup* class is defined. This class transforms response quantities from *ExperimentalElement* degrees of freedom into actuator degrees of freedom, using geometry and kinematics of the loading system. Transformations can be as simple as linear transformations (compatible with small displacements) or nonlinear algebraic transformations. Besides, the OpenSees software framework sends target displacements at control points, that are defined in OpenFresco, and receives measured restoring forces at different control points. The *ExperimentalControl* class of OpenFresco is responsible for defining the control points, direction of loading and actuator configuration. One-actuator control is adopted in this work consistently with a two-point control incorporated into a simulation coordinator. The *ExperimentalSite* class of OpenFresco facilitates the deployment of OpenFresco for a geographically distributed hybrid test.

The OpenFresco framework is capable of interacting with any finite element software as long as the software provides a means for modelling the experimental element. In the current study, OpenSees is adopted as a computational software. It has a comprehensive library of materials and elements necessary for modelling. Besides, new developments such as implementation of a new experimental element can be easily done. To facilitate the integration of OpenFresco and OpenSees for a hybrid test, Tcl programming commands that are necessary for defining OpenFresco Experimental classes were developed by Schellenberg et al. (2009).

To integrate OpenSees into the OpenFresco framework, the *ExperimentalElement* sub-class is added as a new abstract class into the existing element class. This abstract sub-class creates the interface between the OpenSees and OpenFresco (Schellenberg & Mahin, 2006). Through the inheritance principle, the *ExperimentalElement* inherits its property from the *Element* class. The *Element* class has a member function that sets the trial displacements at element degrees of freedom and returns the restoring forces. The trial displacement is then sent to a controller to be applied on a physical element and the corresponding restoring force, which should be computed by OpenSees, is measured using a force transducer and returned to OpenSees. The *ExperimentalElement* only returns initial stiffness of the physical element because it is difficult to compute tangent stiffness using forces that are measured at few points of the physical specimen. Kim (2011) modified the *ExperimentalSignalFilter* class of OpenFresco to compute tangent stiffness during a force-based hybrid simulation. This filter class was originally designed to filter control and DAQ response quantities and to simulate experimental errors such as overshoot, undershoot, lead, lag or random noise.

2.1.3 Simulation coordinator VI

The operation of the software framework starts at this VI. Users start the process from the *initialization* state whereby all input parameters to a hybrid test are initialized. A detailed description of all tasks executed in this state is presented in Table 5. Once the main pressure that drives an actuator, or a shake table, achieves a working pressure level (1000 psi in the current study), user prompts to *Start-up* state

by pressing a hydraulic service manifold (HSM) button. The Start-up state allows the physical substructure to remain in current position. This state is useful when stopping a hybrid test for various reasons or resuming a test after some time. Among many other tasks, the control loop at the FPGA comes into effect by pressing the *start-control-loop* button.

Table 5: Initialization state

<i>Initialization</i>				
Previous state	Main function	Auxiliary function	Next state	Condition
No state	<ul style="list-style-type: none"> ✚ Initializes: ➤ PID gains ➤ Transducers calibration data ➤ TCP/IP parameters ➤ Actuator data etc. ✚ Resets and runs FPGA ✚ Passes control parameters to FPGA 	<ul style="list-style-type: none"> ✚ Disables: ➤ Actuator initial position ➤ Next button ➤ Stop button ➤ Start-control-loop button ➤ Emergency stop button 	Start-up	HSM button

The current position of an actuator or a shake table can be adjusted prior to a hybrid test so that the loading system is properly connected to a test structure. Besides, hybrid test of a structure with an initial drift may be of interest. For example, a hybrid test simulating post-earthquake damage can be carried out using a residual drift. The *Centering* state is designed to carry out this initial positioning of the actuator. During this operation, a command displacement is generated in the form of ramp at rate of 0.5 mm/s.

Table 6: Start-up state

<i>Start-up</i>				
Previous state	Main function	Auxiliary function	Next state	Condition
Initialization	<ul style="list-style-type: none"> ✚ Starts FPGA control loop ✚ Keeps an actuator in its current position ✚ Displays measurements ✚ Sets HS parameters: ➤ FE time-step ➤ Compensator data ➤ PreCor algorithm, etc. 	<ul style="list-style-type: none"> ✚ Disables: ➤ PID gains ➤ TCP/IP parameters ✚ Enables/disables: ➤ HS input data ➤ Actuator data ✚ Enables: ➤ Next ➤ Stop ➤ Actuator Initial position 	Centering	Both start-control-loop & Next buttons
			Stop	Stop button

At the end of a successful or interrupted hybrid test, the software framework automatically returns to the centering state. User can then execute another hybrid test or terminate the test. *Next* button allows the user to continue doing more hybrid tests while *stop* button sends the actuator to halt whereby the hydraulic pressure is dropped from high to low pressure and ultimately to zero pressure. In addition to pressing the *Next* button, user needs to change the TCP/IP port, in the front panel, every time a new hybrid test is executed when the software continuously running. This is due to the LabVIEW TCP listen VI reserving a TCP port, for an extended amount of time, after the port being closed. It should be noted that the need to alter TCP ports is only necessary for the middleware-based scheme of the framework. The maximum number of sequential hybrid tests within the middleware-based framework is limited to 16 for economy of port utilization.

Table 7: Centering state

<i>Centering</i>				
Previous state	Main function	Auxiliary function	Next state	Condition
Start-up	<ul style="list-style-type: none"> ✚ Applies ramp displacement ✚ Records cell force offset ✚ Displays measurements ✚ Checks limits ✚ Launches DAQ at Host PC 	<ul style="list-style-type: none"> ✚ Re-initializes: <ul style="list-style-type: none"> ➤ Limiting parameters ➤ TCP error ➤ Success button ✚ Disables: <ul style="list-style-type: none"> ➤ Stop button ➤ Next button 	Pre-run/ Pre-directHS	Next button
			Start-up	<ul style="list-style-type: none"> ✚ Stop button ✚ Errors in FPGA ✚ Limit exceeded

At the end of this state, proper functioning of FPGA module, DAQ system and actuator position in relation to its limits are checked; and reported to the control panel.

Table 8: Pre-run state

<i>Pre-run</i>				
Previous state	Main function	Auxiliary function	Next state	Condition
<ul style="list-style-type: none"> ✚ Centering ✚ DAQ VI started 	<ul style="list-style-type: none"> ✚ Checks FPGA and TCP/IP errors ✚ Listens for OpenFresco connection ✚ Saves test configuration data into the host PC ✚ Creates queues for PreCor state ✚ Changes TCP/IP port 	<ul style="list-style-type: none"> ✚ Disables DAQ frequency input ✚ Initializes controls used at PreCor ✚ Error handling 	PreCor	<ul style="list-style-type: none"> ✚ User prompt ✚ No errors in FPGA & TCP/IP
			Stop	Errors in FPGA or TCP/IP

The Pre-run state is built only in support of the middleware-based scheme of the software. This state creates a TCP/IP listener for OpenFresco and initializes a group of queues that are necessary during the prediction-correction process of a subsequent state in the framework. The TCP/IP listener listens at a specified IP port for a duration of 3 s before timing-out. If OpenFresco fails to open the port, defined at the Pre-run state, within the 3 s time duration; or the port is already reserved by the TCP/IP listener VI, the software automatically switches to Error state. Final limit checks are also conducted at this stage before starting a hybrid test.

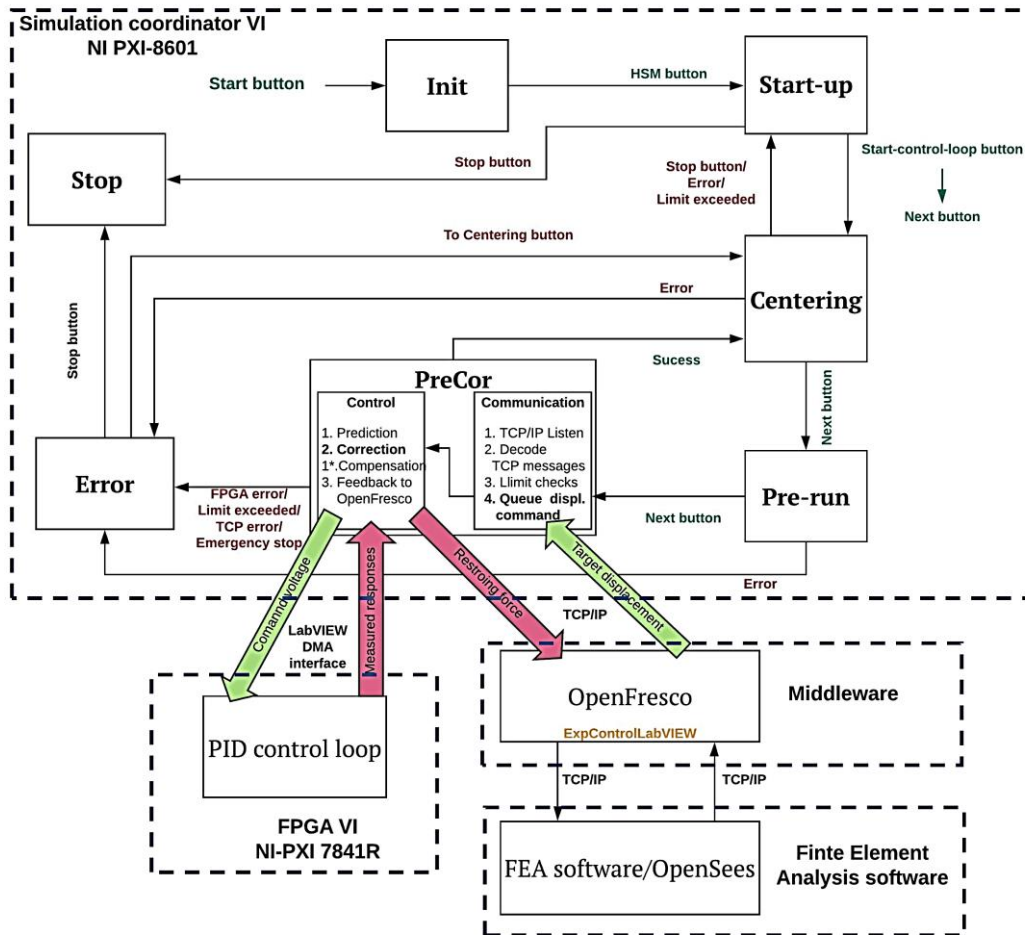


Figure 53: Schematic diagram of the middleware-based scheme

Prediction-Correction state (*PreCor*) is the most important and complex part of the software. Hybrid test is executed in this state given all preceding states are successfully completed without errors. PreCor can be decomposed into three blocks, namely: communication/interface block, control & feedback block and data acquisition block. The interface block allows the simulation coordinator VI to receive TCP/IP messages from OpenFresco, decode the messages and check commands generated by OpenFresco are in the range of the actuator’s stroke limit. Command displacements are queued to be utilized during the correction phase of the command generation. The control and feedback block of PreCor state predicts commands using displacements from previous time-steps until the target displacement for the next time-step is available.

The algorithm predicts for a duration of 60% of the time-step and corrects during the remaining 40% of the time-step. This assumes that the target displacement is available after 60% of the time-step. Prediction-correction process is explained in detail in a subsequent section. Additionally, the DAQ loop operates in parallel to the control and communication blocks. It is responsible for displaying measured

responses in real-time and sending measured responses to the Host PC for saving. Data is buffered for a duration 0.1 s and routed to HOST PC via LabVIEW network-shared variables. This state also supports other auxiliary tasks such as emergency stop.

Error state maintains an actuator in its current position before user decides to continue or terminate a test. The state-flow allows the program to jump from PreCor state to Error state if actuator’s limit is exceeded, control error is encountered (communication block errors) or emergency stop button is turned on. Once on this state, user can bring the test to halt or return to the centering state.

Table 9: PreCor state

<i>PreCor</i>				
Previous state	Main function	Auxiliary function	Next state	Condition
Pre-run	<ul style="list-style-type: none"> ✚ Continuous generation of commands via prediction-correction ✚ Receive target displacement from OpenFresco ✚ Command compensation ✚ Returns measured force and displacement to OpenFresco ✚ Data acquisition and displaying responses ✚ Sends measured responses to Host PC ✚ Tracks experimental errors ✚ Stops a test in case of emergency 	<ul style="list-style-type: none"> ✚ Displays measured responses ✚ Closes TCP/IP ports at the end of a test ✚ Reports messages from OpenFresco ✚ Stops DAQ at the end of a test 	Centering	Successful hybrid test
			Error	<ul style="list-style-type: none"> ✚ TCP/IP error ✚ Control error ✚ Dispatch error to OpenFresco ✚ Emergency stop

Input parameters that may be responsible for causing errors in the PreCor state may be adjusted after returning to the centering state. This state re-initializes all PreCor indicators in preparation for a new test. A schematic representation of data flow and interaction among states in the software framework developed are presented in Figure 53 and Figure 54.

Table 10: Error state

<i>Error</i>				
Previous state	Main function	Auxiliary function	Next state	condition
<ul style="list-style-type: none"> ✚ Pre-run ✚ PreCor 	<ul style="list-style-type: none"> ✚ Keeps an actuator in its current position ✚ Closes TCP/IP connection ✚ Displays error source ✚ Returns to centering 	<ul style="list-style-type: none"> ✚ Enables: <ul style="list-style-type: none"> ➤ Actuator parameters ➤ Stop button ➤ Re-initialize indicators 	Start-up	To Centering button
			Stop	Stop button

The second scheme includes neither an external FEA software nor a middleware software (i.e. OpenFresco). In order to operate the *directHS* scheme of this software, *directHS* button is pressed, otherwise program defaults to the OpenFresco-based hybrid testing. The two schemes have similar data flow during their operation except for the pre-run and PreCor states. When *directHS* button is true, the software prompts from centering state to *pre-directHS* state. This state has similar objectives as that of the Pre-run state. Preparatory actions are taken in this state prior to a *directHS* state whereby a hybrid test is conducted.

At pre-*directHS* state, user is prompted to select a ground motion input file, in the form of an acceleration and/or a displacement time-history. This input acceleration is directly applied to a physical substructure by a shake table controller with acceleration tracking capability or the ground displacement is feed to a PID-based displacement controller of the shake table. Both shake table controllers operate in cascade to the PID-based displacement control loop coded to the FPGA.

Table 11: Pre-*directHS* state

<i>Pre-directHS</i>				
Previous state	Main function	Auxiliary function	Next state	condition
Centering	<ul style="list-style-type: none"> ✚ Prompts user for input acceleration and/or displacement file ✚ Defines numerical sub-structure properties ✚ Updates control parameters ✚ Records measurement offsets 	<ul style="list-style-type: none"> ✚ Disables control parameters ✚ Write configuration file ✚ Re-initialize indicators ✚ Checks errors 	directHS	Next button
			Error	<ul style="list-style-type: none"> ✚ Error indicators ✚ User declines a prompt

Like the PreCor state, the directHS state has control and data acquisition loops running in parallel. Besides, a Newmark integration-based solver for the numerical substructure is executed in this state.

Table 12: directHS state

<i>directHS</i>				
Previous state	Main function	Auxiliary function	Next state	condition
Pre-directHS	<ul style="list-style-type: none"> ✚ Shake table control ✚ Equivalent force control ✚ Numerical solution ✚ Data acquisition ✚ Stops a test in case of emergency 	<ul style="list-style-type: none"> ✚ Filtering and averaging acceleration feedback ✚ Stops DAQ ✚ Checks errors 	Centering	Successful hybrid test
	Error		<ul style="list-style-type: none"> ✚ Error indicators ✚ Emergency stop 	

The PreCor method has a single control loop while this scheme hosts two control loops, equivalent force controller and shake table controller.

The two control loops in directHS state need to be synchronized during their parallel operation. The equivalent force controller that is responsible for matching shear force, computed by the numerical solver, at the base of a numerical substructure. Two algorithms are currently available for the equivalent force control, Smith-predictor and ATS-based controller. The shake table controller can be operated by matching ground displacement or by directly tracking ground acceleration.

Model-based controllers using the Linear quadratic Gaussian controller (LQG) together with a Feedforward controller works as Feedforward-Feedback controllers in minimizing tracking errors for the input acceleration to a shake table. A separate report enunciates the control algorithms developed for the directHS state. The tuning process of this controller is challenging and, thus, an additional displacement-based control was implemented. The latter requires the user to supply ground displacement input file. This input file can be prepared offline by double integrating the acceleration time-history after base-line filtering. A discussion on precautions needed while calculating ground displacement from acceleration records can be found in Boore (2001) and Boore et al. (2002).

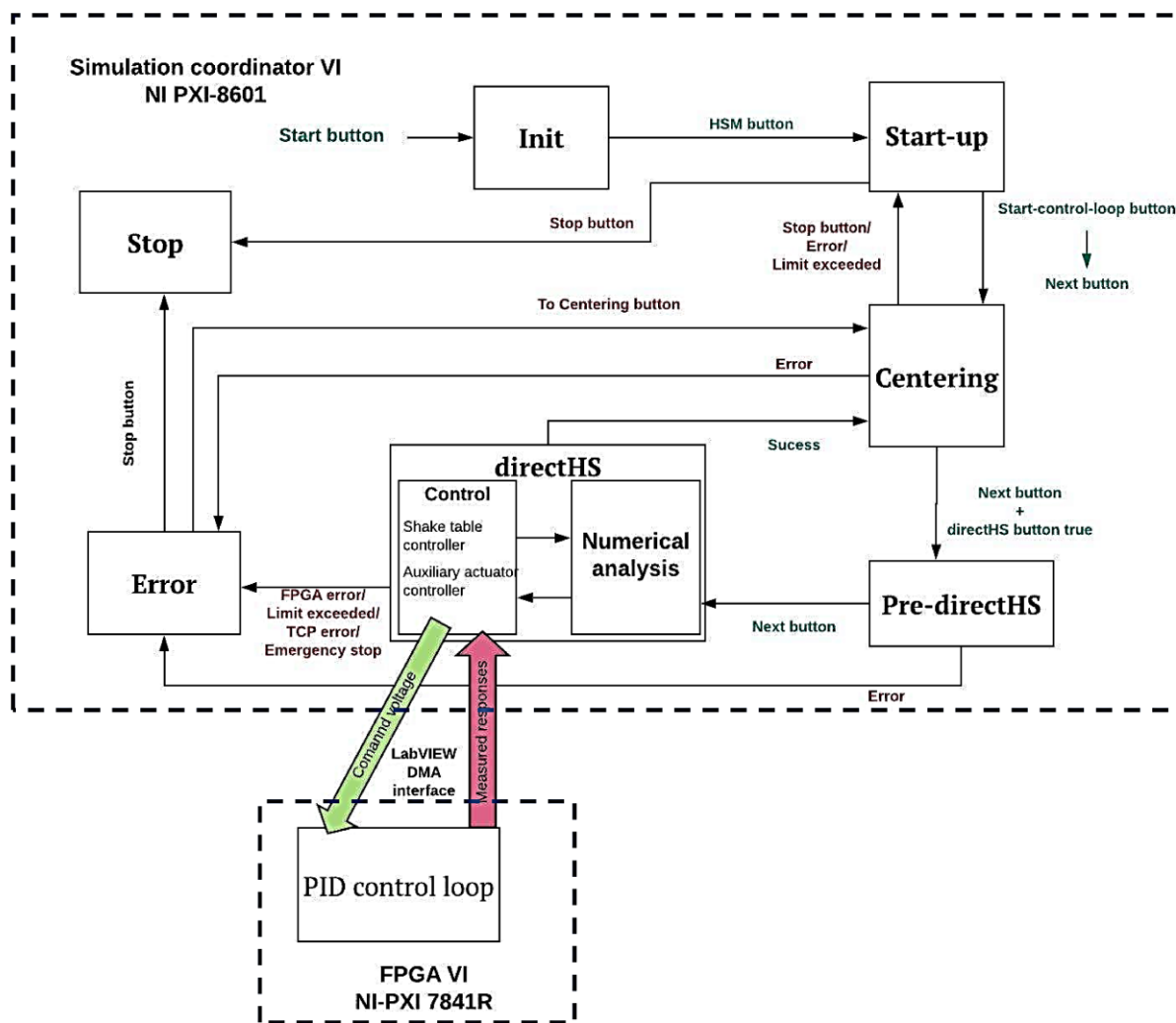


Figure 54: Schematic diagram of the middleware-free scheme

2.1.4 FPGA VI

The control algorithm of the software framework is developed in the NI PXI-7841R FPGA target to achieve determinism and high-rate of execution. The current implementation uses a proportional–integral–derivative (PID) controller algorithm. The PID algorithm works with single-precision floating-number to achieve accuracy in the position of the actuator. The algorithm uses integral anti-windup to overcome large accumulation of errors that can be caused by a large change in the setpoint. The PID algorithm also features bump-less controller output for PID gain changes.

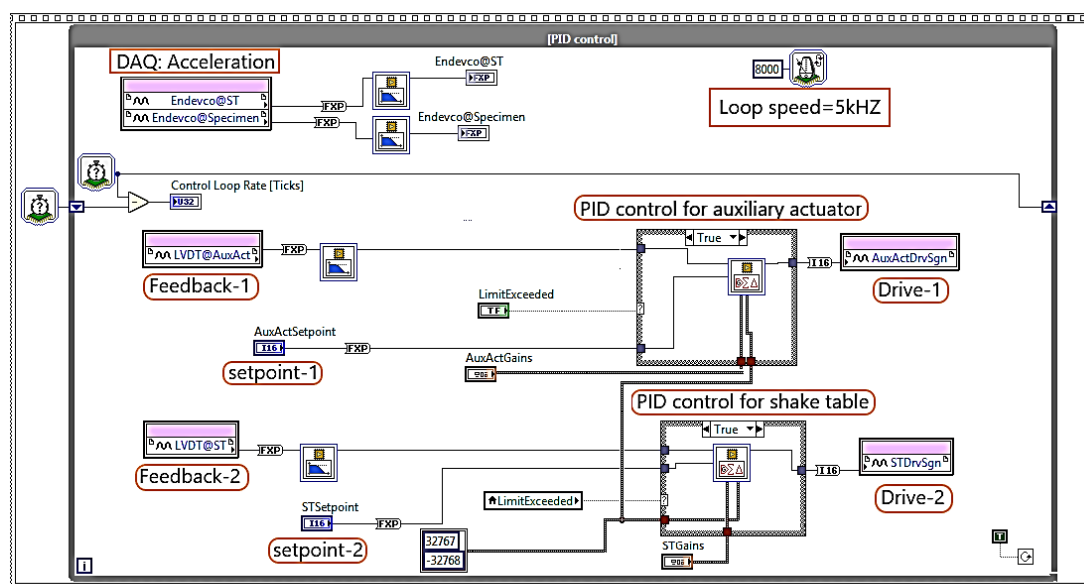


Figure 55: PID control loop at FPGA

The loading system in directHS scheme includes an actuator and a shake table and hence two PIDs are necessary. The two PID VIs are executed in parallel at the FPGA module – one driving the auxiliary actuator and a second one driving the shake table, as shown in Figure 55. Two setpoints are sent to the control loop and, at the same time, two feedback displacements are acquired. The feedback displacements were filtered by a low-pass 2nd order Butterworth filter at 200 Hz to reduce noise in the measured feedback displacement. When operating under the middleware-based scheme, the software works either with the shake table controller or the auxiliary actuator controller (i.e. the second drive is disconnected physically).

Actuator stroke limits are checked at RT host and a Boolean indicator, *LimitExceeded*, is sent to the FPGA VI. The Boolean indicator decides whether to execute the PID loop or not. In case of exceedance, the current position is sent to the drive signal and actuators are kept at their current position while, simultaneously, the RT host switches to the Error state. In order to use FPGA resources properly, data acquisition of acceleration transducers (ENDEVCO) are also carried out at the PID loop. The control loop has an execution speed of 5 kHz (2×10^{-4} s).

PID gains are commonly tuned so that the output-input relationship of the controller is approximately one. A 10 mm square signal at 1 Hz frequency was adopted for characterizing the step-response of the PID controller. During this test, the LNEC's uniaxial shake table (ST1D) was rigidly attached to a mass-block weighing 600 kg. The proportional gain of the controller was adjusted to yield an overshoot error below 5% and a settling time of 50 ms. The integral gain was set to a very small value due to stability problems identified during the tuning process. The derivative term, in theory, facilitates convergence, i.e., reduces settling time. However, it can also result in excessive volatility – spikes in the controller output's behavior often referred to as derivative kick. To this end, the derivative term was set to zero during the characterization and subsequent hybrid test experiments.

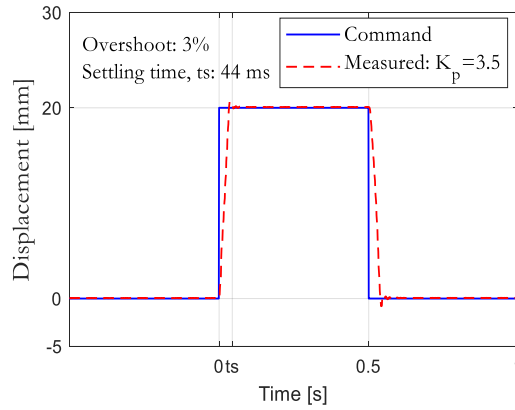


Figure 56: Tuning the PID controller

A band-limited white noise, 0-20 Hz frequency range, was applied in estimating the frequency response function (FRF) of ST1D. The characterization noise has 1 mm RMS value and a 10% cosine-taper, on both ends, for smooth transition of the controller.

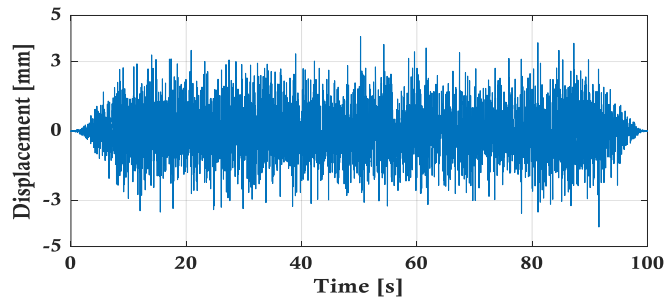


Figure 57: Band-limited White Noise signal at 1 mm RMS

The shake table has unity gain in the frequency range 0-6 Hz, as shown in Figure 58, which is reasonably adequate for the current application.

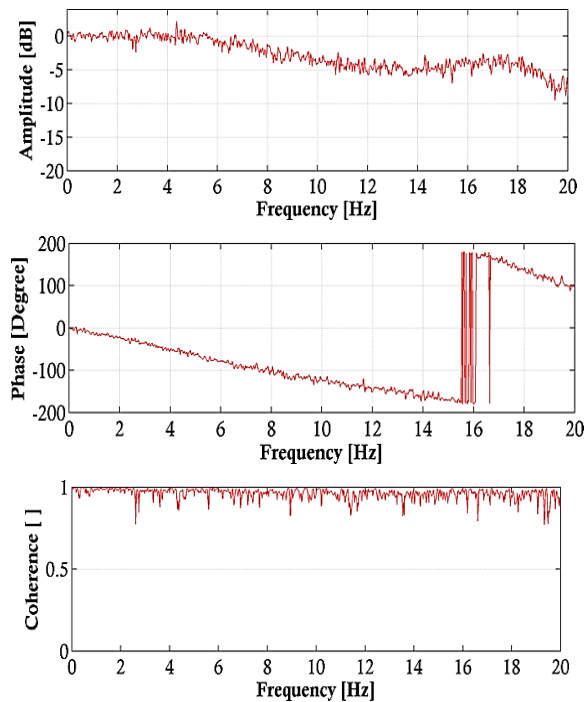


Figure 58: ST1D frequency response

As shown in Figure 58, the FRF magnitude drops by 5 dB (more than half of the original magnitude) at 14 Hz calling the need for an improved PID tuning for structures operating at this range. But again, the current FRF can be altered by control-structure-interaction (CSI) while testing a non-rigid structure; therefore, adaptive compensation is indispensable. The coherence values obtained indicate a reliable estimate of the FRF over the entire frequency range of interest.

2.1.5 LabVIEW based TCP/IP interface

The communication block in PreCor state is programmed to interface with OpenFresco via a TCP/IP network protocol. This interface plugin enables the framework to receive target displacements and send feedback responses to a FEA software. The plugin will be referred as LNTCP in the subsequent parts of this section. LNTCP is a collection of LabVIEW virtual instruments (VIs) that ensure proper transaction of responses, back and forth, between the simulation coordinator VI and OpenFresco. The Experimental LabVIEW control class of OpenFresco sends a TCP/IP data packet to LNTCP and receives a feedback force. The communication starts with a TCP listen VI defined in the Pre-run state. Once the TCP/IP connection is established, the TCP read VI receives a command displacement while a TCP write VI sends intermediate replies and eventually a feedback force. Data packets have a variable-length tab-delimited ASCII format on a single line. Newline is considered as a message delimiter.

Transaction ID is included in every message, so that the client side can be asynchronous and multithreaded. The LabVIEW control class of OpenFresco has a propose-query-execute mode of operation. The sequence of commands executed throughout a hybrid test are detailed in Figure 59 and its implementation in LabVIEW is shown in Figure 60.

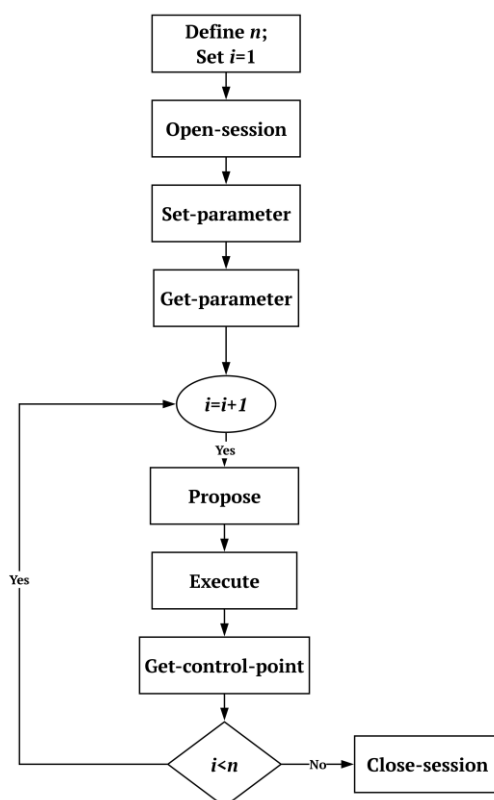


Figure 59: LNTCP dataflow

Open-session message is received when a TCP/IP connection is established. The next two-steps allow user to define and get parameters necessary for the subsequent transaction process. These steps are optional, and they can be skipped by sending 'OK' string back to OpenFresco. In each time-step of the

integration loop, three mandatory steps, propose, execute and get-control-point, are executed. The message syntax of each step is important in decoding data packets sent from OpenFresco and sending feedback signals to it.

Open-session: It can be used to optionally initialize hardware or do any other system-specific work as required. The LabVIEW LNTCP application duly ignores it by sending 'OK' string.

Receive syntax	Return syntax
<i>Open-session TransactionID Parameter Parameter</i>	OK

Set-parameter: This step mirrors the get-parameter message. LabVIEW ignores it by sending 'OK' string as well.

Receive syntax	Return syntax
<i>Set-parameter TransactionID ParameterName Parameter</i>	OK

Get-parameter: This is mainly used for passing parameters to be used for simulation. This command was not used in the current implementation.

Receive syntax	Return syntax
<i>Get-parameter TransactionID ParameterName</i>	OK 0 ParameterName Parameter

Propose: It can handle up to 12 parameters depending on the control point. In this research, a two-point control is developed that has displacement as its only control parameter. Right after this command is received, a separate loop in the LNTCP matches the command with an actuator meta data that was initially saved into the RT host. The actuator meta data consists of an actuator name, control point, geometry, parameter type, limit values and so on forth. If received data matches the actuator data, the proposed values are accepted, other it is rejected. *GeometryType* signify the actuator's axis of loading which is a single character, x, y, or z. *ParameterType* mirrors the control parameter i.e., displacement, force, rotation, or moment. *Parameter* is a simple scalar floating-point number that represents the magnitude of a parameter that is controlled by the loading system. No message is returned in response to propose command.

Receive syntax
<i>Propose TransactionID {ControlPoint GeometryType ParameterType Parameter}¹ {ControlPoint GeometryType ParameterType Parameter}²...</i>
e.g. <i>Propose OPFTransactionIDTimeStamp MDL-00-01 x displacement 0.1</i>

^{1,2} and so on for the number of control parameters sent from OpenFresco

Get-control-point: Get-control point can also support up to 12 parameters as well. It mirrors the propose command in order to return measured responses back to OpenFresco. LNTCP is designed to handle a two-point control with a measured displacement as its first parameter and a corresponding measured restoring force as its second parameter.

Receive syntax	Return syntax
<i>Get-control-point TransactionID ControlPoint</i>	OK 0 ParameterName Parameter
E.g. <i>OK 0 OPFTransactionIDTimeStamp x displacement 0.01 x force -0.113</i>	

Execute: This command message simply executes a previously accepted proposal. The same TransactionID that was used in the proposal and get-control point must be adopted. During the return phase of each of the commands, LNTCP uses a Semaphore VI that allows a given command to be only executed while blocking any other TCP threads to OpenFresco. The TCP read VI that is responsible for this operation is set to run a higher level of priority.

Close-session: Close-session command is executed at the end of a hybrid test. It mirrors the Open-session command. The command does not perform any task on the current protocol.

Receive syntax	Return syntax
<i>Close-session TransactionID Parameter Parameter</i>	<i>Until next time!</i>

Command-reader, limit-checking loop and replier loops make-up the LNTCP. The replier loop, as its name indicates, only displays received and returned TCP data packets. The command-reader loop reads TCP data packets, sent from OpenFresco, byte by byte. This is mainly since TCP data is an anonymous sequence of bytes (Iniewski et al., 2008, Forouzan A., 2010). Thus, data is captured in this manner until the EOL (end of a line) character is encountered, marking the end of a message. The ASCII message is then parsed and enqueued into a *Command queue*.

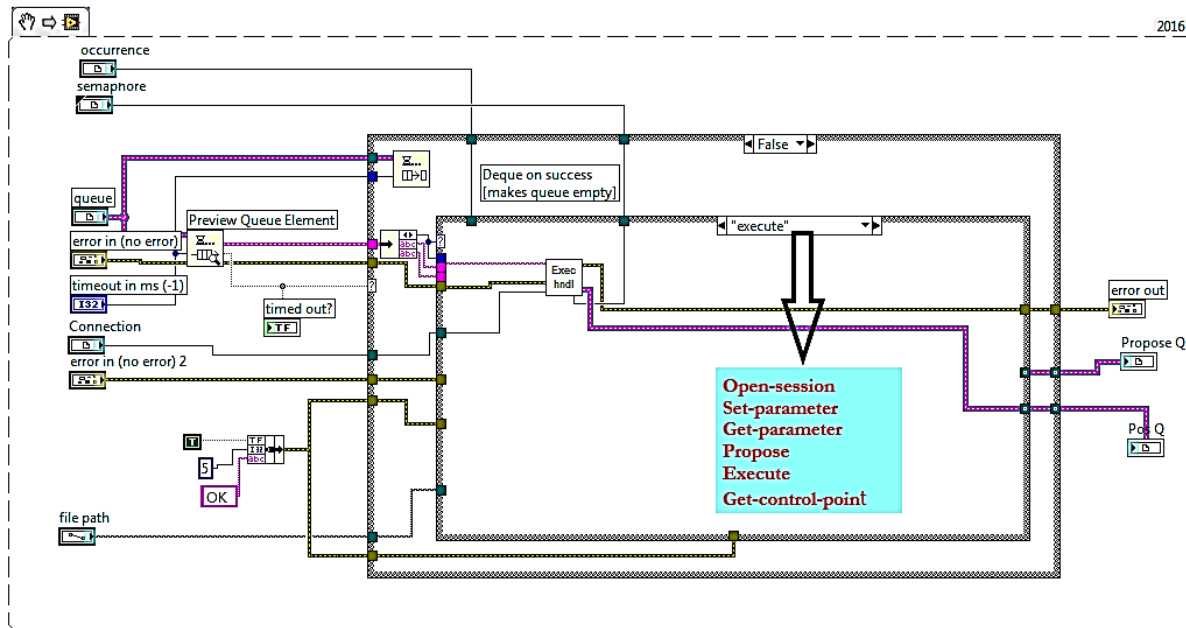


Figure 60: Implementation of LabVIEW plugin for interfacing OpenFresco

The limit-checking and replier loops are designed in the form of a case-structure with each case representing a unique step in LNTCP operation. The data enqueued into the command-reader loop is retrieved and response is sent to OpenFresco. As discussed earlier, in each step, a LabVIEW semaphore is obtained and released sequentially to avoid any thread collision. When the program prompts to execute step, the magnitude of the control parameter is enqueued into a *Position queue*. The *Command queue* at this stage is emptied (or dequeued) and is ready to receive the next time-step command. In parallel, *PreCor queue*, after receiving the target value from *Position queue* drives the correction process of the control loop.

2.1.6 Command generation and tracking

The timely interchange of target displacement and feedback force do not occur instantly since a significant amount of time is spent during the TCP/IP communication in a hybrid test. This phenomenon would force an actuator to move in a ramp-and-hold manner. Force relaxation is therefore likely to occur during the hold phase that could jeopardize the accuracy of simulation. This effect is potentially strong when strain-dependent physical substructures are subjected to fast hybrid tests. To improve this effect, continuous movement of an actuator is essential during hybrid testing that is commonly implemented by extrapolation-and-interpolation algorithms.

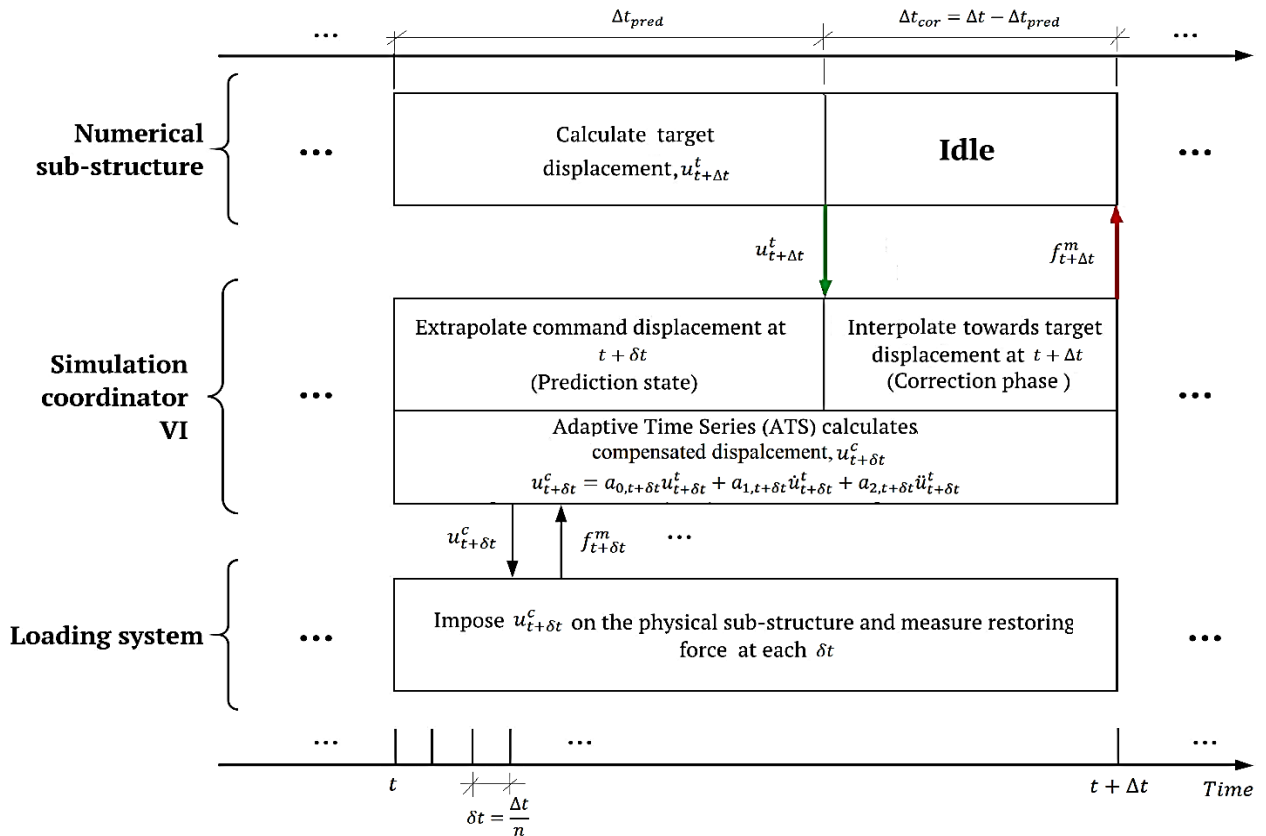


Figure 61: Schematic representation of data flow in hybrid simulation

Initially, extrapolated commands are applied by the actuator while the FEA software is solving the next time-step target displacement. When the target displacement is available at the simulation coordinator VI, the algorithm interpolates towards it. The default value is forty percent (40%) of the time-step for extrapolation while the remaining 60% of the time-step is assigned to interpolation. However, the duration for extrapolation can be adjusted from the control panel. In general, analysis of a structure with large number of elements and/or inelastic level of structural analysis takes longer time implying the need for a longer extrapolation period. However, this additional time might be way too small compared to the latency of TCP/IP. For moderate sized frames, the default setting is a reasonable value. A schematic diagram shown in Figure 61 gives a complete picture of the data flow while operating the middleware-based section of the software framework.

Third-order Lagrange polynomials are implemented in extrapolating and interpolating commands following reports from Nakashima & Masaoka (1999). Schellenberg et al. (2009) also adopted 3rd order polynomials during an extrapolation/interpolation process that was based on 80% of extrapolation. Three different algorithms of extrapolation/interpolation are implemented during the development of the software framework. The first prediction-correction method is only based on displacements. This algorithm is characterized by a large discontinuity, step-like jump, when the algorithm switches from the last predicted displacement to the first interpolated displacement leading to a high velocity demand.

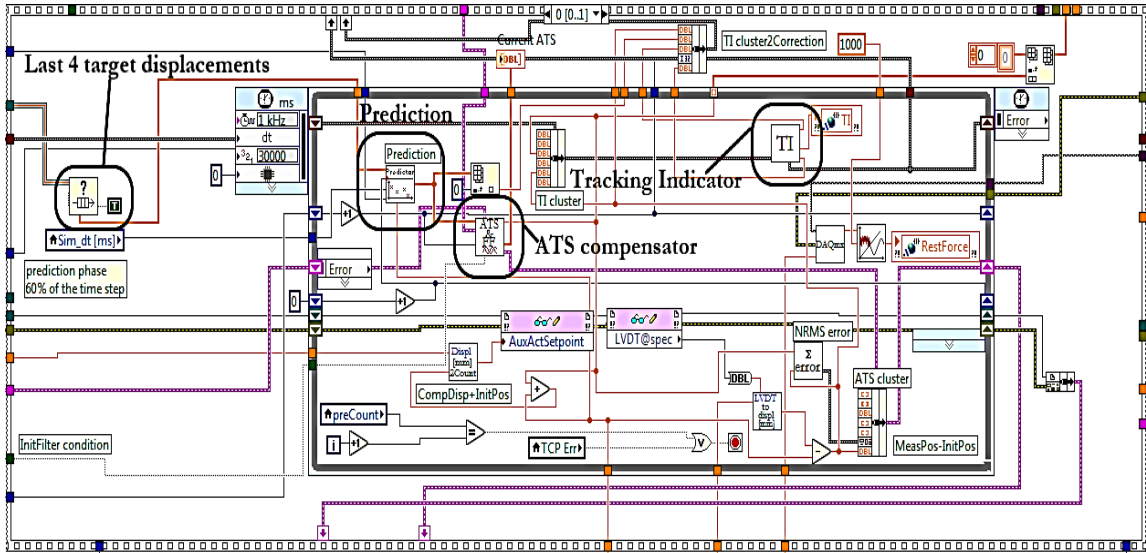


Figure 62: Prediction loop for command generation, compensation and error tracking

The second algorithm however improves the smoothness of displacement path that commands an actuator. This is accomplished by using the last predicted displacement in the interpolation process. Nevertheless, it is not guaranteed to yield a continuous displacement path as it depends on how the controller is tuned. On the other hand, the third method seeks to improve velocity accuracy using velocities in addition to displacements. However, many direct integration methods have less accurate trial velocities that can potentially impair the accuracy predictor-corrector algorithms. Thus, velocities were calculated by numerical differentiation using 2nd order Lagrange polynomials.

In the extrapolation process of the first algorithm, the last four target displacements (i.e., $n=3$) that are sent from the numerical model are used for extrapolating the next time-step displacement.

$$u_{x,p} = \sum_{t=0}^{k=3} u_{t-k} P_{n=3,k}(x), \quad x \in [0, \frac{\Delta t_{pred}}{\Delta t}] \quad (9)$$

Where $P_{n=3,k}$ is a third-order Lagrange polynomial. Similarly, the correction phase is calculated by:

$$u_{x,c} = \sum_{t=0}^{k=3} u_{t-k} C_{n=3,k}(x), \quad x \in [0, 1] \quad (10)$$

Where $C_{n=3,k}$ is a third-order Lagrange polynomial.

Prediction process in the last-predicted displacement approach is like the first method. The correction phase, in the other hand, uses last-predicted displacement, i.e., $[u_{t-2}, u_{t-1}, u_{t-0}, u_{last,p}]$ displacement vector. Where $u_{last,p}$ is predicted at $x = \frac{\Delta t_{pred}}{\Delta t}$. Prediction-correction algorithm using velocities is accomplished using third order Hermite polynomials. Schellenberg et al. (2009) studied continuity and accuracy of several prediction-correction approaches including a method that uses acceleration.

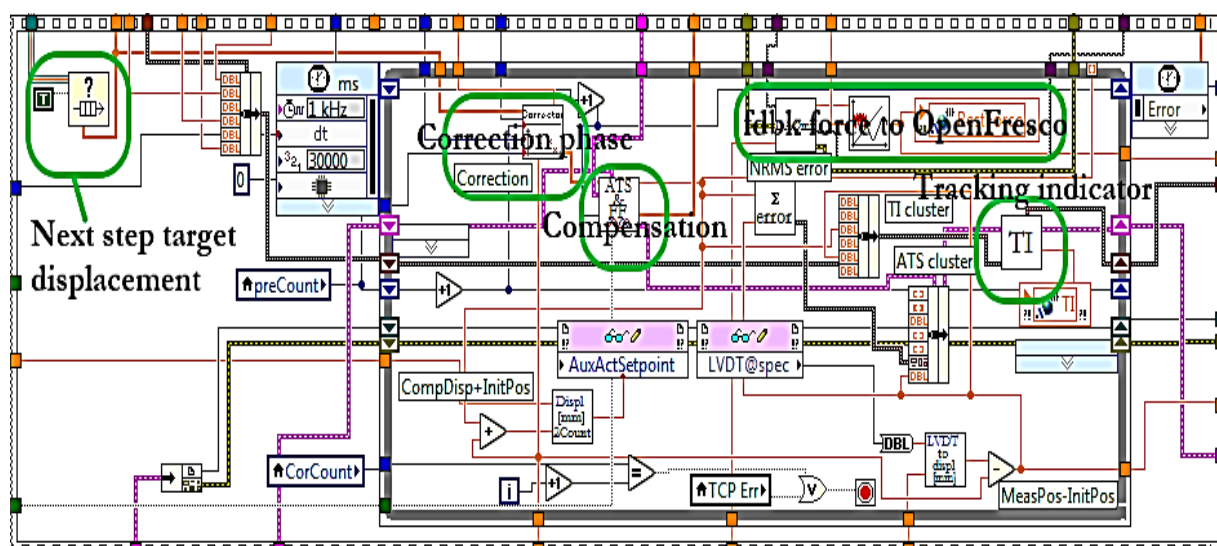


Figure 63: Correction loop for command generation, compensation and error tracking

2.1.7 Command compensation

Phase and amplitude errors of a command displacement have evolutionary nature during a hybrid test; and offline methods fail to capture these errors which are highly dependent on magnitude of the displacement command, excitation frequency and the ever-changing tangent stiffness of the physical substructure. Hence, an adaptive method whereby compensation parameters are evolutionary is the core idea behind ATS technique. Besides, compensation parameters can be directly correlated to experimental errors unlike many other compensation schemes (Chae et al., 2013). This time-domain adaptive compensator is based on second order Taylor expansion in conjunction with least-square error optimization. The algorithm adopted in the current research is slightly different from the original ATS algorithm developed by Chae et al. (2013). The original ATS uses Backward difference method to compute the target velocity and acceleration. In the current research, the derivatives are computed using third-order Lagrange polynomials.

Like the original ATS, initialization of compensator parameters (a_0 , a_1 , a_2) is carried out by estimating second-order compensator parameters in an offline test, using a BLWN input, prior to hybrid simulation. ATS is triggered 1 s after initiating hybrid test thus allowing the controller to build a compensation matrix with 1024 data samples since the clock-speed of command generation is set to 1 kHz. Besides, potential instability can occur if compensation matrix is ill-conditioned. This may happen when starting or ending a hybrid test since measured displacement has a low signal-noise ratio and may result in abrupt change of ATS parameters that may eventually lead to unstable simulation. To solve this issue, Chae et al. (2013) suggested to deactivate updating the compensation parameters if a peak measured displacement, on a 1 s window, is below a threshold displacement. Its implementation using LabVIEW programming language is presented in Figure 65.

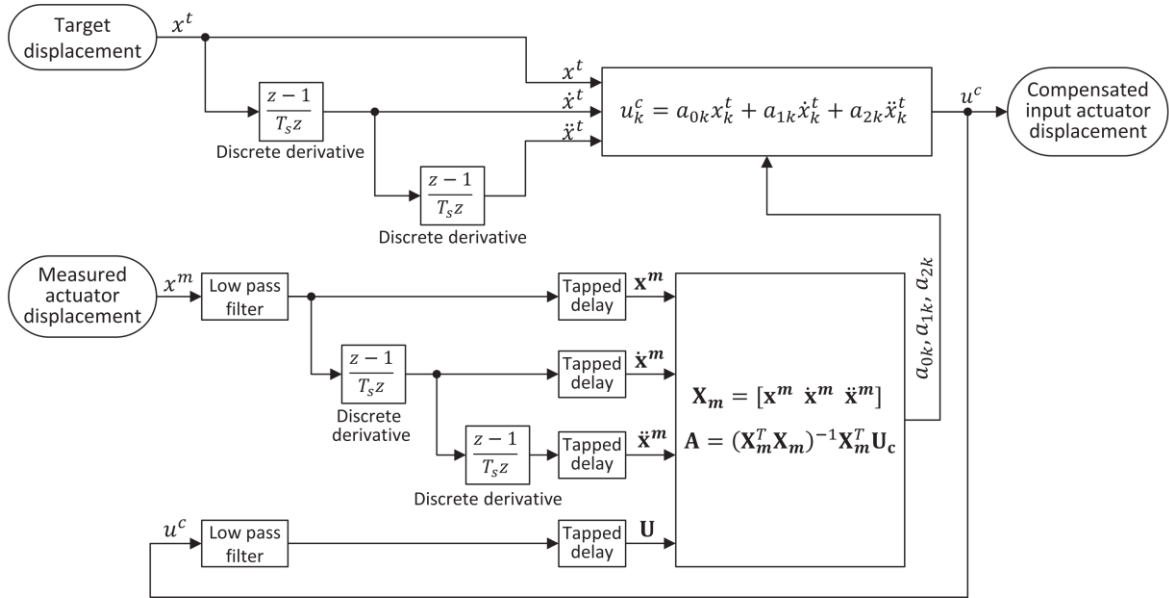


Figure 64: Schematic of adaptive time series (ATS) (after Chae et al., 2013)

However, Dong (2015), suggested that a threshold value based on RMS value of the measured displacement has better performance. He used a threshold value of 1 mm in triggering the compensator. In the current implementation, the initial value of the compensation parameters is kept current if RMS value computed on a 1 s window is smaller than 1 mm. This parameter is designed to be adjustable since different transducers has different noise-levels and threshold value as large as 1 mm may not be necessary.

To achieve stable compensation, range of compensation parameters is defined a priori. The range for a_0 is derived from the maximum expected gain error. Consistently with Chae et al. (2013), $\pm 30\%$ of the initial value was adopted in this work. The range for a_1 is calculated using the maximum actuator time delay identified using the estimated initial parameters. The maximum actuator delay, τ_{max} , can be computed directly from a_1/a_0 . The range for a_1 are therefore set assuming $\pm 100\%$ margins on the initial value. Similarly, the maximum value of a_2 is computed from $\tau_{max}^2/2$ thus allowing us to set its range as $[0, \tau_{max}^2/2]$. For the case-study presented in the framework validation, a remarkable overall time delay less than 2 ms was achieved after tuning the controller gains. The tuning however resulted in a significant overshoot which can be compensated using ATS.

The rate of change of compensation parameters are also restricted depending on practical values that are supported by servo-hydraulic actuators. The values proposed by Chae et al. (2013) are also adopted in this study. Kolay (2016) found that ATS tends to amplify high frequency component of a response if a_1 and a_2 are set to large values. Hence, trial runs for tuning upper limits of compensation parameters are handy prior to conducting a hybrid test. Additionally, putting too much restriction in the upper limits of ATS parameters may result in poor compensation in the frequency range of interest that can eventually compromise the accuracy of a hybrid test.

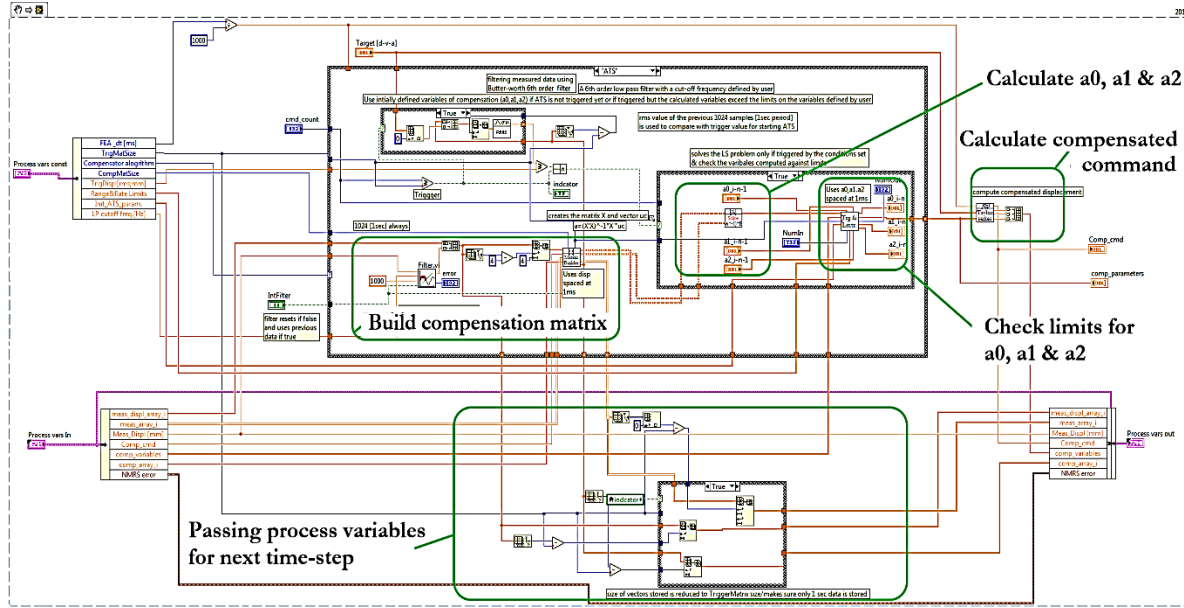


Figure 65: Implementation of ATS in LabVIEW simulation coordinator VI

The backward difference (BD) method for calculating derivatives has a first order error to the exact solution. At 1 kHz clock-speed of the controller, δt , the target velocity and acceleration are calculated as:

$$\dot{x}_t = \frac{(x_t - x_{t-N\delta t})}{\Delta t} ; \ddot{x}_t = \frac{(x_t - 2x_{t-N\delta t} + x_{t-2N\delta t})}{(\Delta t)^2} \quad (11)$$

Where N and δt are the number of sub-steps at each time-step, Δt , and sub-step size respectively. Replacing the BD formula in the second-order Taylor series and transforming the entire equation into a discrete z-transform, the discrete transfer function, G_{ATS} , from target displacement, x_t , to output compensated displacement, x_c , can be expressed by:

$$G_{ATS}(z) = \frac{x_c(z)}{x_t(z)} = \frac{1}{\Delta t^2 z^{2N}} \{q_2 z^{2N} + q_1 z^N + q_0\} \quad (12)$$

$$\text{Where: } q_2 = a_0 \Delta t^2 + a_1 \Delta t + a_2$$

$$q_1 = -a_1 \Delta t - 2a_2$$

$$q_0 = a_2$$

a_0 , a_1 and a_2 are the compensation parameters

Considering third-order LaGrange polynomials for computing the first and second-order derivatives of displacement, the discrete transfer function, G_{ATS} , from target displacement, x_t , to output compensated displacement, x_c , can be expressed in a similar way as:

$$G_{ATS}(z) = \frac{x_c(z)}{x_t(z)} = \frac{1}{\Delta t^2 z^{3N}} \{q_3 z^{3N} + q_2^* z^{2N} + q_1^* z^N + q_0^*\} \quad (13)$$

$$\text{Where: } q_3 = a_0 \Delta t^2 + \frac{11}{6} a_1 \Delta t + 2a_2$$

$$q_2^* = -\frac{18}{6} a_1 \Delta t - 5a_2$$

$$q_1^* = +\frac{9}{6} a_1 \Delta t + 4a_2$$

$$q_0^* = -\frac{2}{6} a_1 \Delta t - a_2$$

Since target displacement is generally less noisy, higher frequency effects are less detrimental. Thus, the choice for computing derivatives of the target displacement can be assumed to be solely dependent on accuracy criteria. To this end, accuracy of a compensator that uses third-order Lagrange polynomials for calculating derivatives is compared to the original implementation by Chae et al. (2013). Compensation parameters are varied to reflect gain and delay errors that are calibrated to actual experimental tests. a_1 and a_2 are varied to yield a time delay in the range of [20, 40] ms. The simulation assumes that delay is constant throughout a hybrid test. This assumption is reasonable in order to compare the two schemes for computing the derivatives. As pointed out earlier, a_0 is the result of a gain error. Thus, cases without gain error and $\pm 10\%$ gain error are considered in the presence of a time delay between command and measured response.

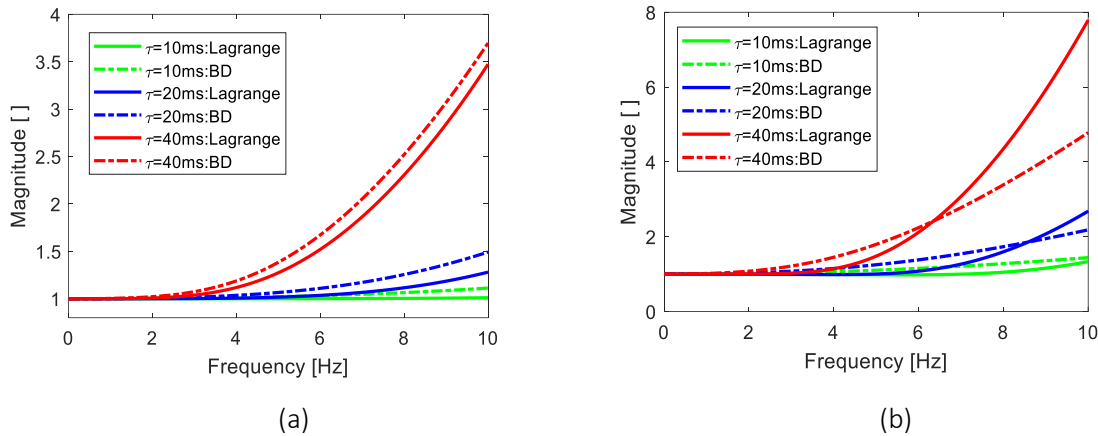


Figure 66: Magnitude of G_{ATS} without gain error (a) time-step=4 ms (b) time-step=20 ms

At small time-step size, the magnitude of G_{ATS} is close to unity for actuator delays as small as 10 ms. For actuator time delays greater than 20 ms, the compensator overshoots as frequency increases. For example, at 40 ms of actuator’s time delay, target displacements of a test structure operating at 10 Hz can be amplified by a factor as large as 3.5. ATS based on Lagrange derivatives remain superior to ATS based on BD method especially when the time-step size is small.

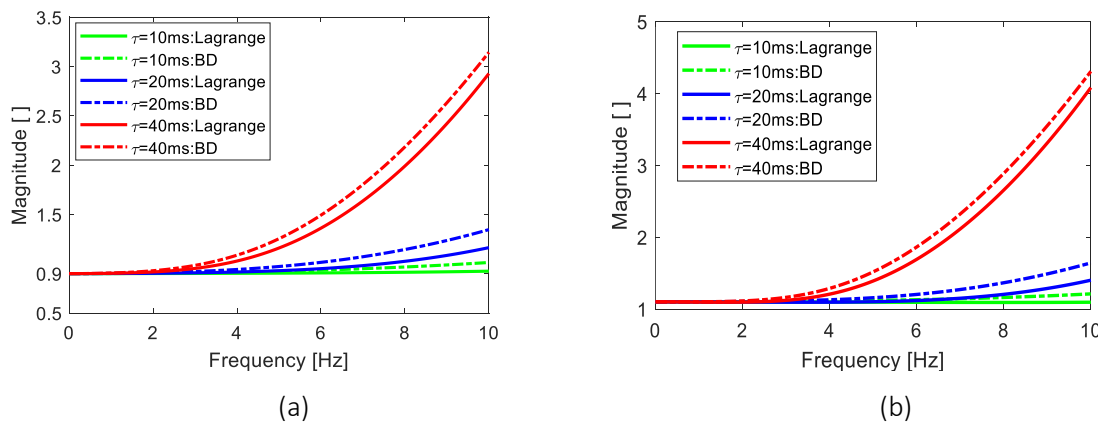


Figure 67: Magnitude of G_{ATS} under (a) 10% overshoot (b) 10% undershoot

With increasing time-step size, the amplitude of overshoot increases, as shown in Figure 66(b). Besides, the BD approach starts to gain better performance at large frequencies favoring structures whose responses are governed by frequencies above 6 Hz. The performance of ATS based on Lagrange derivatives seem to deteriorate with increasing time delay.

Figure 67 reflect the characteristics of the compensator in the presence of undershoot and undershoot gain errors. Simulation results confirms the favourable property of an overshoot gain error during a hybrid test. Undershoot error can be also be interpreted as a time delay error, thus directly adding to the detrimental effect of a time delay error. The theoretical relationship, $a_2 = (a_1)^2/2$, was considered in deriving the magnitude of G_{ATS} . However, the parameters of the compensator are estimated by minimizing the least square error between the compensated and measured displacements. Hence, the compensation parameters may not be necessarily related according to the theoretical formula. To this end, for a_2 less then $(a_1)^2/2$, the compensator has comparatively smaller overshoot error especially for larger values of time-delay. This entails the need for careful monitoring of the parameters of the compensator while executing a hybrid test.

2.1.8 Tracking Indicator

Tracking indicator (TI) calculates the area enclosed in the hysteresis of a synchronized subspace plot (SSP). SSP is the plot with a command displacement in the vertical axis and a measured displacement in the horizontal axis (Mercan and Ricles 2009). The method uses complementary and enclosed areas to compute the area enclosed in the SSP (see equations 14 to 16).

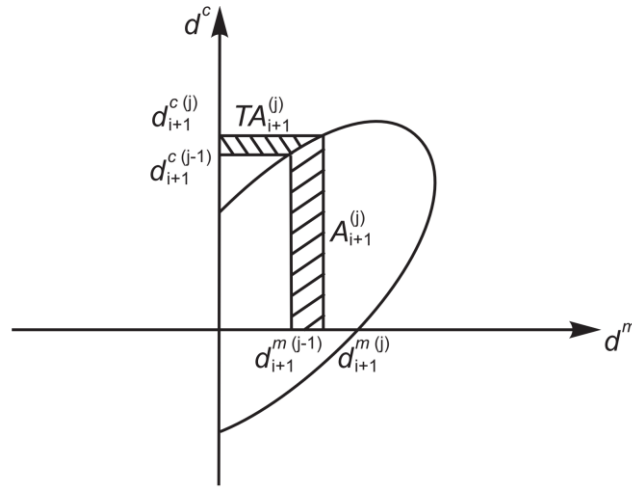


Figure 68: Definition of Tracking indicator (TI) (after Mercan and Ricles, 2009)

TI can be monitored online from the GUI of the software to help in identifying errors during a hybrid test. It has a refresh rate of 0.1 s. Positive values of TI indicate a leading feedback while negative indicate a lagging feedback. Despite the coupled effect of gain and delay errors, the SSP plot together with TI help to identify the nature of the errors. The Phase and Amplitude Error Indicator (PAEI) method that was proposed by Hessabi and Mercan (2007) can uncouple the two errors using a least square solution of the ellipse equation of the SSP plot. The latter method was not implemented in the current framework since it needs a significant share of computational resource in operating it online. A comprehensive list of assessment measures is discussed by Christenson et al. (2014).

$$TI_{i+1}^j = 0.5(A_{i+1}^j - TA_{i+1}^j) \quad (14)$$

The enclosed, A_{i+1}^j , and complementary areas, TA_{i+1}^j , are calculated as:

$$A_{i+1}^j = A_{i+1}^{j-1} + dA_{i+1}^j = A_{i+1}^{j-1} + 0.5(d_{i+1}^{c(j)} + d_{i+1}^{c(j-1)})(d_{i+1}^{m(j)} - d_{i+1}^{m(j-1)}) \quad (15)$$

$$TA_{i+1}^j = TA_{i+1}^{j-1} + dTA_{i+1}^j = TA_{i+1}^{j-1} + 0.5(d_{i+1}^{c(j-1)} - d_{i+1}^{c(j)})(d_{i+1}^{m(j)} + d_{i+1}^{m(j-1)}) \quad (16)$$

Clockwise direction of winding of the SSP plot indicates a phase-lead while anti-clockwise winding indicates a phase-lag. Moreover, plot inclination below 45° signifies an undershoot error, while plot inclination above 45° signifies an overshoot error.

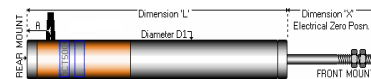
2.2 Data acquisition and transducers

Data acquisition block of the framework records data from linear variable displacement transducers (LVDT), load cell and accelerometers. A 68-pin shielded connector block, SCB-68, connects the FPGA module to signal conditioners. RDP600 signal conditioner rack equipped with RDP 611 is responsible for conditioning analogue signals from LVDT and load cell transducers. ENDEVCO accelerometers are also conditioned using an analogue conditioner. NI data acquisition (NI-DAQ) is also integrated into the simulation coordinator VI. Acquired data is buffered, 100 measurements from each transducer, in the DAQ loop before being transferred to the Host PC (see Figure 71). This improved the performance of the simulation coordinator VI during the prediction-correction state. The speed of data acquisition can be adjusted from the front panel of the simulation coordinator. DAQ rates faster than 1 kHz clock speed may not be realized due to limitations in the NI controller.

NI DAQ board and accessories



LVDT



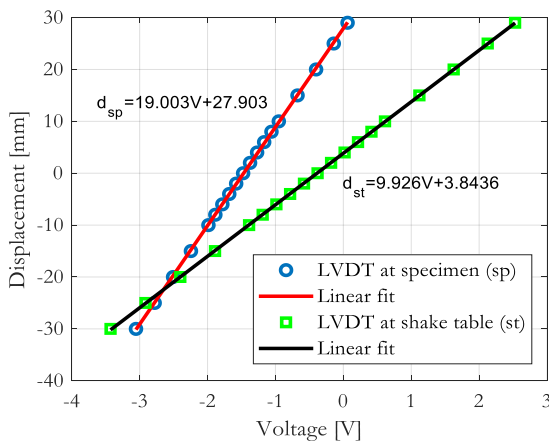
ENDEVCO accelerometer

PCB accelerometer

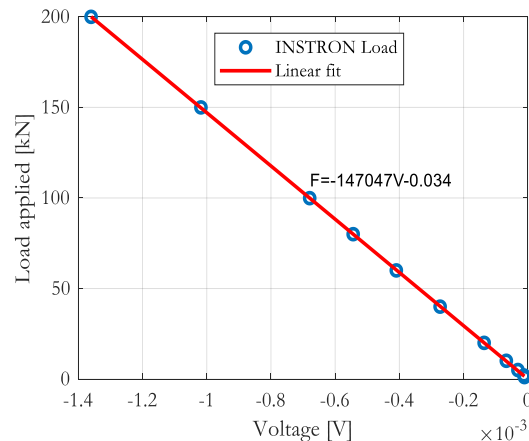


INSTRON load cell

Figure 69: NI DAQ modules and transducers for hybrid simulation



(a)



(b)

Figure 70: Transducer calibration: (a) LVDTs; (b) INSTRON load cell

Prior to an experimental testing, sensors are all calibrated whereby scale factors of an engineering unit to electrical command (voltage in the current implementation) are calculated.

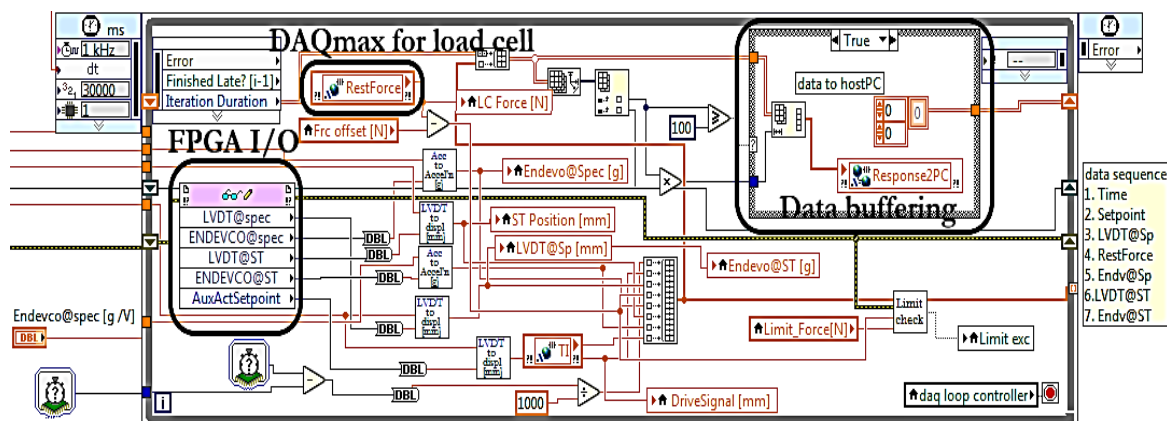


Figure 71: Implementation of data acquisition loop in simulation coordinator VI

2.3 HDS framework validation

2.3.1 Case-study

Three two-dimensional steel frames are considered for validating the software framework. They are moment resisting steel frames with rigid floors. The first two categories have one storey and two bays. The left external column forms the experimental substructure while the remaining part is modelled numerically in OpenSees Finite-element software. All columns of frame-1 (see Figure 72) are 1.8 m high with a fixed end connection at the base. They are hinged at the connection to the roof beams. The hinge boundary condition is purposely designed to allow a one-parameter actuator control during the hybrid test. Frame-2 has unequal height of columns with the shorter column in the middle, 1 m in height, and two 1.8 m high external columns. In the latter, overall system nonlinearity can be achieved without introducing any permanent damage in the experimental substructure. Hence, the second category of steel frame aims to validate capability of the software framework under nonlinear simulation. A bay width equal to 3.6 m is maintained in all frames.

The experimental column does not experience any plastic damage in Frame-2 and it can be considered as a virgin specimen for further hybrid tests. Frame-3 is a one-bay two-storey steel frame that was designed to examine the potential of the framework during hybrid test of a structure with comparatively larger number of DOFs. The left-hand column (marked by red dashed line) in the ground floor level is tested physically while the rest of the frame is modelled numerically. Ground floor columns are hinged at the top, as shown in Figure 72, for the same reason discussed above. All columns are constructed from S355 grade HEB 100 steel profiles while beam elements are made from S355 grade IPE 240 steel profiles. All beams are designed to remain linear during the simulation.

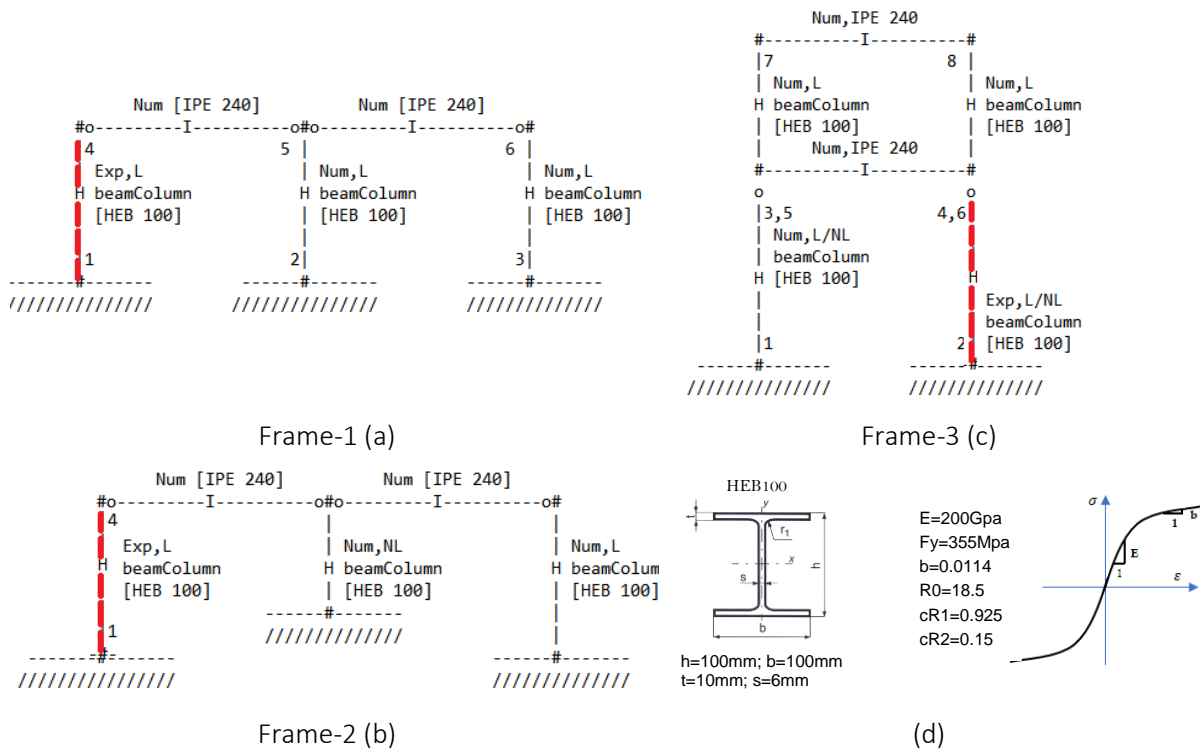


Figure 72: Definition of case-study: (a) steel frame-1; (b) steel frame-2; (c) two-storey one-bay steel frame; (d) steel column properties

2.3.2 Test setup

The uniaxial shake table at LNEC was used for conducting the validation hybrid tests on the steel frames. The experimental column is welded to a steel base at the bottom and connected to a loading strut at the top as shown in Figure 73. The loading strut is connected to a load cell at its rear end and measures the column’s restoring force. The strut is rigidly connected to the shake table platen through a space truss. The shake table base frame is also rigidly secured to a strong floor. The experimental column (test specimen) is welded to a steel base which is attached to the strong floor through bolt and nut system.

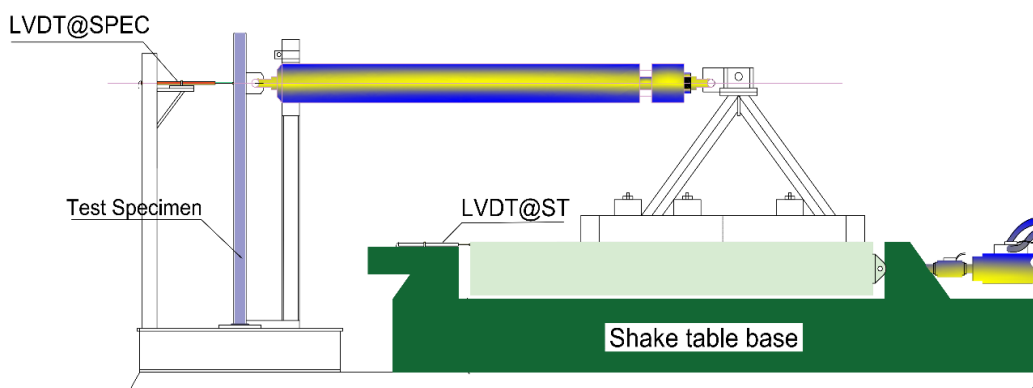


Figure 73: Test setup for hybrid simulation

The command to the actuator’s servo-valve drives the shake table platen which in turn drives the experimental column. To achieve the same target displacement, received from OpenFresco, at the strut-level of the test specimen, feedback to the controller is returned from the ‘LDVT@SPEC’. The sudden drop depicted in Figure 74 (a) shows presence of gap at joints. A total of 0.1 mm gap is identified

in the test setup. The joints connecting the steel mast and space truss, the space truss to plate, and the steel strut to the experimental column are all tightened after careful inspection.

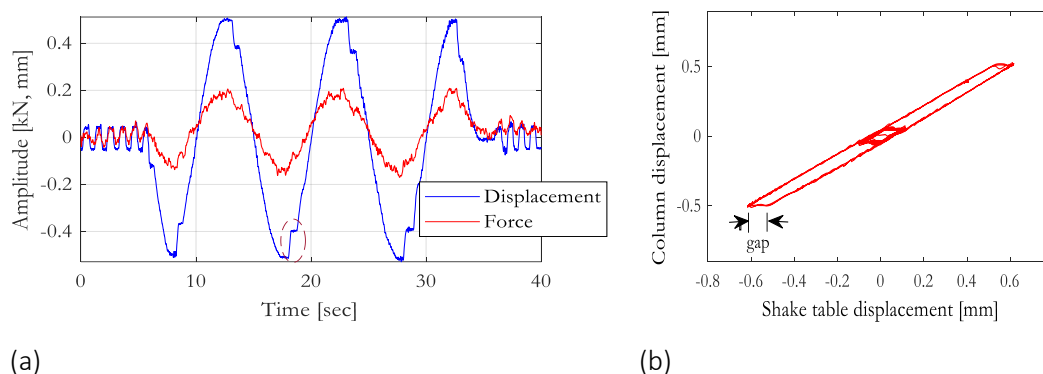


Figure 74: (a) Joint gap identification in test setup; (b) Sub-space synchronization plot (SSP)

OpenFresco middleware returns initial stiffness of the experimental column to OpenSees. Hence, accurate estimation of the initial stiffness of the experimental structure is very essential in producing better fidelity results. Thus, the modal frequencies of the steel column were firstly characterized using a hammer test.



Figure 75: Column hammer test

The steel column was divided into 6 equal sections, with 30 cm spacing, from the base to the point of the connection between the column and the strut. This leaves a free height of 37.5 cm above the connection point. Six PCB accelerometers (0.5 g maximum capacity) were attached on one of the flanges of the HEB 100 profile. Hammer impacts were then conducted on the second flange in a roving manner at the level of the accelerometers. This resulted in six hammer tests, H1-H6. The hammer has

a rigid head that is connected to a PCB accelerometer that has 50 g acceleration capacity. Each test has six impacts that are spaced by a 10 s idle time. The window size was selected after experimenting the damp-out time of the acceleration measurements. This avoids overlapping of acceleration measurements from neighboring impacts. Data was acquired at 1 kHz frequency during the test.

FRFs of all impact tests were computed after filtering measured accelerations with a low-pass Butterworth filter at 50 Hz. The modal frequencies and modal damping coefficients were determined by Enhanced Frequency domain decomposition (EFDD) and Canonical Variate Analysis (CVA) methods of operational modal analysis (OMA). Nevertheless, experimental modal analysis (EMA) is more pragmatic in this case since external force is applied to the column. Thus, EMA estimates were also computed by superposing FRFs of all measurement points (M1-M6) and all test setups (H1-H6). The OMA estimates were also in good agreement with EMA estimates. The fundamental frequency was estimated to be 18.24 Hz (refer to Figure 76). This implies a non-rigid connection between the steel-base and strong floor since the theoretical frequency of the column is 25.32 Hz. Therefore, the initial rigid-base model of the cantilever column is updated as a pin-ended connection with moment capacity defined by a rotational spring, K_{θ} .

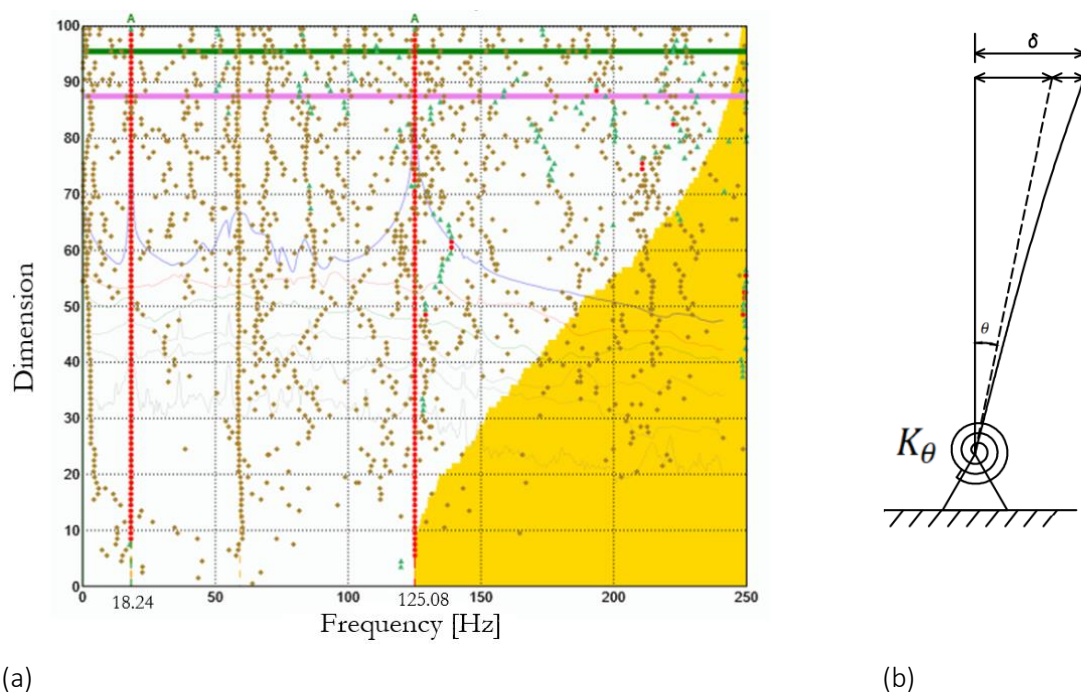


Figure 76: (a) Operational modal analysis using CVA; (b) Modelling experimental column

The 1st and 2nd modal frequencies of the updated model of the column are matched with the experimentally identified estimates by modelling the experimental column as pin-ended and a rotational spring K_{θ} equal to 1942 kNm/rad. Results of column identification and the model updating are presented in Table 13. Stiffness matrix of the updated model of the was then computed following the principles of semi-rigid frame modelling. The stiffness matrix was then used in defining the BeamColumn Experimental element in OpenFresco.

$$K = \begin{bmatrix} 288090.00 & 0 & 0 \\ 0 & 282.075 & -617.33 \\ 0 & -617.33 & 1322.45 \end{bmatrix} \text{ kN, m}$$

Table 13: Modal identification of experimental substructure

Mode	Undamped Frequency [Hz]			Experimental Damping [%]
	Experimental [EMA/OMA]	Numerical [SAP2000]	Updated Numerical [SAP2000]	
1	18.24	25.08	18.25	0.27
2	45.21	-	-	0.69
3	54.32	-	-	0.56
4	58.66	-	-	0.52
5	75.14	-	-	0.4
6	83.50	-	-	0.36
7	125.08	148.76	124.87	0.18

The rotational spring is modelled using the zero-length element class of OpenSees and the rotational restraint along the major axes of the inelastic beamColumn element is released. All columns were modelled using Steel02 constitutive model of OpenSees. The strain hardening ratio of the constitutive model was computed from principles of continuous strength method (CSM) developed by Yun and Gardner (2017). CSM is a strain-based approach that predicts section capacities more accurately compared to international design guidelines. It uses a quad-linear curve to define the stress-strain backbone of steel. The strain hardening ratio, b , is estimated from:

$$b = \frac{f_u - f_y}{C_2 \varepsilon_u - \varepsilon_{sh}} \frac{E_{int}}{E_{int}} \quad (17)$$

The ultimate strain, ε_u ; strain-hardening strain, ε_{sh} , and the slope term, C_2 , are computed by:

$$\begin{aligned} \varepsilon_u &= 0.6 \left(1 - \frac{f_y}{f_u} \right) \quad \left[\frac{f_y}{f_u} \leq 0.9 \right] \\ C_2 &= \frac{\varepsilon_{sh} + 0.4(\varepsilon_u - \varepsilon_{sh})}{\varepsilon_u} \\ \varepsilon_{sh} &= 0.1 \frac{f_y}{f_u} - 0.055 \quad \left[0.65 < \frac{f_y}{f_u} \leq 0.85 \right] \end{aligned} \quad (18)$$

Where E_{int} is the initial steel modulus, taken to be 210 GPa.

The initial parameters of ATS also need to be estimated via an experimental test using second-order estimation. Command displacement is prepared by summing up a White Gaussian Noise (WGN) at 10 mm amplitude, in the frequency range 0-1 Hz, and a 2 mm WGN in the frequency range 0-20 Hz. This compound WGN input displacement was applied to the shake table in order to estimate the gain error and time delay of the system. The command signal was sampled at 50 Hz frequency.

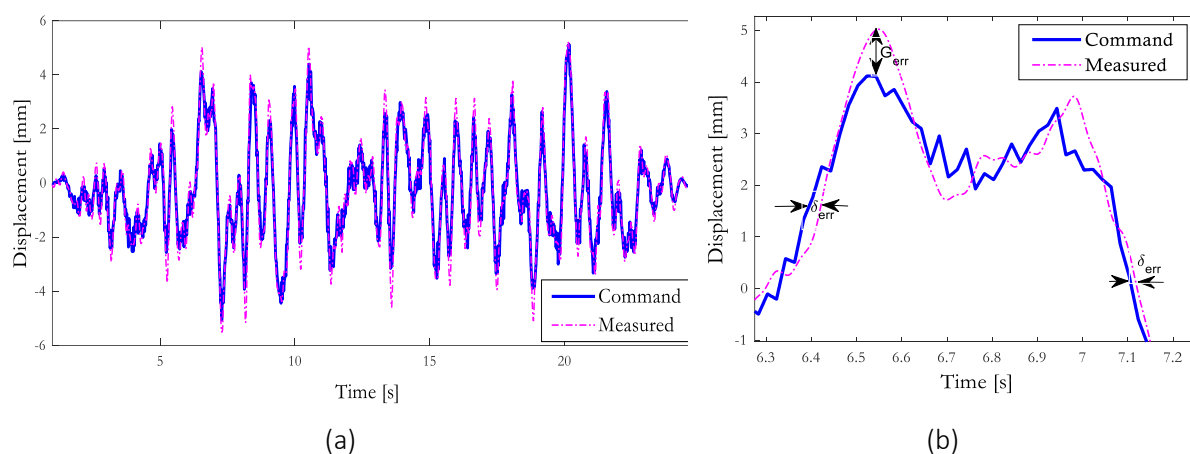


Figure 77: (a) Command versus measured displacement of ST1D; (b) a closer view on time delay, δ_{err} , and gain error, G_{err}

The measured acceleration was directly used for estimation after its treatment whereas the velocity response is synthesized from the measured displacement and acceleration. A cross-over frequency of 4 Hz was adopted during the velocity synthesis. Measured displacement is cropped at the start and at the end to so that the estimation matrix will not be ill-conditioned. To have a reliable estimation of the variables, the command and measured displacements were filtered by a 20 Hz low-pass Fourier filter. Parameters are estimated to be $a_0=0.9066$, $a_1=0.0015$ s and $a_2=9.95e-5$ s². These parameters can be interpreted as 1.65 ms time delay and 10.3% overshoot error. The ATS identification test was conducted at $k_p = 3.5$ and $k_i = 0.001$. Changing control gains can significantly alter compensation parameters. PID gains were therefore set to fixed values throughout the testing campaign.

2.3.3 Rehearsal test for hybrid simulation

In the initial step, proper functioning of all the software components are tested in order to detect bugs in the software. Besides, adequacy of the control/compensator algorithm is assessed. Failure to do so, can damage a test specimen prematurely. Thus, a simulated hybrid test, also termed as *open-loop* hybrid test, is conducted by sending back simulated restoring force into the FEA software instead of sending the measured restoring force. The loading system can either be kept inactive by disconnecting the drive signal to the actuator or the drive signal is scaled and applied to the test specimen. Software bugs and communication issues can be identified in the former open-loop test. The latter is conducted at low excitation level and the performance of control and compensation algorithms can be evaluated by comparing the target and measured displacements. The experimental element is kept in the linear regime since the simulated restoring force assumes a linear relationship between stiffness and target displacements. The adequacy of control and/or compensation algorithms that are implemented in the software framework was assessed in the latter, as shown in Figure 78b.

The *open-loop* hybrid test was conducted on the two-bay one-storey steel frame (frame-1) by scaling the peak ground acceleration (PGA) of the 1994 El Centro earthquake record to 0.03 g (PEER NGA-West2). Figure 78 shows that lateral displacement response of the steel frame from the *open-loop* hybrid test is in good agreement with the numerical solution of the problem. Tracking error in the testing system is acknowledged and the compensation parameters were revised.

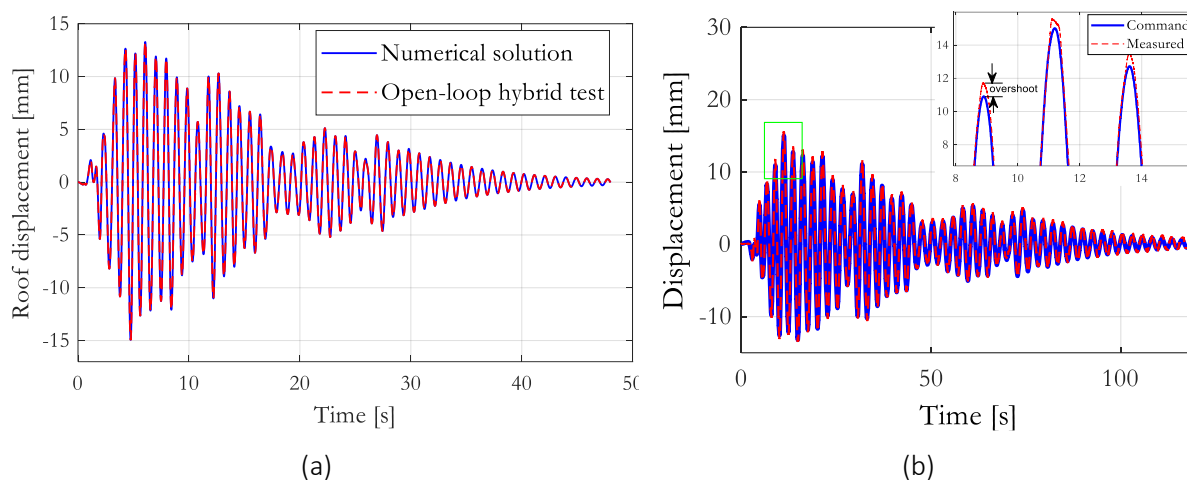


Figure 78: (a) Roof displacement comparison; (b) Tracking errors

2.3.4 Hybrid test experiment

The term closed-loop hybrid test refers to a hybrid test conducted by returning the measured restoring forces to the computational driver. In addition to the rehearsal test, a close-loop test at low excitation level helps in pointing out errors due to the feedback force. The experimental column is also kept strictly linear during the additional rehearsal test. This test was conducted during the current validation process. Small signal-to-noise, in the measured restoring force, is inevitable in these tests; nevertheless, fidelity of measured force can be improved using small-duty force transducers. For brevity, results of the latter test are not discussed in this chapter. However, results of a preliminary hybrid test conducted following the additional rehearsal test are discussed.

Hybrid test presented here refers to a test that was conducted on frame-1 only. The first mode of steel frame is 1.08 Hz. The measured restoring force was low pass filtered at 4 Hz using the 2nd order Butterworth filter. α -OS time-stepping algorithm drives the system solution based on deductions made from a parametric study that was conducted on robustness of one-step time-stepping algorithms. The alpha term (α) is taken as 0.9 in order to introduce a reasonable amount of numerical damping. The simulation was done by scaling the El Centro earthquake record to 0.03 g PGA at 4 ms time-step size. Adaptive time series (ATS) compensation was carried out in conjunction to prediction-correction process. At the end of the simulation, the true speed of the hybrid test, $\frac{\delta t_{sim}}{\delta t_{exp}}$, was calculated to be 27.8. Speed range for hybrid simulation between 20 and 50 is normally considered as fast. Hence, the experimental test conducted can be categorized as a fast hybrid test.

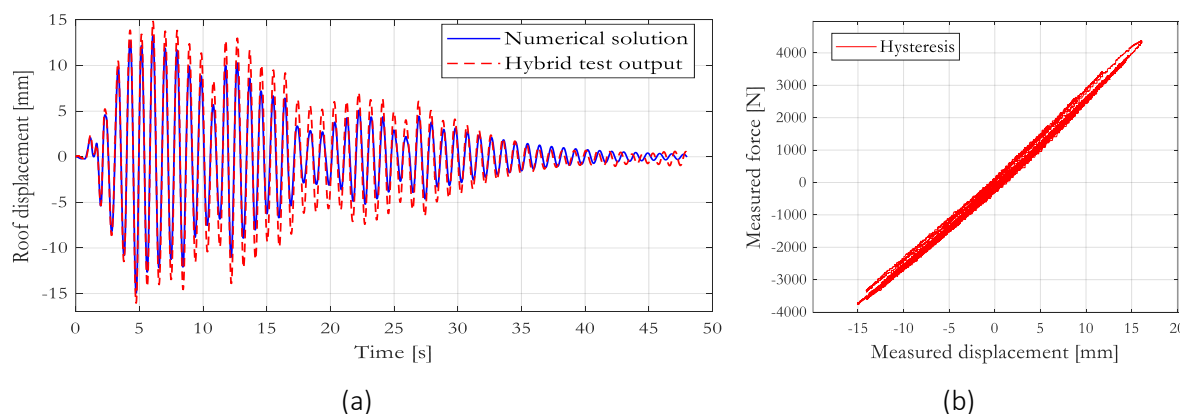


Figure 79: (a) Roof displacement comparison; (b) hysteresis loop

The controller algorithm over-shoots target displacements during the hybrid test. Over-shoot values as large as 20% can be depicted from Figure 79a. Nevertheless, error propagation was not observed since experimental errors during the hybrid test were compensated towards the end the test.

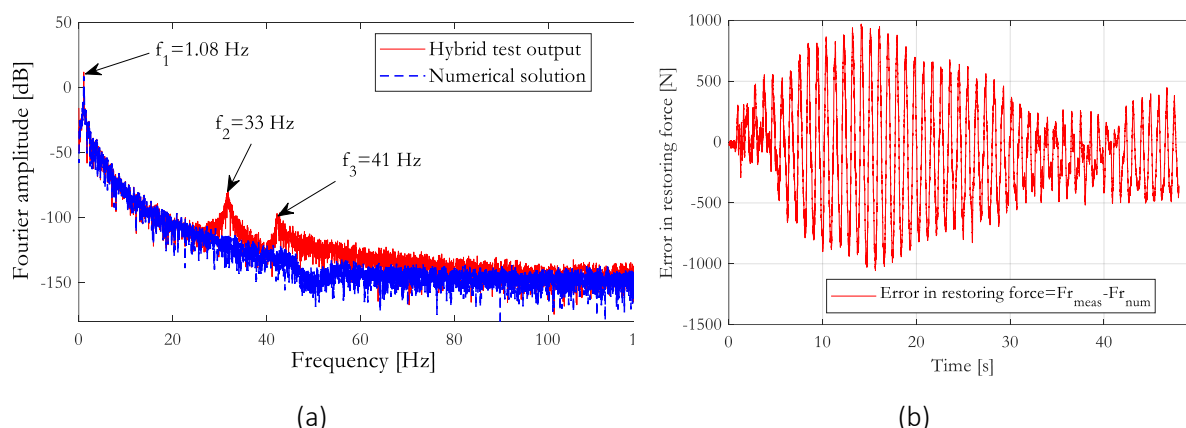


Figure 80: (a) Fourier amplitude of roof displacement; (b) error in restoring force

The overshoot observed during the experimental test may be resulted from excitation of the second and third modes of the structure which are 33 Hz, 41 Hz respectively. This reasoning can be seen in the frequency response of the lateral displacement shown in Figure 80. This entails the need for additional numerical damping and/or adjustment on setting compensation coefficients of ATS (includes both range and initial values). The control overshoot is also translated into an error in the restoring force as large as 1 kN. This is approximately equal to 25% of the maximum restoring force.

2.4 Soil-structure interaction analysis via HDS

As briefly discussed in the introduction, laboratory testing of soil-structure systems is complex and expensive. Past experimental studies were restricted to only cantilevered mass or tower-like structures and rarely were realistic structural models physically modelled. With the advent of HDS, full scale SSI tests with realistic structural models could be tested. Nevertheless, hybrid testing of a simple cantilever column by itself is not straightforward since the technique involves servo-hydraulic actuator and sensor dynamics. It is therefore easy to imagine the challenges in conducting HDS of a structure considering SSI.

Several SSI hybrid dynamic simulations (HDS) were conducted in the last decade, most of which had the SSI component modelled as a numerical substructure. A few experimental tests, however, have been carried out on a soil-foundation setup while modelling the superstructure numerically. Multiple superstructures resting on a pile-group foundation in a saturated sandy soil contained in a laminar box were tested at the University of Buffalo. The test setup included a shake table imposing a ground motion at the base of the laminar box, while a small shake table applies the interface force that is transmitted from the superstructure to the foundation. The challenges in performing the latter configuration lies in the real-time control of the interface boundary conditions. Experimental testing of lower stories of a structure may necessarily need the equilibrium condition to be satisfied, at the interface boundary, instead of the traditional compatibility criteria. A hybrid test setup that has a superstructure portion erected on a soil has not been attempted to date due to its complexity. The current research is designed to tackle and conduct hybrid tests of such a kind.

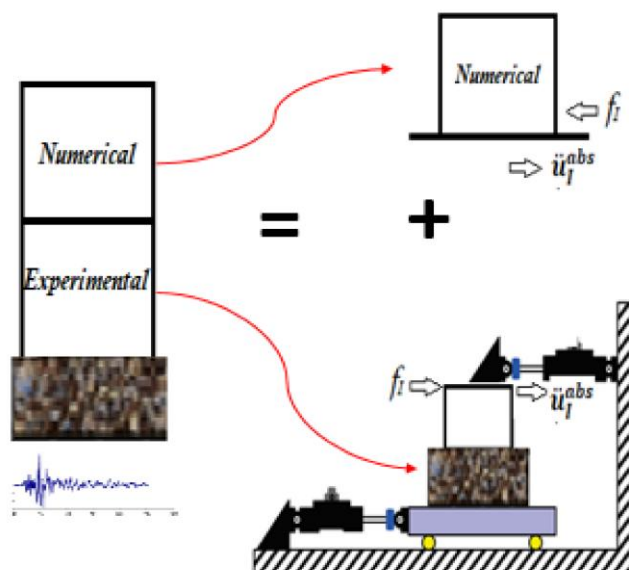


Figure 81: Test scheme for SSI analysis using HDS

Besides, the directHS framework has integrated Smith-predictor and Linear Quadratic Gaussian (LQG) controllers both working in cascade with a PID controller. The former aims to compensate actuator dynamics under an equivalent force control via added compliance, while the latter is dedicated for acceleration tracking of the shake table; both are model-based controllers.

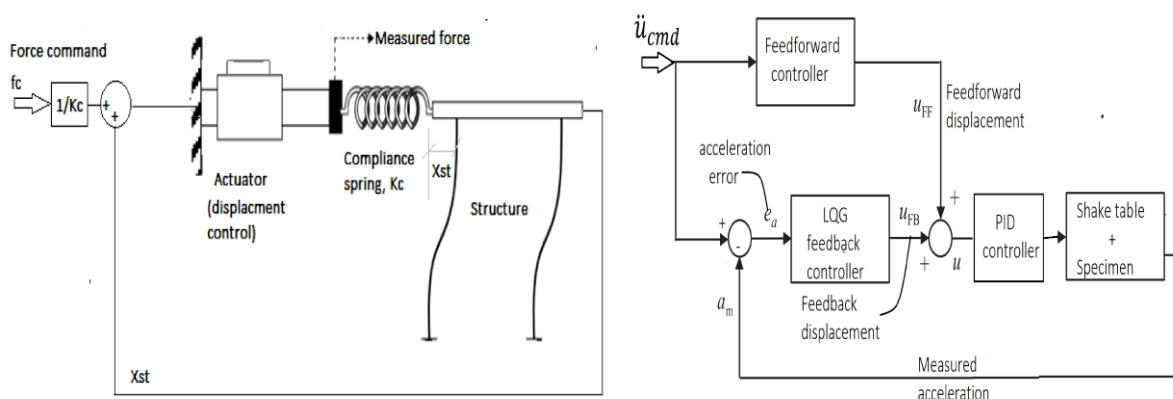


Figure 82: Equivalent force control via added compliance (left) and feedforward-feedback controller for a shake table (right)

Test preparation in SSI testing is essential and takes a significant effort. The soil-container should be designed to achieve similarity of responses between the model and the 1D semi-infinite soil layer. In the present design, it was considered that the boundary effects would be minimized if the dynamic response of an idealized soil layer with the internal dimensions of the container matched the joint response of the soil and the container. Following the approach by Zeng and Schofield (1996), the base and end walls of the container are covered by a thin sheet of aluminium glued to the base of the container and covered with a slim layer of glued coarse sand all over its internal face.

Soil filling is performed by diving the total height of soil in three layers at constant velocity of pluviation. In each layer, the opening width is adjusted to achieve a relatively homogenous soil deposit.

During the test, a full description of the foundation flexibility is captured through an array of transducers. Both the linear and nonlinear responses of the soil-foundation interaction are analysed with emphasis on the nonlinear elastic uplifting and soil plasticity properties.

A two-storey steel shear-frame system resting on a dry well-graded sand with negligible embedment depth forms the reference test structure. The 2nd storey columns are designed to remain elastic throughout the tests while the 1st storey columns can become inelastic. The 1st storey columns together with the foundation soil are tested physically leaving the 2nd storey columns to be modelled numerically. A two-dimensional problem is considered, but the experimental setup is designed as a 3D frame with identical columns to maintain frame's stability and restrict out of plane movements. A rigid diaphragm supported by beams on its periphery models the lumped mass on the 2nd storey. The mass of the system can be easily adjusted by adding mass blocks to the top of the diaphragm.

The foundation soil is filled into a flexible soil container that is constructed from alternating aluminium rings and rubber-like elastomeric layers. The container has 2×0.75×1.75m dimensions. A soil pluviation machine fills the container to achieve the desired soil properties. The sand that had been already characterized in the past is used in this study. The combined soil and container fundamental frequency was reported to be around 13.9 Hz.

Data acquisition of the test setup is envisaged to include: displacement transducers at the base of the container, at the foundation level, at the interface boundary (or top) and along the height of the container; acceleration transducers at the interface boundary, bottom of the soil-container and at the foundation level; and force transducers that are connected to the shake table and auxiliary actuator. Transducers are arranged in an array in a way to correctly capture uplifting and settlement of the test specimen.

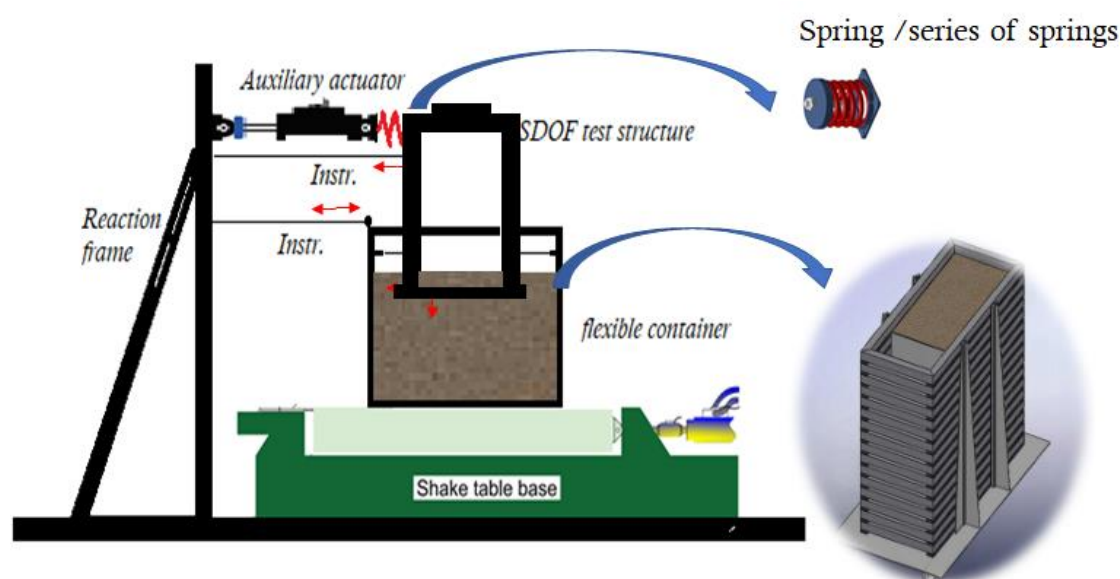


Figure 83: Test setup for soil-structure analysis via HDS

Note that the auxiliary actuator is controlled in displacement feedback but the original command from the numerical substructure is the shear force at the base of the 2nd storey. This is accomplished by the added compliance system since the actuator-spring assembly forms a flexible loading system where force control can be applied given that the spring remains elastic. The spring coil should have a stiffness less than or equal to the structure's stiffness. Care must be taken however not to make the spring overly flexible because the total displacement may exceed the stroke limit of the auxiliary actuator. The measured absolute acceleration at the roof of the test specimen is recorded, filtered and returned to the numerical model and serves as the input motion to the numerical model.

During the initial validation steps, open-loop test is executed under a simulation environment where the feedback (absolute acceleration) is simulated from a purely numerical analysis conducted prior to the validation test. In the validation test, the shake table and auxiliary actuator are synchronized to apply very small magnitudes of motion to prevent damage of the test specimen. True hybrid tests with progressively increasing amplitudes of input motion are then conducted following the validation experiments.

3 Use of HDS for thermomechanical applications

Large-scale structural fire tests are rare because of the need for expensive specialized facilities. As a result, most of the research regarding the behaviour of structures in fire has been carried out on single structural components subjected to standard heating curves. Although such tests offer significant information about the fire performance of specific structural elements, they do not account for force redistribution owing to the interaction of the tested structural component with the remaining part of the structure. In order to overcome such limitations, HDS emerged as a viable alternative to both large-scale and component fire testing in the last two decades.

Hybrid fire simulation (HFS) indicates the specific application of HDS to structures subjected to fire. The seminal paper of Korzen et al. (1999) describes the first proof-of-concept HFS of a steel frame with a single physical column subjected to fire. Subsequently, CERIB-Prométhée testing facility in Epernon, France developed a HFS setup consisting of a gas-fired furnace with integrated mechanical loading frames that can reproduce interactions between the parts of the structure under testing and those that are unexposed to fire (Robert et al., 2009). Later, Mostafaei (2013a, 2013b) tested a hybrid model of a 6-storey reinforced concrete building. In this case, interface boundary conditions between NS and PS were manually adjusted. Whyte et al. (2015) extended the Open-source Framework for Experimental Setup and Control (OpenFresco) (Schellenberg et al., 2007) middleware to impose temperature loads on mechanically tested components using computer-controlled electric furnaces in an online manner. Sauca et al. (2018) proposed a nonlinear static algorithm to perform HFS. Wang et al. (2018) recently performed HFS of vertically loaded stiff columns compensating for the deformation of the reaction frame. There is a flurry of interest in HFS, as testified by several recently presented conference papers (Qureshi and Elhami-Khorasani, 2018; Mergny et al., 2018; Schulthless and Neuenschwander (2016)). However, there is still a lot of work to be done to improve HFS.

A 3-Degree-of-Freedom (DOF) thermomechanical (TM) test rig was recently developed at ETH Zurich for testing 200x500x2 mm plates under different thermal and mechanical boundary conditions. In detail, four electromechanical actuators provided with load cells impose displacement/rotation to both plate edges and read corresponding force/moment while infrared lamps, Peltier modules and heat flux gauges control the thermal response of the specimen. A real-time computer coordinates both thermal and mechanical actuation devices as well as data acquisition. Starting from the existing test rig, the goal of this project is to develop a thermomechanical hybrid simulation platform. This research expands the state-of-the-art paradigm of HDS, which mainly focused in the area of structural seismic testing, towards stochastic multi-physic hybrid simulation.

Section 3.1 describes the 3-DOF TM test rig, section 3.2 describes a verification HFS experiment and section 3.3 describes a series of HFSs performed on a composite plate. Finally, conclusions are given in section 3.4.

3.1 Thermomechanical test rig

The 3-DOF TM test rig combines a mechanical and a thermal transfer system that allow the application of mechanical and thermal boundary conditions (BCs) to a plate specimen of 200x500 footprint and thickness varying between 1 and 3 mm. A real-time computer controls the two transfer systems and computes the prototype structure response. Figure 84 describes the architecture of the TM test rig.

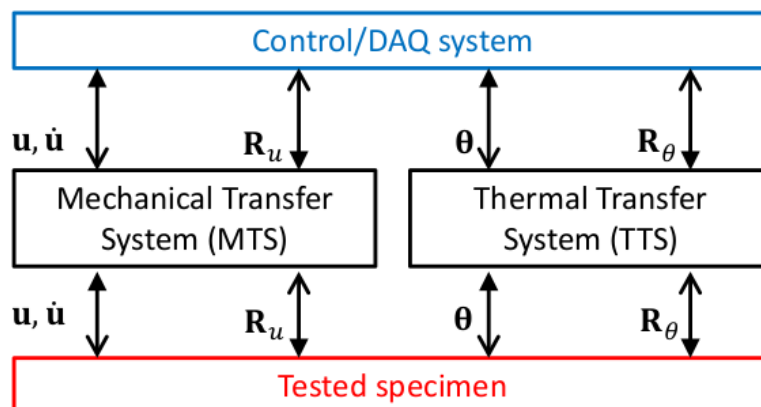


Figure 84. Architecture of the 3-DOF TM test rig.

3.1.1 Mechanical transfer system

The mechanical transfer system (MTS) consists of a loading frame equipped with four electromechanical linear actuators and load cells that impose displacements/rotations and measure the corresponding reaction forces/moments on the specimen boundaries. The plate specimens are held by two clamps on short edges and are free on long edges. Figure 85 shows the whole loading frame (left) and a close-up view of the linear actuators and load cells (right).

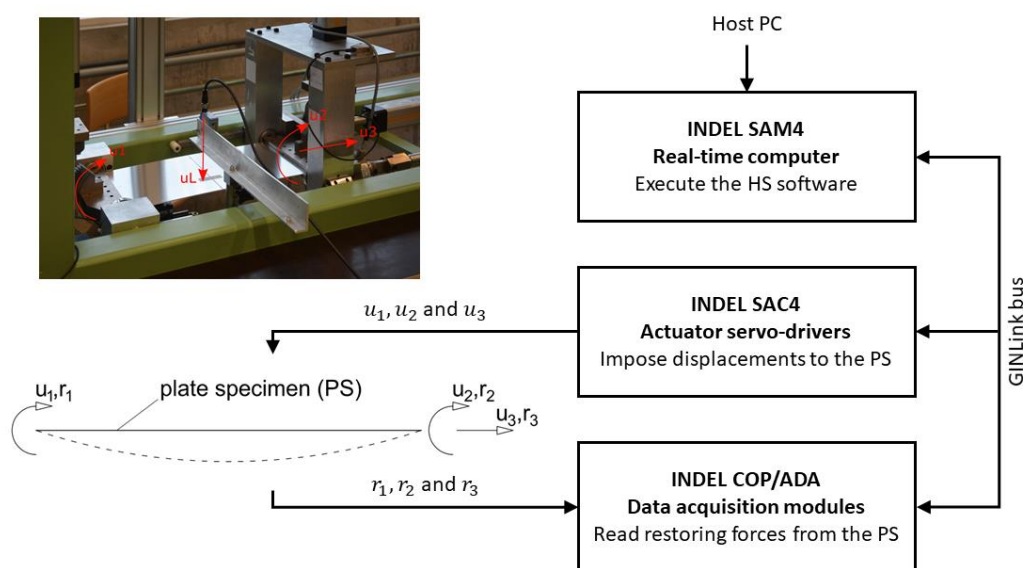


Figure 85. MTS of the 3-DOF TM test rig: with close-up view with an installed aluminum plate.

Two of the actuators are positioned in the specimen plane in order to apply axial displacements/forces (axial actuators). The two actuators orthogonal to the specimen plane apply rotations/bending moments at the plate edges through a translation-to-rotation transfer system (bending actuators). Laser positioning sensors and two angular optical resolvers are installed in order to improve the control feedback. Table 14 summarizes the measurement ranges and errors of the sensors.

Table 14: Measurement ranges and errors of the MTS sensors

Sensor	Measurement range	Error
Actuator displacement	± 75 mm	± 0.03 mm
Laser positioning sensor	± 90 mm	± 0.09 mm
Angular resolver	360°	$0.25''$
Load cell	± 10 kN / ± 0.5 kNm	0.003 %

3.1.2 Thermal transfer system

The thermal transfer system (TTS) combines an infrared (IR) lamp for heating, eight Peltier heating/cooling elements to impose temperatures and an IR camera to measure the temperature field of the tested specimen from above. Furthermore, thermocouples are installed to measure the temperature and control the IR lamp and Peltier arrays. Figure 86 shows the installed IR lamp and IR camera (left) and the Peltier arrays and thermocouples (right).

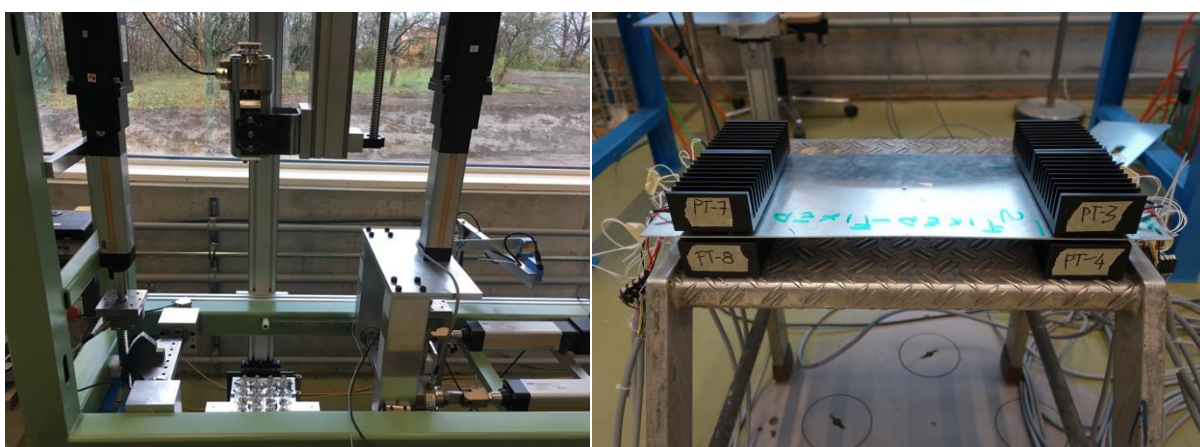


Figure 86. TTS of the 3-DOF TM test rig: IR lamp and IR camera (left) and Peltier arrays and thermocouples being installed to an aluminum plate (right)

The IR lamp heats up the tested specimen from below with a temperature range between 20 and 180 °C at a maximum rate of 2 °C/s. It includes 16 bulbs and absorbs a maximum power of 1150 W. In order to adjust the temperature at both short edges of the plate, two arrays of four Peltier thermoelectric modules each are installed. On the part of the hardware, a range of ± 83 °C with respect to the bulk temperature is feasible. However, currently it is not possible to go below room temperature (RT). This limitation probably results from the capacity of Peltier module heat exchangers or from the way the Peltier modules controllers are programmed and implemented. For each Peltier module the temperatures of the two surfaces are measured by one thermocouple each. Another thermocouple is installed to measure the specimen temperature at the midpoint of the IR lamp footprint. Depending on the setting, the IR camera can measure temperatures between -20 and 900 °C at a frequency of up to 80 Hz. Table 15 summarizes the measurement ranges and errors of the sensors.

Table 15: Measurement ranges and errors of the TTS sensors

Sensor	Measurement range	Error
IR lamp	20 to 180 °C	-
Peltier module	± 288 W ± 83 °C	± 0.5 K
Thermocouple	-100 to 400 °C	-
IR camera with jacket	382x288 pixel @ 80 Hz -20 to 900 °C	± 2 °C or $\pm 2\%$

As can be appreciated from Figure 86, Peltier modules are quite massive and easily bend a thin composite plate (the plates in the setup are aluminium). Accordingly, Peltier modules were not used in composite plate tests. Furthermore, during thermal experiments the laser sensor measuring the out-of-plane displacements was removed. In order to use Peltier module on thin plate specimens, their harnessing and heatsink size needs to be reduced.

3.1.3 Real-time control system

In order to coordinate the MTS and TTS, a real-time computer (RTC) was designed for this specific application (see Figure 87, left). It is based on a quad-core INDEL GIN-SAM4 4x2.2G system and is controlled by a Windows based Host-PC via a graphical user interface (GUI) generated with a python script. A screenshot of the GUI is shown in Figure 87, right, where the green portion controls the actuators (MTS) and the blue and pink parts regulate the IR lamp and Peltier arrays (TTS). A Simulink model developed on the Host-PC generates a C-code which is then executed by the RTC. The Host-PC is connected to the RTC via Ethernet, which is in turn wired to the TM-TR. If a HS is conducted, the RTC also emulates the NS that is virtually coupled to the PS.

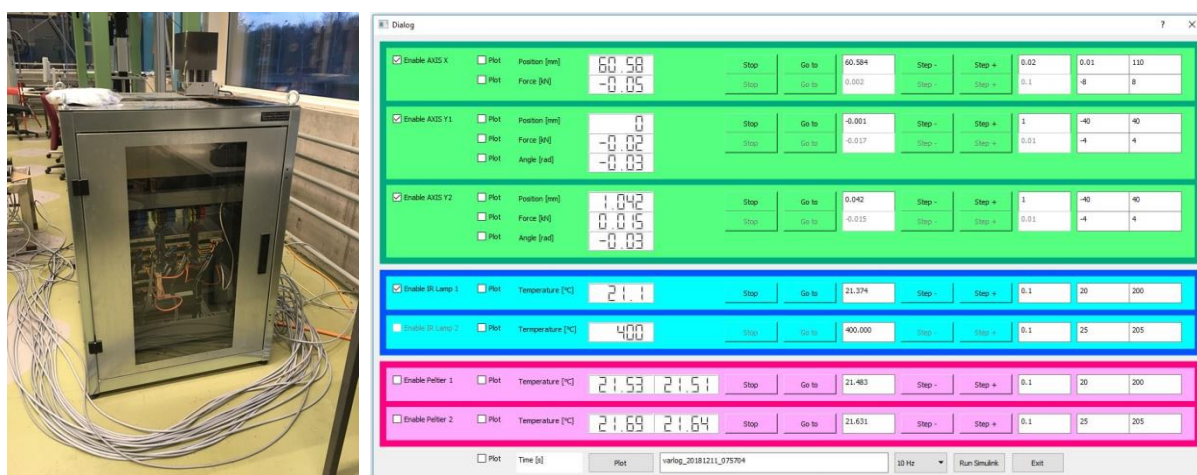


Figure 87. Real-time computer (left) and screenshot of the GUI (right)

3.2 Verification of the MTF

3.2.1 Benchmark case study

The prototype structure consists of an in-plane simply-supported beam provided with linear elastic torsional restraints at both ends and subjected to a ground motion excitation, which acts in the orthogonal direction with respect to the beam axis. Figure 88 provides a schematic view of the prototype structure and its substructuring into PS and NS for the purpose of HDS.

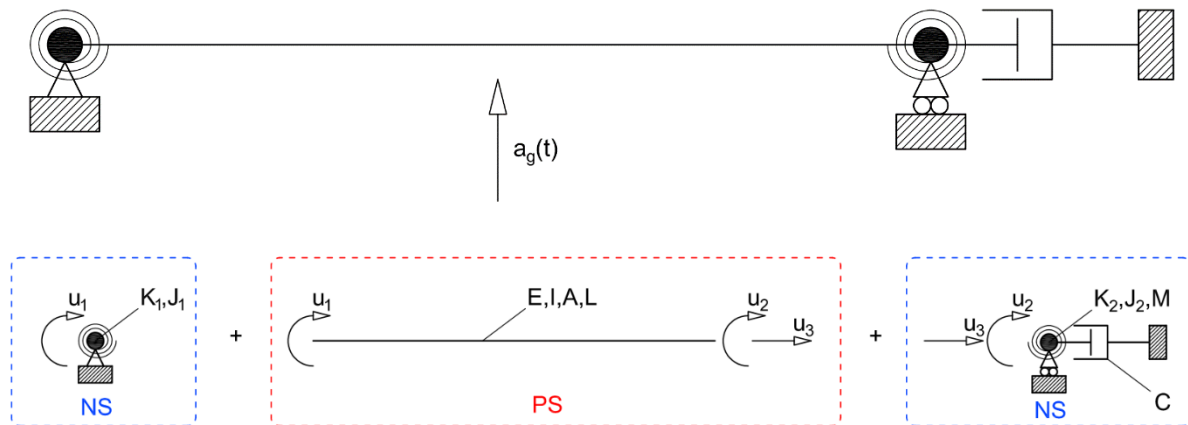


Figure 88 Benchmark case study: (top) reference structure; (bottom) prototype structure.

According to Figure 88, u_1 and u_2 indicate the two rotational DoFs of the simply-supported beam, while u_3 corresponds to the axial DoF. The PS consists of a steel plate (Young modulus $E = 100$ GPa density $\rho = 7850$ kg/m³), which is assimilated to a 3-DoFs beam, of 200×2 mm cross-section ($A = 400$ mm² area and $I = 133$ mm⁴ inertia) and $L = 470$ mm length. The distributed seismic mass is computed according to the Bernoulli beam theory and condensed to the three retained DoFs. The NS comprises two rotational masses $J_1 = J_2 = 0.9$ kgm², a lumped mass $M = 20,000$ kg, a linear dashpot $C = 300,000$ Ns/m and two linear elastic torsional springs, with stiffness K_1 and K_2 of 70 Nm/rad.

The velocity-pulse model proposed by Dabaghi and Der Kiureghian (2018), which describes near-field ground motions, defines the lateral loading excitation. The velocity-pulse model consists on a cosine wave of period T_p modulated by a truncated cosine function, namely the pulse function, of period γT_p and amplitude V_p . The latter corresponds to the peak velocity of the pulse located at $t_{max,p}$. The expression of the velocity-pulse reads:

$$v_g(t) = \left(\frac{V_p}{2} \cos \left(2\pi \left(\frac{t - t_{max,p}}{T_p} \right) + \nu \right) - \frac{D_r}{\gamma T_p} \right) \left(1 + \cos \left(\frac{2\pi}{\gamma} \left(\frac{t - t_{max,p}}{T_p} \right) \right) \right)$$

where ν is the phase angle between the cosine wave and pulse function, while D_r is the residual non-zero displacement at the end of the pulse. The velocity-pulse model is defined for $t \in \{0, \gamma T_p\}$ and zero outside this interval. In order to reduce the number of free parameters, the velocity pulse peak is located at $t_{max,p} = \frac{\gamma T_p}{2}$ fixed values are set to $\gamma = 2$ and $\nu = 0.1$ whereas $V_p = 1.25$ m/s and $T_p = 2$ s. The transverse inertial acceleration $a_g(t)$ applied to the prototype structure corresponds to the time derivative of the velocity-pulse model. Figure 89 depicts a realization of the velocity-pulse model with main parameters highlighted.

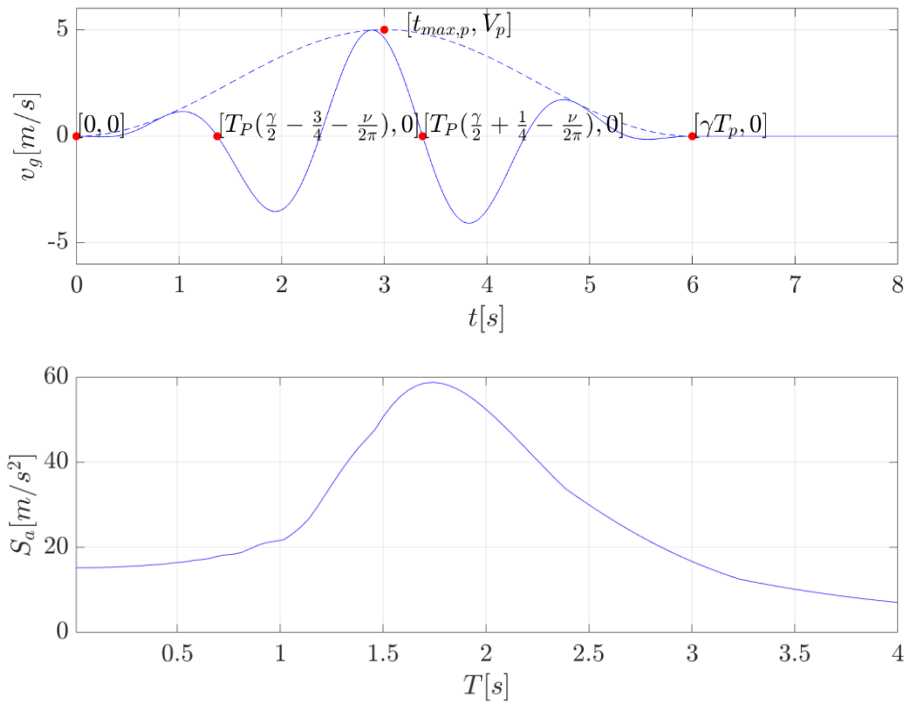


Figure 89 Velocity-pulse history with main parameters highlighted (top) and corresponding acceleration response spectrum with 5 % proportional damping (bottom).

3.2.2 Results and discussions

The outcome of a HDS simulation in terms of response histories of u_1 and r_1 is reported in Figure 90, where corresponding peak quantities $u_{1,max}$ and $r_{1,max}$ are also highlighted.

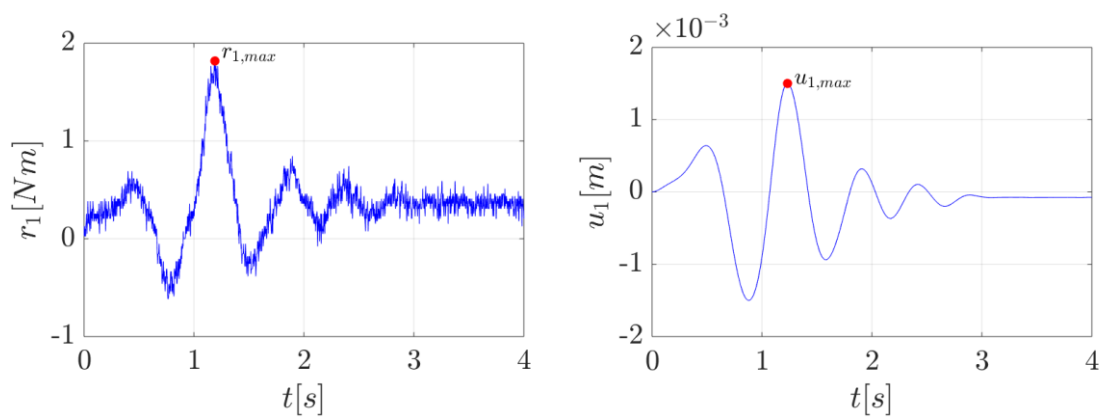


Figure 90 Examples of rotation (a) and bending moment (b) response histories obtained via HS with peak quantities highlighted.

The time-history response of r_1 is much noisier than that of u_1 . This is a common occurrence with non-stiff specimens that produce low reaction forces for appreciable displacements.

3.3 Verification of the TTF

3.3.1 Benchmark case study

In order to verify the TTF of the 3-DOF TM test rig, a composite plate based on the PowerRibs technology was tested. The PowerRibs technology is a natural fiber composite reinforcement grid which is added to a base layer (substrate) in order to improve its mechanical properties. A composite plate of 420x200x2 mm size produced by Bcomp (2019) was tested (see Figure 91).



Figure 91. PowerRibs composite plate (420x200x2 mm) produced by Bcomp.

Table 16 summarizes the material properties of the different layers, which are later considered for the implementation of the numerical model. For the powerRibs 5020 the parameters are given by Bcomp. However, most of the parameters for the ampliTex 5040 have to be taken from literature. At the crossing points of the powerRibs the fibers in the short direction remain flat while the fibers in the long direction lie above. This circumstance leads to different Young's moduli and thermal expansion coefficients for the powerRibs in the two directions.

Table 16: Material properties of the PowerRibs composite plate (* Sparnins, 2009; ** Powell et al., 2002; *** Lewin, 2007)

Material	Thick. [mm]	Density [kg/m ³]	Poisson's ratio [-]	Young's Mod. 1 [GPa]	Young's Mod. 2 [GPa]	Thermal expan. 1 [1/K]	Thermal expan. 2 [1/K]	Thermal cond. [W/m·K]	Heat capacity [kJ/kg·K]
ampliTex 5040	0.7	1350	0.22 *	18.1	18.1	$5 \cdot 10^{-6}$ *	$5 \cdot 10^{-6}$ *	0.02 **	1.35 ***
powerRib 5020	0.83	265	0.04	1.92	1.89	$20.6 \cdot 10^{-6}$	$5.6 \cdot 10^{-6}$	0.33	2.4

1 ... wavy ribs direction (long side)

2 ... flat ribs direction (short side)

Figure 92 depicts a schematic of the installation of the PowerRibs composite plate installation in the 3-DOF TM test rig.

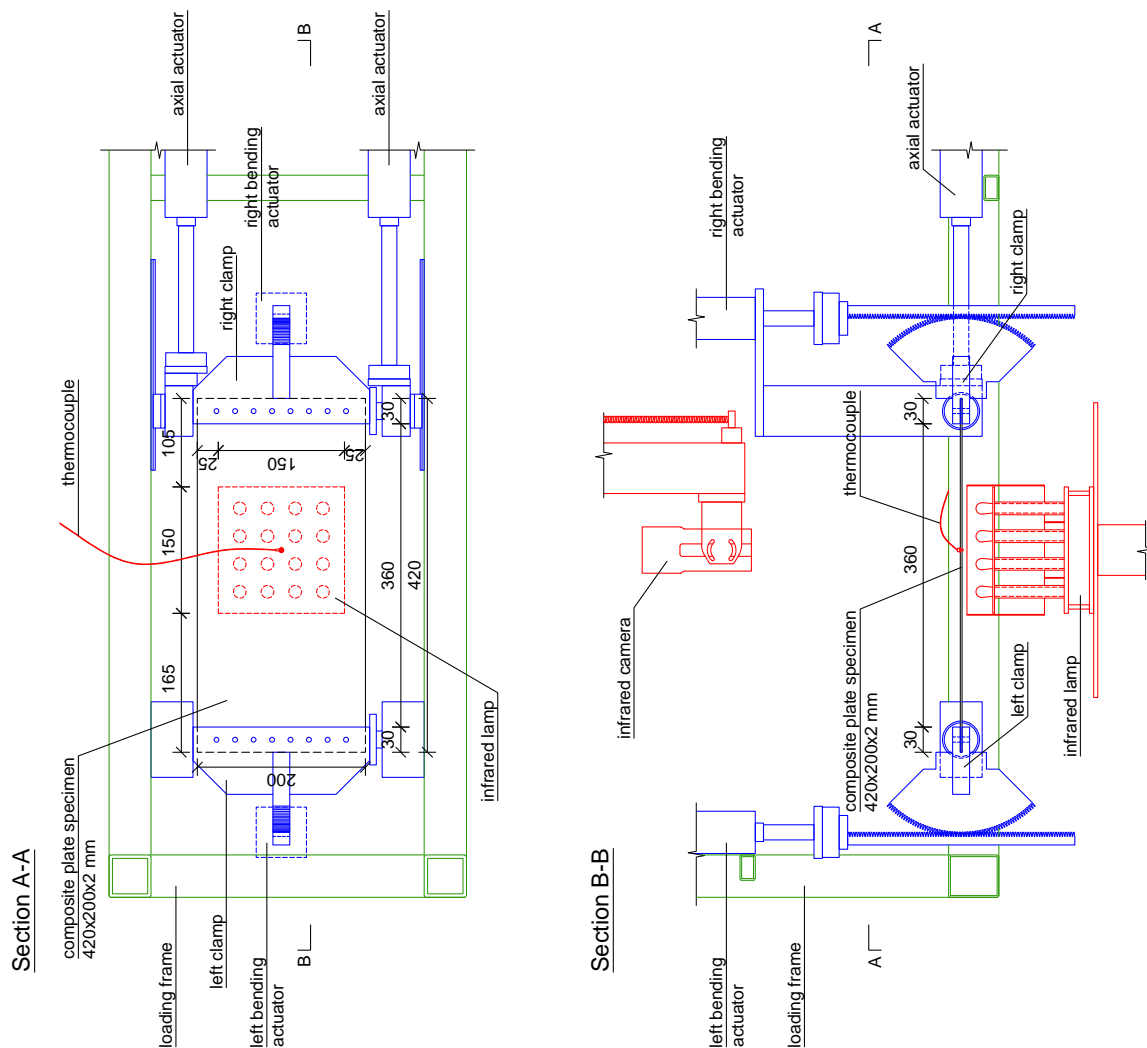


Figure 92. Schematic configuration of the TM-TR for the thermal testing of the PowerRib composite plate in top view (above) and side view (below) [dimensions in mm]

The plate was heated from the bottom side under fixed-fixed boundary conditions. The thermal loading was produced with the IR lamp. Starting from room temperature (about 23 °C), the specimen was heated up to 90 °C linearly during the first 10 minutes. Afterwards, the temperature was kept to 90 °C during another 40 minutes. Figure 93 shows the clamped composite plate before and during the heating process.



Figure 93. Tested composite plate specimen with inactive (left) and active (right) IR lamp

During the test the temperature of the material at the middle of the IR lamp footprint was measured continuously with the thermocouple. Furthermore, the temperature field was recorded every 2 seconds with the IR camera above. The mechanical response was measured with the load cells at the actuators.

3.3.2 Results and discussions

The time histories of the temperature measured by thermocouple and by the IR camera for a point close to the thermocouple are compared in Figure 94. One can observe the steady increase during the first 10 minutes and oscillations around a constant value afterwards. The temperature measured by the IR camera during the plateau phase is about 88 ± 17 °C. The thermocouple gives a slightly larger average value of 94 °C and a variation of ± 6 °C.

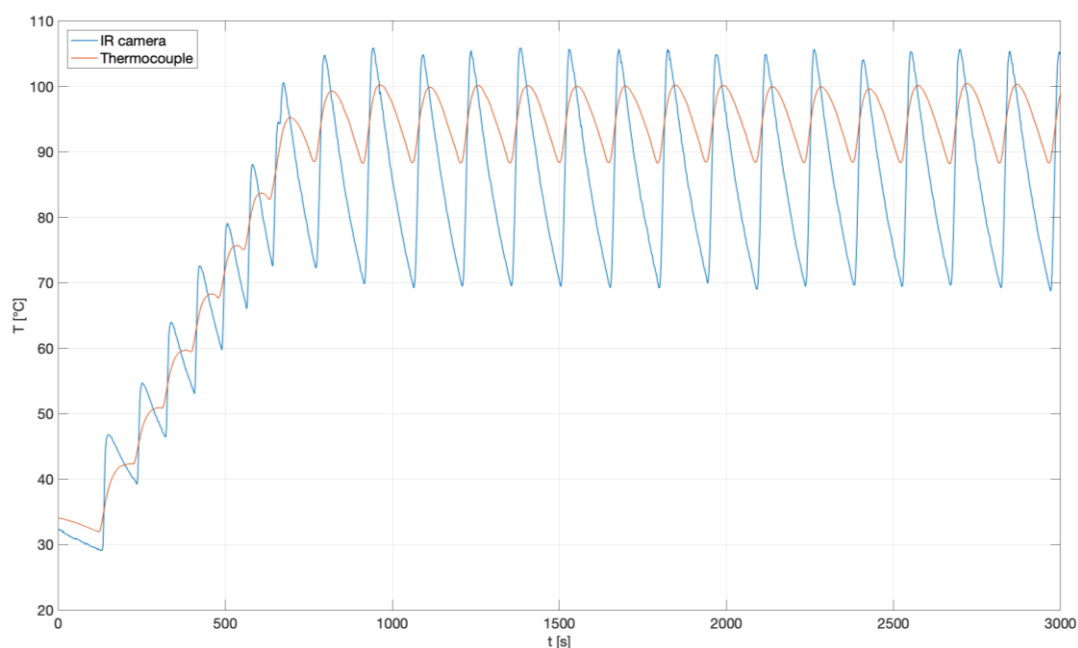


Figure 94. Time history of the temperature measured by the IR camera and the thermocouple

Figure 95 shows the temperature field measured by the IR camera at four different points in time. At the initial condition, the specimen has a constant temperature of about 23 °C (a). As the heating starts, the footprint of the IR lamp becomes clearly visible. Around its edge one can see the temperature gradient down to ambient temperature. It can also be observed that the PowerRib composite plate show lower temperatures than the substrate during heating (b and c). When the temperature becomes lowest during the oscillation, the opposite is the case (d). The maximum temperature at the PowerRib composite plate is about 140 °C and up to 200 °C for the substrate material.

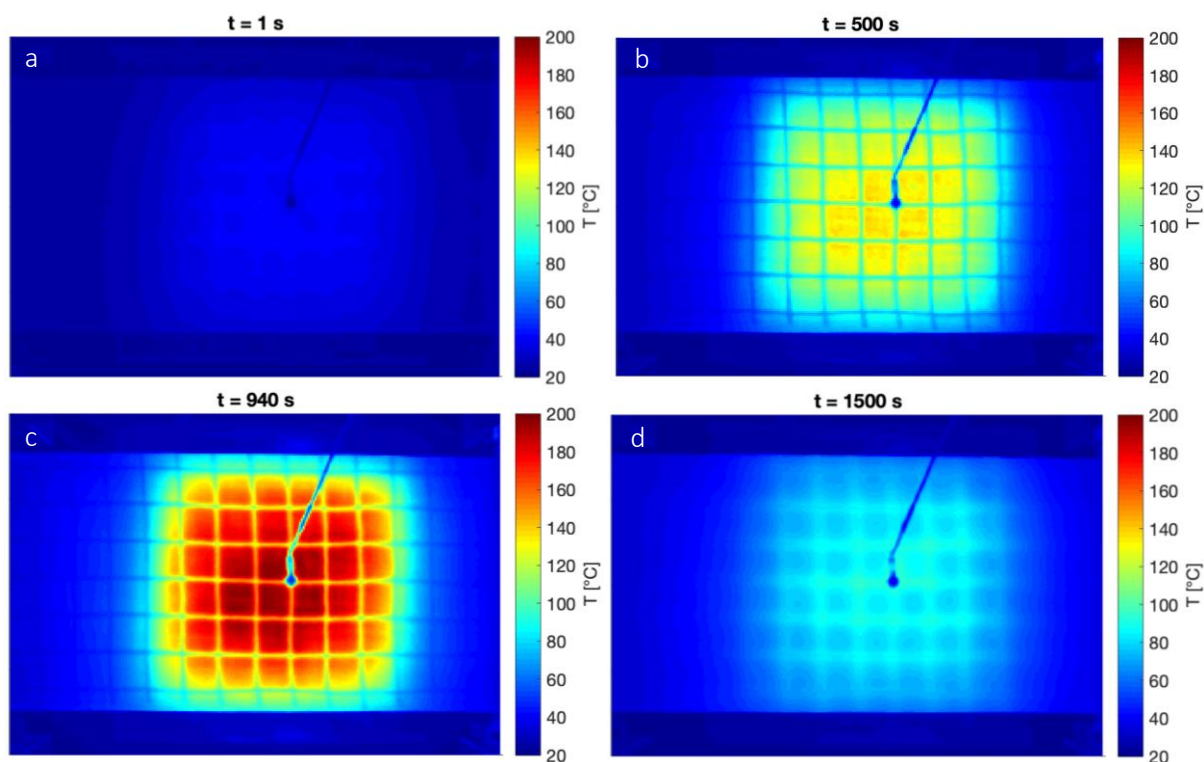


Figure 95. Temperature fields before heating (a), during heating-up (b), at maximum temperature (c) and at minimum temperature (d)

In order to determine an average temperature for the IR lamp footprint, the mean temperature field during the plateau temperature phase was calculated. The result is presented in Figure 96, complemented by the border of the IR lamp footprint with a maximum temperature of $140 \text{ }^{\circ}\text{C}$. The average temperature within this footprint is about $110 \text{ }^{\circ}\text{C}$.

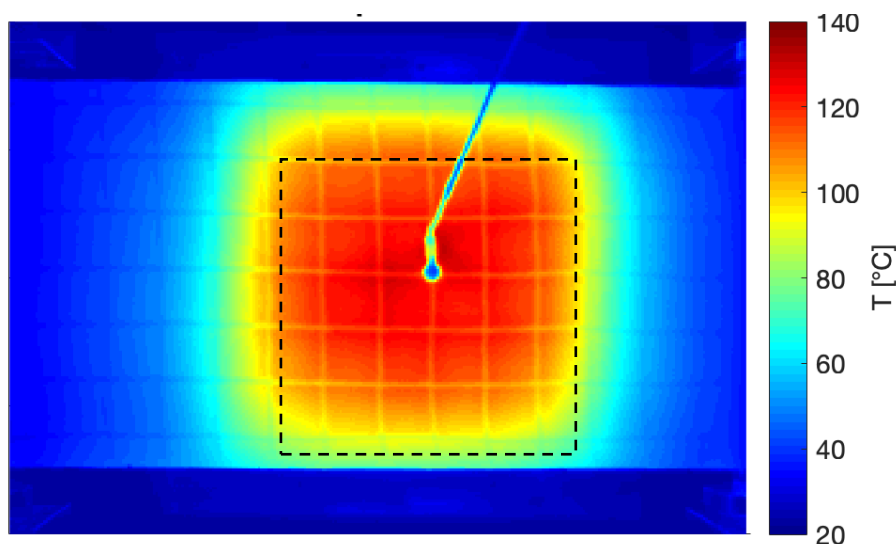


Figure 96. Time-averaged temperature field with the IR lamp footprint

Figure 97 shows the temporal development of the axial reaction force measured by the load cell. One can observe the rise in the beginning, correlating with the heating-up phase. Afterwards, the axial force oscillates accordingly to the temperature, but starts to decrease slowly. After the heating-up the value is about $350 \pm 200 \text{ N}$ and reduces to $250 \pm 190 \text{ N}$ by the end of the experiment.

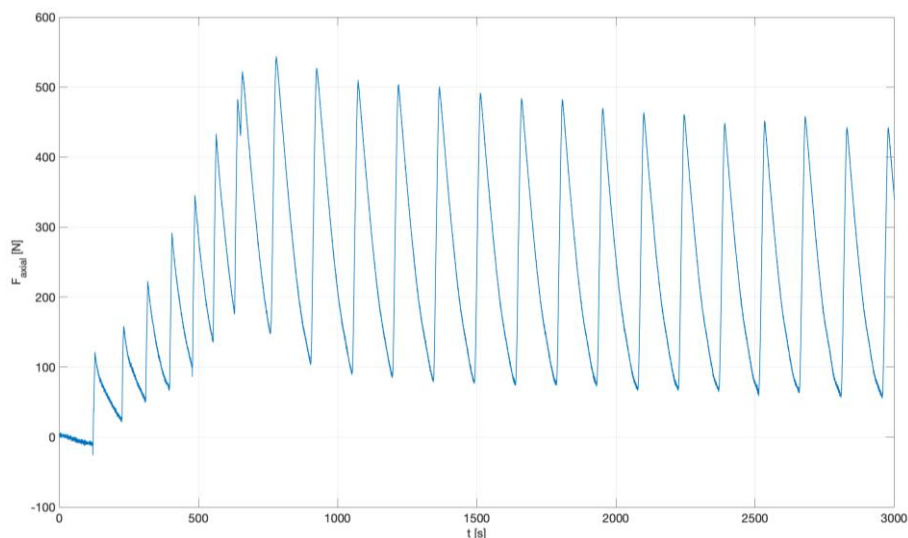


Figure 97. Time history of the axial reaction force measured by the load cell

The time histories of the temperature show a much stronger oscillation for the IR camera measurements. However, the average temperature is closer to the predefined value of 90 °C. The results of the thermocouple measurements might be influenced by the thermal conductivity of the metal screw, which was drilled through the plate in order to fix it. One can also observe that the oscillations of the IR camera measurements (Figure 94) correlate better with the ones of the axial force (Figure 97). The thermocouple measurements, however, are slightly shifted in time. A further advantage of the IR camera is the fact that temperature is not only measured at one single point, but over the whole specimen. The observation that the PowerRibs composite plate show lower temperatures than the substrate material (Figure 95 and Figure 96) is an indication for a higher thermal conductivity of the PowerRibs composite plate. Therefore, heat flows away faster and temperature gets lower. This finding also matches the material properties from Table 16. The temperature peaks of up to 200 °C occur only temporary due to the heat bursts of the IR lamp and do not represent a long-term condition. As already mentioned, the variation of the measured axial reaction force correlates well with the IR camera measurements. It is a consequence of prevented thermal expansion of the material due to the two fixed clamps. Although the average temperature is kept constant after the heating-up, the average force starts to reduce. This implies a stress relaxation of the material, as the thermal strains stay more or less constant while the stress response decreases.

3.4 OpenFresco Class

The concept of HFS was briefly reviewed first, followed by a presentation of the mechanical and thermal transfer systems of the TM test rig at ETH Zürich. The performance of the mechanical and the thermal transfer systems was demonstrated separately.

The next step is the conduct of HFS. In order to enable HDS with existing FE software, an OpenFresco control class will be tailored to the 3-DOF TM test rig following the architecture proposed by Whyte et al. (2015) and reported in Figure 98.

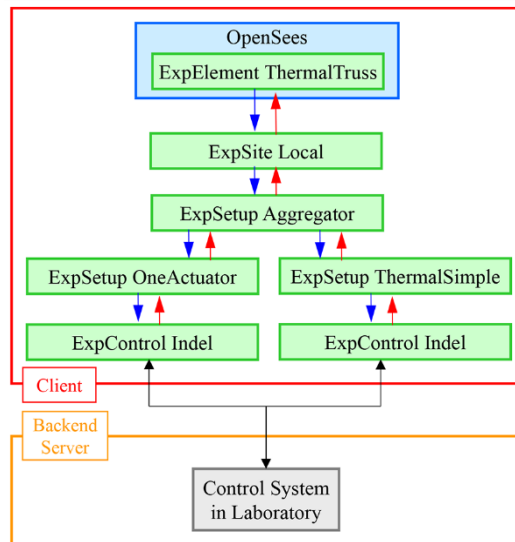


Figure 98 Class diagram of the OpenFresco framework reported in Whyte et al. (2015)

With regards to Figure 98, a 3-DOF *ThermalShell* will replace the 1-DOF *ThermalTruss* experimental element class. Similarly, a *ThreeActuator* experimental setup class will be coded to handle the three axes of the 3-DOF TM test rig. On the other side, *ThermalMulti* experimental setup class will control the two arrays of Peltier modules and the infrared lamp. Finally, SAFIR (Franssen and Gernay, 2017), which is a finite-element code for analysis of structures subjected to fire, may be used as finite-element analysis software instead of OpenSees (McKenna et al., 2000).

4 Conclusions and future developments

4.1.1 Conclusions

An improved displacement-dependent damper with recentering capability and multiphased nature was developed. It consists of the tube-in-tube assemblage of two commonly available hollow structural sections made of stainless-steel, and a central bar of large diameter made of NiTi alloys. To characterize the hysteretic behavior of NiTi bars several specimens were subjected to cyclic loading in both static and dynamic conditions, and at different frequencies. Some of them were tested up to failure to evaluate the ultimate energy dissipation capacity under low-cycle fatigue.

Under cyclic static loads at constant amplitude the shape of the hysteretic loops stabilized after few cycles of deformation and the residual strain remained unaffected. Under dynamic loadings, the shape of the hysteretic loop is influenced by the frequency of loading. Increasing the frequency increases the loading and unloading stresses and reduces the amount of energy dissipated in each cycle, while the residual stress remains constant. All specimens showed similar equivalent viscous damping ratios that ranged between 2.5% and 3% under dynamic frequencies. The amount of energy dissipated under dynamic loading was 62% of that dissipated under static loads, and about 40% lower than the values reported in the literature for NiTi wires. An expression is proposed to quantify the ultimate energy dissipation capacity to failure in terms of number of cycles at constant amplitude, and the normalized energy dissipation in one cycle. From test results, a simple flag-shape numerical model is proposed to represent the hysteretic behaviour of NiTi bars under arbitrary cyclic loading.

Moreover, to modify the 5% elastic spectrum for higher values of damping, new expressions for damping correction factors (DCFs) were developed. The new DCFs are intended to be used for the design of structures with energy dissipation systems. DCFs for the spectral displacement, velocity and acceleration were calculated through time history analyses using 880 far-field accelerograms recorded in Europe. The new DCFs extends the current expression of Eurocode 8 to damping ratios over 28%, and improve its accuracy in the long and short period range.

On the other hand, in order to fully understand the response characteristics and contribution of fibre-reinforced elastomeric isolators (FREIs) to seismic vulnerability reduction, they have been tested in actual conditions, because previous experimental studies are rather limited in scope and extent. Along these lines, the main objectives of the experimental work were to investigate the behaviour of such bearings and, in particular, the temperature effects developed during cycling at large deformations.

Afterwards, the development and validation of a software framework for HDS of soil-structure systems was presented. Fundamental principles and ingredients of hybrid simulation were introduced and existing software frameworks for hybrid simulation were discussed. The architecture adopted in the current development, a three-loop architecture, was introduced and the state-machine software was explained in stepwise manner. The flexibility and modularity offered by this software are pointed out and its implications on the future extension of the framework were addressed. OpenFresco middleware-based operation of the software is explained and underlying processes of the TCP/IP communication block developed in LabVIEW were discussed. Command generation, target compensation and error tracking algorithms developed in this work were presented together with the sequence operation in the simulation coordinator. The superior performance of Lagrange-based extrapolation-interpolation were briefly analyzed. On the other hand, the implementation and merits of the middleware-free approach, that uses a simple numerical solver inside LabVIEW application, were also mentioned.

In the validation phase, conditions for testing and preparation of a test setup were presented. Moment resisting steel frames were selected for validation process due to ease in preparing test setups and cost of building several mockups during an extensive validation program. The results of a closed-loop hybrid

test on the one-storey two-bay steel frame were presented and the errors prevailed in control/compensation were pointed out for future improvement. Subsequently, the potential of hybrid dynamic simulation (HDS) for soil-structure interaction problems together with the testing framework developed at LNEC were presented. The challenges for a successful HDS in the context of a soil-structure system were also discussed.

Finally, the hybrid fire simulations and test platform developed at ETH Zurich was presented, representing a state-of-the-art facility for innovative testing.

4.1.2 Future developments

Regarding the HDS of soil-structure systems, the test setup proposed @LNEC, which considers a shake table and an additional actuator could also be simplified by simply using a shake table and a fixed rod instead of an additional actuator. In this approach, the interface force, which should be applied by the auxiliary actuator, is transformed to an equivalent acceleration command of the shake table. This infers that the shake table needs to be controlled in real time, adopting good acceleration tracking control capabilities because its command is not known a priori. The exploration of this technique is part of a future study.

On the other hand, the software framework was developed to promote ease during its future development. The current implementation of the OpenFresco based scheme works only with a two-point control, i.e. one control parameter from the numerical substructure. However, future applications may require hybrid tests with more than one control parameter. Extension of the two-point control to a higher number is therefore one of the future tasks for this application. Besides, the speed of hybrid tests that are conducted using OpenFresco are limited. To improve this limitation, the middleware-free scheme was proposed and implemented in this work. Nevertheless, it has certain drawbacks: the LabVIEW software does not offer computational resources that are geared towards finite-element programming and, hence, the numerical solver developed in the latter is limited for linear numerical substructures. To this end, another approach for implementing the solution of a numerical substructure without imposing strict speed limitations is desirable. A candidate method, in this context, could be using MATLAB programming environment, for solving the numerical substructure, while interacting with LabVIEW based control through dynamic link libraries (dlls). For example, the Model Interface Toolkit (MIT) provides a method for creating a LabVIEW-based user interface for a Simulink model. It converts the Simulink model into a dynamic link library allowing the model to run in a real-time target. The Simulink model could be designed to execute MATLAB functions that are responsible for solving a nonlinear numerical substructure.

Finally, the concept of HFS was briefly introduced but, in order to enable HDS with existing FE software, an OpenFresco control class needs to be tailored to the 3-DOF TM test rig. As such, a 3-DOF *ThermalShell* will replace the 1-DOF *ThermalTruss* experimental element class. Similarly, a *ThreeActuator* experimental setup class will be coded to handle the three axes of the 3-DOF TM test rig. On the other side, *ThermalMulti* experimental setup class will control the two arrays of Peltier modules and the infrared lamp. Finally, the SAFIR finite-element code for analysis of structures subjected to fire, may be used instead of OpenSees.

5 References

- Bcomp (2019) "powerRibs." Available at: [http://www.bcomp.ch/en/products/composite plate](http://www.bcomp.ch/en/products/composite%20plate)
- Behrouz Forouzan A (2010) "*TCP/IP Protocol Suite.*" 4th Ed. McGraw-Hill.
- Benavent-Climent A (2007) "An energy-based damage model for seismic response of steel structures." *Earthquake Eng Struct Dyn*, 36 (8): 1049-1064. DOI: 10.1002/eqe.671.
- Benavent-Climent, A (2010) "A brace-type seismic damper based on yielding the walls of hollow structural sections." *Engineering Structures*, 32: 1113-1122.
- Boore, David M. (2002) "Effect of Baseline Corrections on Displacements and Response Spectra for Several Recordings of the 1999 Chi-Chi, Taiwan, Earthquake." *Bulletin of the Seismological Society of America*, 91 (5): 1199–1211.
- Boore, David M., Christopher D. Stephens, and William B. Joyner (2002) "Comments on Baseline Correction of Digital Strong-Motion Data: Examples from the 1999 Hector Mine, California, Earthquake." *Bulletin of the Seismological Society of America*, 92 (4): 1543–1560.
- Carrion, Juan E, and Billie F Spencer (2007) "Model-Based Strategies for Real-Time Hybrid Testing, NSEL Report Series." *Report No. NSEL-006*. Illinois, USA.
- Chae, Yunbyeong, Kazemibidokhti and Karim, and James M. Ricles (2013) "Adaptive Time Series Compensator for Delay Compensation of Servo-Hydraulic Actuator Systems for Real-Time Hybrid Simulation." *Earthquake Engineering and Structural Dynamics*, 42: 1697–1715.
- Chen, Cheng, and James M. Ricles (2010) "Tracking Error-Based Servohydraulic Actuator Adaptive Compensation for Real-Time Hybrid Simulation." *Journal of Structural Engineering*, 136(4): 432–440.
- Christenson, Richard et al. (2014) "*Hybrid Simulation: A Discussion of Current Assessment Measures.*" <https://nees.org/resources/13416>.
- Combescure, Didier, and Pierre Pegon (1997) "Alpha-Operator Splitting Time Integration Technique for Pseudodynamic Testing Error Propagation Analysis." *Soil Dynamics and Earthquake Engineering*, 16: 427–443.
- Dabaghi, M. and A. Der Kiureghian (2018) "Simulation of orthogonal horizontal components of near-fault ground motion for specified earthquake source and site characteristics." *Earthquake Engineering and Structural Dynamics*, vol. 47, no. 6, pp. 1369-1393.
- Darby, A. P., M. S. Williams, and A. Blakeborough (2002) "Stability and Delay Compensation for Real-Time Substructure Testing." *Journal of Engineering Mechanics*, 128 (12): 1276–84.
- Das, A., Deb, S.K. and Dutta, A. (2016) "Comparison of numerical and experimental seismic Responses of FREI-Supported Un-reinforced Brick Masonry Model Building." *Journal of Earthquake Engineering*, 20 (8): 1239-1262. DOI: 10.1080/13632469.2016.1140098
- Das, A., Dutta, A., and Deb, S.K. (2015) "Performance of fiber-reinforced elastomeric base isolators under cyclic excitation." *Journal of Structural Control and Health Monitoring*, Vol. 22, No. 2. DOI: 10.1002/stc.1668.
- DesRoches, R., J. McCormick, and M. Delemont (2004) "Cyclic Properties of Superelastic Shape Memory Alloy Wires and Bars." *Journal of Structural Engineering*, 130 (1): 38-46.
- Dolce, M. and D. Cardone (2001) "Mechanical Behaviour of Shape Memory Alloys for Seismic Applications – 1. Martensite and Austenite NiTi Bars Subjected to Torsion." *International Journal of Mechanical Sciences*, 43 (11): 2631-2656. DOI: 10.1016/S0020-7403(01)00049-2.

- Dong, Baiping (2015) "Large-Scale Experimental, Numerical, and Design Studies of Steel MRF Structures with Nonlinear Viscous Dampers under Seismic Loading." *Phd Thesis*, Lehigh University.
- Fenves, Gregory L., Frank McKenna, Michael H. Scott, and Yoshikazu Takahashi (2004) "An Object-Oriented Software Environment for Collaborative Network Simulation." *13th World Conference on Earthquake Engineering*.
- Franssen, J.-M. and T. Gernay (2017) "Modeling structures in fire with SAFIR®: Theoretical background and capabilities." *Journal of Structural Fire Engineering*, vol. 8, no. 3, pp. 300-323.
- Hanley, Jason et al. (2003) "Continuous Hybrid Simulation with Geographically Distributed Substructures." *1st International Conference in Advances in Experimental Structural Engineering*.
- Hessabi, R Mirza, and Oya Mercan (2007). "Phase and Amplitude Error Indices for Error Quantification in Pseudodynamic Testing." *Pacific Conference on Earthquake Engineering*.
- Iniewski, Krzysztof, Carl McCrosky, and Daniel Minoli (2008) "TCP/IP Protocol Suite." In *Network Infrastructure and Architecture*, John Wiley & Sons, 137–181.
- Kelly, J. M. and Takhirov, S. M. (2001) "Analytical and experimental study of fiber-reinforced elastomeric isolator." *PEER Report 2001/11*, University of California, Berkeley.
- Kelly, J. M. and Takhirov, S. M. (2002) "Analytical and experimental study of fiber-reinforced strip isolators." *PEER Report 2002/11*, University of California, Berkeley.
- Kim, Hong Ki (2011) "Development and Implementation of Advanced Control Methods for Hybrid Simulation." *PhD Thesis*, University of California, Berkeley.
- Kolay, Chinmoy (2016). "Parametrically Dissipative Explicit Direct Integration Algorithms for Computational and Experimental Structural Dynamics." *PhD Thesis*, Lehigh University.
- Korzen, M., G. Magonette and P. Buchet (1999) "Mechanical Loading of Columns in Fire Tests by Means of the Substructuring Method." *Zeitschrift für Angewandte Mathematik und Mechanik*, vol. 79, pp. 617-618.
- Kwon, Oh-Sung et al. (2007) "User Manual and Examples for UI-SIMCOR v2.6 (Multi-Site Substructure Pseudo-Dynamic Simulation Coordinator) and NEES-SAM v2.0 (Static Analysis Module for NEESgrid)."
- Kwon, Oh-Sung, N. Nakata, A. Elnashai, and B. Spencer (2005) "A Framework for Multi-Site Distributed Simulation." *Journal of Earthquake Engineering*, 9 (5): 741–753.
- Lewin, M. (2007) "*Handbook of Fiber Chemist*." CRC Press.
- Maghareh, A., S. J. Dyke, A. Prakash, and J. F. Rhoads (2013) "Establishing Predictive Indicators for Stability and Performance of SDOF Real-Time Hybrid Simulations." *Report*, University of Purdue, West Lafayette, Indiana.
- McCormick, Jason, Jeff Tyber, Reginald DesRoches, Ken Gall, and Hans J. Maier (2007) "Structural Engineering with NiTi. II: Mechanical Behavior and Scaling." *Journal of Engineering Mechanics*, 133 (9): 1019-1029
- McKenna, F., G. Fenves and M. H. Scott (2000) "*Open System for Earthquake Engineering Simulation*." Pacific Earthquake Engineering Research Center.
- Mercan, Oya, and James M. Ricles (2009) "Experimental Studies on Real-Time Testing of Structures with Elastomeric Dampers." *Journal of Structural Engineering*, 135 (9): 1124–1133.
- Mergny, E., D. Elke, G. Drion and J. Franssen (2018) "A Pi-Controller for Hybrid Fire Testing in a Non-Linear Environment." *10th International Conference of Structures in Fire*, Belfast, UK.
- Mostafaei, H. (2013a) "Hybrid fire testing for assessing performance of structures in fire—Methodology." *Fire Safety Journal*, vol. 58, pp. 170-179, 2013.

- Mostafaei, H. (2013b) "Hybrid fire testing for assessing performance of structures in fire—Application." *Fire safety journal*, vol. 56, pp. 30-38.
- Moumni, Z., A. Van Herpen, and P. Riberty (2005) "Fatigue Analysis of Shape Memory Alloys: Energy Approach." *Smart Materials & Structures*, 14 (5): S292. DOI: 10.1088/0964-1726/14/5/017.
- Nakashima, Masayoshi, Hiroto Kato, and Eiji Takaoka (1992) "Development of Real-Time Pseudo Dynamic Testing." *Earthquake Engineering and Structural Dynamics*, 21 (1): 79–92.
- Nakashima, Masayoshi, and Nobuaki Masaoka (1999) "Real-Time on-Line Test for MDOF Systems." *Earthquake Engineering and Structural Dynamics*, 28 (4): 393–420.
- Nezhad, H. T., Tait, J. M., and Drysdale, R. G. (2008) "Lateral response evaluation of fiber-reinforced neoprene seismic isolator utilized in an Un-bonded Application." *Journal of Structural Engineering*, 134: 850–859.
- Nezhad, H. T., Tait, M. J., and Drysdale, R. G. (2009a) "Simplified analysis of a low-rise building seismically isolated with stable un-bonded fibre reinforced elastomeric isolators." *Canadian Journal of Civil Engineering*, 36 (7): 1182–1194.
- Nezhad, H. T., Tait, M. J., and Drysdale, R. G. (2009b) "Shake table study on an ordinary low-rise building seismically isolated with SU-FREIs (stable unbonded-fiber reinforced elastomeric isolators)." *Journal of Earthquake Engineering and Structural Dynamics*, 38: 1335–1357.
- Paulson, T. J., Abrams, D. P., and Mayes, R. L. (1991) "Shaking-table study of base isolation for masonry buildings." *Journal of Structural Engineering*, 117 (11): 3315–3336.
- Powell, T., S. Panigrahi, J. Ward and L. Tabil (2002) "Engineering Properties of Flax Fiber and Flax Fiber-Reinforced thermoplastic in Rotational molding." *ASAE/CSAE North-Central Intersectional Meeting*, Saskatoon.
- Qureshi, R. and N. Elhami-Khorasani (2018) "Instantaneous Stiffness Correction for Hybrid Fire Testing." *10th International Conference of Structures in Fire*, Belfast, UK.
- Robert, F., S. Rimlinger and C. Collignon (2009) "Promethee, Fire Resistance Facility Taking Into Account the Surrounding Structure." *1st international Workshop on Concrete Spalling due to Fire Exposure*, Leipzig, Germany.
- Saouma, Victor, and Mettupulyam Sivaselvan (2008) "*Hybrid Simulation: Theory, Implementation and Applications*." Taylor & Francis.
- Sauca, A., T. Gernay, F. Robert and N. Tondini (2018) "Hybrid fire testing: Discussion on stability and implementation of a new method in a virtual environment." *Journal of Structural Fire Engineering*, vol. 9, no. 4, pp. 319-341.
- Schellenberg, Andreas, and Stephen Mahin (2006) "Integration of Hybrid Simulation in the General-Purpose Computational Framework OpenSees." *8th National Conference on Earthquake Engineering*, San Francisco, California, USA.
- Schellenberg, Andreas, S. Mahin and G. Fenves (2007) "A software framework for hybrid simulation of large structural systems." *Structural Engineering Research Frontiers*, pp. 1-16.
- Schellenberg, Andreas H et al. (2009) "OpenFresco Command Language Manual: OpenFresco v2.6." *Technical Report*. California, USA. <http://openfresco.berkeley.edu/documentation/misc/>.
- Schellenberg, Andreas H, Stephen A Mahin, and Gregory L Fenves (2009) "Advanced Implementation of Hybrid Simulation." *Report*, University of California, Berkeley.
- Schulthess, P. and M. Neuenschwander (2016) "Consolidated Fire Analysis—Coupled Thermo-mechanical Modelling for Global Structural Fire Analysis." *9th International Conference of Structures in Fire*, Princeton, NJ, USA, 2016.

- Spurnins, E. (2009) "Mechanical Properties of Flax Fibers and Their Composites." *PhD thesis*, Lulea University of Technology.
- Spencer, B.F. et al. (2006) "Multi-Site Soil-Structure-Foundation Interaction Test (MISST)." *University of Illinois*, http://nees.org/data/get/NEES-2006-0120/Documentation/MISST_Report_Final_Web.doc.
- Stefanaki, Aikaterini, Mettupalaya V. Sivaselvan, Anthony Tessari, and Andrew Whittaker (2015) "Soil-Foundation-Structure Interaction Using Hybrid Simulation." *23rd Conference on Structural Mechanics in Reactor Technology (SMIRT23)*, Manchester, UK, Division V; Paper ID 730.
- Takahashi, Yoshikazu, and Gregory L. Fenves (2006) "Software Framework for Distributed Experimental-Computational Simulation of Structural Systems." *Earthquake Engineering and Structural Dynamics*, 35 (3): 267–91. <http://doi.wiley.com/10.1002/eqe.518>.
- Tekeste, Gidewon G, António A Correia, and Aníbal G Costa (2017) "Stability Analysis of a Real-Time Shake Table Hybrid Simulation for Linear and Non-Linear SDOF Systems." *7th International Conference on Advances in Experimental Structural Engineering*.
- Thewalt, Christopher R., and Stephen A. Mahin (1987) "Hybrid Solution Techniques for Generalized Pseudodynamic Testing." *Earthquake Engineering Research Center*, University of California.
- Van Engelen, N. C., Tait, J. M., and Konstantinidis, D. (2012) "Investigation of base isolated structures utilizing stable unbonded fiber reinforced elastomeric isolator." *15th World Conference on Earthquake Engineering*, Lisbon, Portugal.
- Vemuru, V. S. M., Nagarajaiah, S., Masroor, A., and Mosqueda, G. (2014) "Dynamic lateral stability of elastomeric seismic isolation bearings." *Journal of Structural Engineering*, 140 (8). DOI: 10.1061/(ASCE)ST.1943-541X.0000955.
- Wang, X., R. E. Kim and O. Kwon (2018) "Hybrid Simulation Method for a Structure Subjected to Fire and Its Application to a Steel Frame." *Journal of Structural Engineering*, vol. 144, no. 8.
- Whyte, C., K. Mackie and B. Stojadinovic (2015) "Hybrid simulation of thermomechanical structural response." *Journal of Structural Engineering*, DOI: 10.1061/(ASCE)ST.1943-541X.0001346.
- Yun, Xiang, and Leroy Gardner (2017) "Stress-Strain Curves for Hot-Rolled Steels." *Journal of Constructional Steel Research*, 133 (September): 36–46.
- Zhu, Songye and Yunfeng Zhang (2013) "Loading Rate Effect on Superelastic SMA-Based Seismic Response Modification Devices." *Earthquakes and Structures*, 4 (6): 607-627. DOI: 10.12989/eas.2013.4.6.607.

Liability claim

The European Commission is not responsible for any use that may be made of the information contained in this document. Also, responsibility for the information and views expressed in this document lies entirely with the author(s).